

May 2019

A Real-Time Approach to Process Monitoring of Heavy Metals: Spectrophotometric Characterization and Application of Novel Azo

Joseph Timothy Labeots
University of Wisconsin-Milwaukee

Follow this and additional works at: <https://dc.uwm.edu/etd>

 Part of the [Chemistry Commons](#)

Recommended Citation

Labeots, Joseph Timothy, "A Real-Time Approach to Process Monitoring of Heavy Metals: Spectrophotometric Characterization and Application of Novel Azo" (2019). *Theses and Dissertations*. 2089.
<https://dc.uwm.edu/etd/2089>

This Dissertation is brought to you for free and open access by UWM Digital Commons. It has been accepted for inclusion in Theses and Dissertations by an authorized administrator of UWM Digital Commons. For more information, please contact open-access@uwm.edu.

A REAL-TIME APPROACH TO PROCESS MONITORING OF
HEAVY METALS:
SPECTROPHOTOMETRIC CHARACTERIZATION AND
APPLICATION OF NOVEL AZO DYES

by

Joseph T. Labeots

A Dissertation Submitted in
Partial Fulfillment of the
Requirements for the Degree of

Doctor of Philosophy
in Chemistry

at

The University of Wisconsin-Milwaukee

May 2019

ABSTRACT

A REAL-TIME APPROACH TO PROCESS MONITORING OF HEAVY METALS: SPECTROPHOTOMETRIC CHARACTERIZATION AND APPLICATION OF NOVEL AZO

by

Joseph T. Labeots

The University of Wisconsin-Milwaukee, 2019

Under the Supervision of Professor Joseph H. Aldstadt, III and Professor Alan Schwabacher

I will describe studies in developing an on-line system for process monitoring that is based upon spectrophotometric methods. Heavy metals that are discarded into the environment may pose severe threats to public health, and are thus heavily regulated. Currently, there is no reasonably affordable, reliable, real-time monitoring method for heavy metals in water. This lack of feedback for industrial applications often leads to wasted resources due to massive overtreatment to avoid costly penalties. Spectrophotometry is a viable analysis option assuming a suitable sensor molecule is available as seemingly conflicting requirements may occur. Characterization of the sensor is one of the most important considerations when developing an analytical method. For this application, the sensor must be well understood in order to accurately quantify the analyte(s). This involves studying pKa values and binding affinities to fully understand the responses that are seen. Classic titrimetric methods can be used along with multivariate analysis to determine these values. The metal response of a library of novel azo dyes was studied and full characterization is shown on one potential candidate. This characterization includes defining the working regions of the dye and binding affinities to the metals it complexes.

Additionally, a partial Least Squares approach can be used to build a predictive model. This can then simultaneously predict the concentrations of multiple metals in an aqueous sample

with exquisite accuracy. This was shown with commercially available, 4-(2-Pyridylazo)resorcinol and 4 metals (Cu,Ni,An,Pb). The mean prediction error for replicate measurements was 0.19 μM (12 ppb) for copper, 0.36 μM (21 ppb) for nickel, 0.26 μM (17 ppb) for zinc, and is 0.14 μM (29 ppb) for lead, and the corresponding standard deviations were below 10 ppb.

The predictive model that was used in solution studies needed to be adapted for flow experiments for use in a remote sensor application. To do this, the sensor dyes were attached to a solid support for use in a flow cell. Flow studies were completed with 2 types of flow systems. The first, was an industrial style that had large volumes and flow rates run by multiple pumps. This flow system was shown to have a stable response to low ppb metal concentrations over several hours. The other flow system used was a sequential injection analysis (SIA) platform. This setup was particularly useful when identifying factors that needed to be included when attempting to model binding and quantify metals. Initial results suggest low ppm detection limits for the monitor being developed with Sequential Injection Analysis (SIA) techniques being explored for a possible microscale device.

**© Copyright by Joseph T. Labeots, 2019
All Rights Reserved**

To
my wife,
my daughter,
and my parents
Thank you

TABLE OF CONTENTS

| | |
|--|------|
| LIST OF FIGURES | viii |
| LIST OF TABLES | xiv |
| ACKNOWLEDGEMENTS | xv |
| Chapter 1: Introduction | 1 |
| 1.1 Background | 1 |
| 1.2 Spectrometric Techniques | 3 |
| 1.3 Process Monitoring | 5 |
| 1.4 Azo Dyes in Quantitative Analysis | 6 |
| 1.5 Sensor Dye Films and Arrays | 7 |
| 1.6 Multivariate Analysis Overview | 8 |
| 1.7 Modeling Equilibrium Constants with Multi-Variate Analysis | 9 |
| 1.8 Quantitative Analysis Using Multi-Variate Analysis | 10 |
| 1.9 Partial Least Squares | 12 |
| 1.10 Continuous Flow: Flow Injection Analysis (FIA) | 14 |
| 1.11 Sequential Injection Analysis (SIA) | 15 |
| Chapter 2: Experimental | 22 |
| 2.1 Materials | 22 |
| 2.1.1 Reagents | 22 |
| 2.1.2 Buffer Preparation | 23 |
| 2.1.3 Labware | 23 |
| 2.2 Instrumentation | 24 |
| 2.3 Flow Studies Using the Conventional System | 24 |
| 2.3.1 Flow Cell Design | 24 |
| 2.3.2 Flow System Configuration | 25 |
| 2.3.3 Quantitation Method | 25 |
| 2.4 Flow Studies Using Sequential Injection Analysis | 26 |
| 2.4.1 Flow cell design | 26 |
| 2.4.2 Flow System Configuration | 26 |
| 2.4.3 Quantitation method | 27 |
| 2.5 Treatment of Error | 28 |
| Chapter 3: Results and Discussion | 34 |

| | |
|---|-----|
| 3.1 Preface..... | 34 |
| 3.2 Free Dye Characterization | 34 |
| 3.2.1 Solvatochromism Study | 36 |
| 3.2.2 MOPS Aggregation Study | 37 |
| 3.2.3 Free Dye pK _a Studies | 38 |
| 3.2.4 Determination of Metal Complex pK _a Values | 42 |
| 3.2.5 Determination of Binding Ratios | 44 |
| 3.2.6 Study of Binding Affinities..... | 46 |
| 3.2.7 Development of a PLS Model..... | 49 |
| 3.2.8 Dye Longevity Study | 54 |
| 3.3 Flow Experiments | 54 |
| 3.3.1 Conventional Flow Experiments..... | 55 |
| 3.3.2 SIA Experiments | 60 |
| Chapter 4: Conclusion..... | 127 |
| Appendix I. Error Propagation for ReactLab Experiments | 133 |
| Appendix 2: Dye Structures | 137 |
| Appendix 3: Metal Responses | 142 |
| References | 151 |
| CURRICULUM VITAE..... | 157 |

LIST OF FIGURES

| | |
|--|----|
| Figure 1: Synthesis of ZP family fluorophores. Changing the “X” and “Y” groups yields a fluorophore with unique excitation/emission wavelength, pK_a , and K_d values. ³⁸ | 17 |
| Figure 2. Chemical structures of commercial azo-based sensors (PAR and PAN) as well as the focus in this work (PAN-7OH). The conjugation and moieties lead to a change in spectral characteristics and responses of the dye. | 17 |
| Figure 3: Illustration of multivariate analysis approach for the determination of equilibrium constants from absorption spectra adapted from Reference 65 ⁶⁵ . Graphical illustration (left) shows the variable space where the complex formation [ML] leads to a decrease in signal for the free dye [L] and in an increase in signal for ML. The spectral data is iteratively fit to a model to minimize residuals and calculate equilibrium concentrations which are used to find the formation constants from nonlinear regression..... | 18 |
| Figure 4. Illustration of projection of data onto subspace for determining latent variables and PLS regression for building a predictive model. Matrix dimensions are denoted with a lowercase letter. A portion of the figure was adapted from references 78, 101, and 102 ^{101,102,78} | 19 |
| Figure 5: Schematic diagram of FIA (top) and SIA (bottom) instrument designs. In FIA, the flow is unidirectional, and a sample “plug” is injected into the carrier via a valve. The pumps used in FIA are typically peristaltic and the solution is taken through a mixing coil to improve homogeneity. In this example, there is an additional reagent line that mixes with the sample before the mixing coil. In SIA, the pump is bidirectional (syringe) and a multiposition valve (MPV) is used to stack reagent “zones” in the holding coil before dispensing them to the detector. These zones disperse and mix to a certain extent as they travel to the detector. | 20 |
| Figure 6: Dispersion profile created in FIA/SIA that forms a concentration gradient. When a sample zone (red) is in contact with the reagent zone (blue), a product zone (yellow) forms between them. This sandwiched zone is then sent to the detector. The size of this zone can be controlled by flow rates, volumes, tubing dimensions, etc. ¹⁰³ | 21 |
| Figure 7: Schematic of the Perkin-Elmer spectrometer used in some UV-Vis experiments. | 30 |
| Figure 8: Schematic of the optical components (crossed Czerny-Turner) of the StellarNet Black Comet used in UV-Vis experiments. ¹⁰⁴ | 31 |
| Figure 9: Conventional flow system (version 1) with combined buffer and sample flow lines..... | 31 |
| Figure 10 Conventional Flow System (version 2) with separate buffer and sample flow lines.... | 32 |
| Figure 11: Schematic diagram of the conventional flow cell. | 32 |

Figure 12: Schematic diagram of the SIA system.¹⁰³ The selection valve has multiple positions and is used to cycle between reagents, samples, standards, etc. The device is controlled via a computer interface that allows the user to easily manipulate zones of fluid to a detector.33

Figure 13: Picture of SIA flow cell showing optical path as well as the Z-type flow path33

Figure 14: Visual response of four dyes to 16 metals (pH 7.0). Even for similar responses, there is enough spectral information so that multiple metals can be distinguished.71

Figure 15: QAN 1,5-OH (325 μ M) in less polar solvents toluene and chloroform. The λ_{max} is blue shifted relative to several more polar solvents. This would lead to the classification of positive solvatochromism for this dye.....72

Figure 16: Solvatochromism of QAN-1,5OH in more polar solvents (acetonitrile and DMF). The spectra are red shifted in these solvents with higher polarity which indicates that QAN 1,5-OH can be classified as a positive solvatochromic dye.....73

Figure 17: Metal complex aggregation is seen with certain buffers. The scattering was eliminated for PAN-7OH with Cr(III) and Fe(II) by using different buffers. There was no response for Cr(III) in EPPS buffer at pH 7.5 (top) while there were spectral changes seen for Fe(II) in acetate buffer at pH 4.7 (bottom).....74

Figure 18: PAN-7OH pK_a results. The results for the pK_a testing on PAN-7OH are shown with the species distribution and decomposed spectra from Reactlab analysis. The decomposed spectra show 4 distinct species that exist over the pH region tested. The species distribution identifies pK_a values where species exist in a 50:50 ratio.....75

Figure 19: QAN-1,5OH pK_a values. The results for the pK_a testing on QAN-1,5OH are shown with the species distribution and decomposed spectra from Reactlab analysis. The first and third pK_a values are lower than PAN-7OH and the middle pK_a is slightly higher. The decomposed spectra show that the completely deprotonated has a molar absorptivity coefficient that is nearly five times higher than that of the other species.76

Figure 20: QAN-4OH pK_a results. The results for the pK_a testing on QAN-4OH are shown with the species distribution and decomposed spectra from Reactlab analysis. The L²⁻ and LH¹⁻ decomposed spectra are very similar and this may be a result of the model overfitting. This results in the first two pK_a values being very close together.77

Figure 21: Initial binding ratio studies for PAN-7OH. All metals bind in a 1:2 (M:L) ratio except for Pb which shows 1:1 binding. By tracking the disappearance of the free dye spectral peak (red) or appearance of the metal-dye complex peak (black) the binding ratio can be determined. Some binding curves, such as Ni, are not clear results. Nevertheless, the 1:2 binding model was used for all metals except Pb because previous studies and model fitting.....80

Figure 22: Modeled species for metal complex pH studies. The decomplexation occurs in all cases at low pH. It appears that it also occurs at high pH but was only modeled effectively in the

case of Pb. There is only one dye shown in these structures for simplicity, but they do bind in a 1:2 fashion for all metals but Pb.81

Figure 23: Decomplexation at low and high pH. The metal complex spectra for the Zn experiment looks like the free dye at low pH (top left). The spectra for the complex shown at high pH begin to shift towards the free dye peak but this is not enough to accurately model (top right). The decomplexation of the Pb complex is complete enough to model at the pH values tested (bottom left).82

Figure 24: Pourbaix diagram for Pb showing the formation of Pb/O compounds at higher pH values. The formation of metal oxides and metal hydroxides is likely the cause of decomplexation at high pH. There is a competition between forming a complex with the dye and complexing oxygen.83

Figure 25: Species distribution of PAN-7OH metal complexes (previous pages). The species distribution of the metal complexes of PAN-7OH are made with computed concentrations of each species from the Reactlab analysis. All complexes were modeled as 1:2 binding except for Pb. The first pK_a values is decomplexation at low pH, the second is deprotonation of the complex, and the third (Pb) is the decomplexation at high pH because metal hydroxide and oxide formation.86

Figure 26: Binding affinity curve of PAN-7OH and Zn (left) and decomposed spectra (right) for PAN-7OH metal complex. The curve shows good hyperbolicity with the $[dye]_0 \approx K_D$. The decomposed spectra show good agreement with the raw data which is one indicator that the model is fitting correct species.87

Figure 27: Binding affinity curve of PAN-7OH and Ni (left) and decomposed spectra (right) for PAN-7OH metal complex. The curve shows good hyperbolicity with the $[dye]_0 \approx K_D$. The decomposed spectra show good agreement with the raw data which is one indicator that the model is fitting correct species.88

Figure 28: Binding affinity curve of PAN-7OH and Cu (left) and decomposed spectra (right) for PAN-7OH metal complex. The curve shows good hyperbolicity with the $[dye]_0 \approx K_D$. The decomposed spectra show good agreement with the raw data which is one indicator that the model is fitting correct species.89

Figure 29: Binding affinity curve of PAN-7OH and Cd (left) and decomposed spectra (right) for PAN-7OH metal complex. The curve shows good hyperbolicity with the $[dye]_0 \approx K_D$. The decomposed spectra show good agreement with the raw data which is one indicator that the model is fitting correct species.90

Figure 30: Binding affinity curve of PAN-7OH and Co (left) and decomposed spectra (right) for PAN-7OH metal complex. The curve shows good hyperbolicity with the $[dye]_0 \approx K_D$. The decomposed spectra show good agreement with the raw data which is one indicator that the model is fitting correct species.91

Figure 31: Binding affinity curve of PAN-7OH and Zn (left) and decomposed spectra(right)for PAN-7OH metal complex. The curve shows good hyperbolicity with the $[dye]_0 \approx K_D$. The decomposed spectra show good agreement with the raw data which is one indicator that the model is fitting correct species. Pb was modeled as a 1:1 binding.92

Figure 32: The binding affinity of PAN-7OH increases relative to ionic radius. The smaller ions such as Cu(II), Co(II), Zn(II), and Ni(II) have much smaller K_D values than that of Cd(II) and Pb(II).....93

Figure 33: Example Variable Importance Plot (VIP) for PLS analysis. The VIP can give insight into important spectral features that improve the model. The peaks of the plot correspond to free and bound dye peaks. The best interpretation of these peaks is shown in the inset tables.94

Figure 34: Plots of absolute prediction error of pseudo-unknown samples. The errors are relatively low and do not seem to follow a trend among the four metals.95

Figure 35: Distribution of absolute prediction errors. The predictor error is generally gaussian in shape and were low in all samples.....96

Figure 36: The comparison between types of PLS models show that binary had the highest error in all cases. The complete model (black) and the trimmed (red) model from the VIP data show similar errors in all cases.....97

Figure 37: Longevity studies done of several chemosensors. The molar absorptivity coefficient was normalized to the first week of measurements.99

Figure 38: Response of the PAR film to three different Zn concentrations (10 to 30 mg L⁻¹). The negative absorbance appears because the buffer concentration (0.01 M) was too low and the acidic AA standard neutralized the dye. 100

Figure 39: Typical response of films to 5 mg L⁻¹Zn when proper MOPS concentration was used. The spectral response (top) shows a negative peak for the free dye and a positive peak for the metal complex. The growth of these peaks can be monitored over time (bottom). 101

Figure 40: Repeatability of an OAN film to 1 mg L⁻¹ Zn. The response (top) is negative when rinsed with acid and then positive when metal is binding. The average RSD for all data points was 1.54% (bottom). 102

Figure 41: Several trials of the PAR film response to 10.9 mg L⁻¹ Zn are shown as concatenated data. The return to baseline with acid wash is quick (1-2 min)..... 103

Figure 42: PAR film response to 1 mg L⁻¹ Ni. One run (solid line) was done for a longer period to see if saturation could be reached..... 104

Figure 43: Response of PAR film to 100 mg L⁻¹ Zn. Longer runs were done to see if saturation could be reached. 105

Figure 44: Response of PAR film (519 nm) to 1 mg L⁻¹ Zn at varying flow rates. The first two trials were at 4.72 mL min⁻¹ and the final five at 10.6 mL min⁻¹. The last trial was stopped to examine stopped flow conditions..... 106

Figure 45: Stopped flow response (516 nm) of a PAR film to 100 µg L⁻¹ Zn. The solid line is continuous flow and the dashed line has flow stopped at the point marked. 107

Figure 46: Attempting to reach saturation for a cationic PAR film (516 nm) with 100 µg L⁻¹ Zn. Saturation was not reached, even after 250 minutes..... 108

Figure 47: Response of a PAR film to 1 mg L⁻¹ Cu. The response (512 nm) was monitored over time..... 109

Figure 48: Photograph of the SIA flow cell design. The flow cell is a Z-design but has a cutout that allows a slide with the chemosensor to be inserted (courtesy of G. Marshall). 110

Figure 49: Initial response (500 nm) to the acid wash cycle (0.1 M HCl) when using large volumes of acid and buffer to wash and equilibrate the film, the Absorbance is initially negative when being washed by acid and then returns to zero when equilibrated with buffer. 111

Figure 50: The adjusted response (500 nm) when using appropriate volumes of acid (0.1 M HCl) and buffer (0.1M MOPS) to wash and equilibrate the film. 111

Figure 51: Typical response for a QAR film to 100 mg L⁻¹ Zn. The negative peak occurs when the buffer is neutralized by acid..... 112

Figure 52: Repeatability of PAR film for two trials of 3.3 mg L⁻¹ Zn with an RSD of 2.07%. 113

Figure 53: Response of PAR to increasing Zn concentrations. Saturation is reached in all cases. 114

Figure 54: Response (525 nm) of a PAR film to increasing Zn concentrations. At 100 µM, saturation is reached within ~150 s. 115

Figure 55: Comparison of the initial rate of accumulation of Zn on a PAR film. The slope from 60-100 seconds (while the metal was accumulating) was used as a measure of the rate. 116

Figure 56: Response (525 nm) of a PAR film to increasing Zn concentrations at pH 7.0. The 95% confidence interval was used for error bars. The response of this film is linear at lower [Zn] (<3 mg L⁻¹) with a R² of 0.97 for a linear fit. At higher concentrations (>3 mg L⁻¹) the R² increases to 0.94..... 120

Figure 57: Response (525 nm) of PAR film to a baseline obtained using acid (0.1 M HCl) then buffered (pH 7.0). The baseline was taken in acidic and buffered (pH 7.0) conditions..... 122

Figure 58: Effect of pH on binding rate. The best binding occurs near neutral pH because there is little competition..... 123

Figure 59: Effect of ionic strength on binding rate (2.29 mg L⁻¹ Zn). The ionic strength of the metal sample was varied by adding NaCl (n=4). 124

Figure 60: Effect of metal concentration of binding rate. The response rate (525 nm) increases with increasing [Zn]. The initial slope was calculated to find the response rates. The linear behavior is shown in the full and cropped concentration range with an R² of 0.997 and 0.998 respectively..... 126

Figure 61: Spectral response of 8 novel azo dyes to 16 different heavy metals. Spectral responses can be useful in creating a spectral selectivity in an array of metal sensors. The unique or even similar response can give the information needed to distinguish multiple metals in solution..... 149

Figure 62: Characteristic responses of the 4 dyes from Figure 2 to a variety of metal ions (pH 7.0). The visual response can give some insight into what metals might complex with the dye, but the spectral response can give exact characteristics and be useful in determining the capability of the dye to be a sensor. 150

LIST OF TABLES

| | |
|--|----|
| Table I. Buffers were prepared from acid and base (conjugate salt) in the region near the desired pH for a given experiment..... | 29 |
| Table II: Quick reference for metal response of azo dye library. In some cases, scattering was seen and is noted in the table with an "S". The responses for most dyes were a red shift in the absorbance spectrum. Green boxes indicate a significant shift in the spectrum when the metal is bound to the dye. Yellow boxes indicate where only a small shift (~10 nm) was seen, and red boxes are denoted with "NR" for "no response"..... | 66 |
| Table III: List of solvents tested while exploring the solvatochromism of QAN 1,5-OH. The dipole moment of the solvent was used as a measure of polarity. There appears to be a positive solvatochromic behavior but there are several unexplained exceptions that would be interesting to explore in the future work. ¹¹¹⁻¹¹⁴ | 67 |
| Table IV: Summary of pH studies for PAN-7OH and its metal complexes. The pK _a values for most metal complexes are similar to the free dye. The errors shown include regression and experimental errors. pK _{a3} was only modeled for Pb because it was too high to be modeled accurately for the others..... | 68 |
| Table V: Binding affinities for metals. The K _D values for PAN-7OH and the metals that it binds. The K _D ' value represents the square root of the K _D (for the 1:2 complexes) and are akin to a 1:1 binding affinity. The affinity for first row transition metals Cu, Ni, Zn, and Co are all very similar while the binding affinity is significantly less for bigger metals Pb and Cd. ¹¹⁵ The size of these metal ions likely causes weaker binding to occur. | 68 |
| Table VI: PLS prediction results for the simultaneous determination of 4 metals. The determination of Cu, Ni, Zn, and Pb using PAR and QAR at pH 7.0 and 20°C was achieved with very little error (<1µM total in all cases)..... | 69 |
| Table VII: PLS prediction results for solutions (n=19) of Cu, Ni, Zn, and Pb using PAR and QAR at pH 7.0 and 20°C. The mean error was less than 0.4 µM and the standard deviation was less than 0.15 for all metals..... | 70 |

ACKNOWLEDGEMENTS

Above all, I want to acknowledge my wife, Katie, for her perseverance and understanding throughout my studies. Her hard work as a wife and mother has not gone unnoticed during this journey. To my daughter, Corinne, thank you for inspiring me each and every day. I would like to acknowledge Mr. Paul Roth, my high school chemistry teacher. With the right mix of comedy, approachability, and incredible teaching skills, he has impacted more lives than he will ever know. He was the sole reason that I started my journey into the field of chemistry and for that, I thank him. Additionally, Dr. Paul Henning has been instrumental in my success. He was a great mentor due to his vast knowledge and advice. I would also like to thank my advisors, Dr. Peter Geissigner, Dr. Joseph Aldstadt, and Dr. Alan Schwabacher for their advice and guidance. Finally, I would like to thank my parents for their love and support. My late father was always someone who I looked up to and was always enthusiastic about my successes. He taught me to persevere and push through the tough times. The time I spent with him during my childhood are some of the best memories of my life. My mother is an incredibly hard worker who has inspired me to become the person I am today. I cannot thank her enough for her compassionate nature and ability to be understanding at all times

Chapter 1: Introduction

1.1 Background

Heavy metals have been of great concern for many decades when it comes to human health and their effects upon ecosystems. There are several heavy metals, such as Fe, Cu, Co, and Zn, that are nutritionally essential in small quantities.¹ However, heavy metals tend to form complexes with N-, O-, and S-containing compounds readily found in the body. For this reason, there has always been concern with exposure to heavy metal ions. Fe, for example, is needed for proper growth and development. It is a critical component of cytochromes that play a key role in brain development.² Thus, Fe is either provided through breastmilk, vitamins, or dietary supplements to newborns and children and is also necessary for adults but is commonly overlooked as an issue because it is often provided in a normal, balanced diet. Zn is another metal that is necessary for cellular processes and is an essential cofactor and plays a key role in neurotransmission^{3,4}, gene expression⁵, and enzyme regulation.⁶ Cu is a vital component of several metalloenzymes and deficiencies can result in defects that result in vascular, skeletal central nervous, and cardiovascular system problems.⁷⁻⁹ Co is a part of vitamin B-12 and helps the human body make red blood cells. It also contributes to the Krebs-cycle for producing energy from sugars as a part of the biotin dependent pathways.¹⁰ Most individuals get sufficient vitamin B-12 (therefore Co) from their diet as it is readily found in meats, milk, cheese, eggs, etc. Vegans can sometimes suffer from B-12 deficiency if they do not supplement in their diet. This usually leads to weakness, pale skin, and nerve problems.¹¹ These four metals highlighted play an important role but many heavy metals are quite toxic in even small amounts.

In general, the five most “dangerous” metals are As, Cd, Cr, Pb, and Hg because of their

carcinogenic properties even at low levels. Pb, for example, is extremely toxic even in small quantities, as evidenced recently by a major crisis with Pb in drinking water in Flint, MI. Pb often enters the drinking water through solder and the corrosion of brass components in plumbing, and acidic and hot water facilitate the release of Pb¹². Short-term and long-term exposure to Pb can cause abdominal pain, headaches, and weakness among other symptoms. The problem is that Pb poisoning can occur slowly and be masked by other common ailments. Additionally, it can cross the placental barrier causing Pb exposure to unborn children. Pb is extremely dangerous to developing age groups and can affect the behavior and intelligence of these young individuals.¹³ The severity of the health effects depends on numerous factors such as the metal and its abundance, speciation, route and length of exposure, etc.

Some heavy metals are naturally occurring but anthropogenic activities like mining, industrial discharge, and agricultural use play an important role in their spread within the environment.¹⁴ This includes waste or “spent” water emitted from industrial process plants such as those for Zn plating.¹⁵ Currently, there is no reasonably affordable, reliable, real-time monitoring method for heavy metals in water. This lack of feedback for industrial applications often leads to wasted resources because of massive overtreatment (e.g., precipitation as hydroxide) to avoid costly penalties from regulatory agencies. Rather than having the capability to monitor in real time, periodic “grab” samples are collected, with the analytical results obtained hours, if not days, later. Therefore, the availability of qualitative and quantitative information for heavy metals in wastewater, and the subsequent corrective actions to be taken if regulatory limits are exceeded, are lacking. The current practice is to heavily over-treat the wastewater with binding polymers and hydroxides to ensure that heavy metal concentrations are below regulatory levels prior to release to the environment. By development of a “sensing platform” capable of real-time, continuous

monitoring, a reduction in time, money, and other resources would be possible. Additionally, in the event of a process upset, there could be immediate intervention to reduce human and environmental exposure to these toxic metals.

1.2 Spectrometric Techniques

The most common techniques for accurate quantitation of heavy metals are inductively coupled plasma-mass spectrometry (ICP-MS)^{16,17} and atomic absorption spectroscopy (AAS)^{18,19}. These methods have great value in the laboratory because they are extremely precise, accurate, and robust. A typical example of AAS, was reported with an ionic liquid microextraction of Cu, Ni, and Zn followed by analysis with AAS. The LODs were determined to be 0.79, 0.93, 0.71 $\mu\text{g L}^{-1}$ respectively and RSD values ranged from 1.0-2.7%. The method was applied to both wastewater and alloy samples analyzed for these metals.²⁰ There is also a report of the simultaneous determination of Cu, Cr, Al, and Mn with AAS which had relative standard deviations of 1.7, 1.5, 1.6, and 1.5% and limits of detection (LODs) of 0.08, 0.05, 0.06, and 0.06 $\mu\text{g L}^{-1}$ respectively.²¹ In another example, a portable AAS was developed that allowed for analysis of Co in the field.²² Using 1-(2-pyridylazo)-2-naphthol (PAN) as a chelating agent for extraction, Co was detected with a LOD of 0.30 ppb under ideal conditions by researchers at Dali University. The extraction and analysis was also performed on real-world samples with less success.²² PAN was used in this case as the chelating agent rather than spectrophotometrically like the azo dyes presented in this work. Despite the impressive figures of merit in these examples, there are many issues that plague process analysis using sophisticated techniques such as ICP-MS and AAS, including capital costs, operating costs, instrument size or “footprint”, and the delay in obtaining analytical information.

Spectrophotometric methods have also commonly been used for heavy metal quantitation in process streams. Absorbance methods include the use of lipophilic “zincon” as a “one-shot” sensor for Cu^{2+} using an orange LED source,²³ the use of membranes with 4-(2-pyridylazo)resorcinol (PAR) derivative sites to measure Zn^{2+} ,²⁴ and many other examples summarized by Oehme and Wolfbeis.²⁵ Although some research using molecular absorbance spectroscopy has been done, by and large, fluorescence has been the preferred method as it is much more sensitive than absorbance-based measurements.^{26–31} The fluorophore 1,10-phenanthroline and its derivatives have great utility as fluorescence probes as they responds to both cations and anions. It has been shown to be a good probe for metals such as Pb^{2+} , Cu^{2+} , Na^+ , Hg^{2+} , Ni^{2+} , and Zn^{2+} with responses varying from wavelength shifts to quenching depending on the analyte.²⁶ It also shows responses to CN^- , H_2PO_4^- , F^- , and AcO^- . A metal analyte of interests for many decades has been Zn. Zn is ubiquitous in nature and second only to Fe in abundance as a heavy metal within the human body.²⁸ Small fluorescent Zn probes can be one of two classes: intensity-based or ratiometric (i.e., shift in excitation or emission wavelength). Early fluorometric sensors for Zn were quinoline-based until it was found that they formed ternary complexes with proteins that contain Zn.²⁸ Thus, labile Zn was not measured but rather the Zn complexes.^{32–35} Fluorescein derived sensors have now grown in popularity to avoid this issue.^{28,36,37} Some common examples include a popular set of Zn sensors named the “Zinpyr” or ZP family. ZP1-ZP10 are 10 examples of synthesized dyes that have been extensively characterized and tested with the goal of Zn quantitation within cellular environments.^{36–44} A few examples of this family of fluorescent probes are shown in Figure 1.

The biggest issue with fluorescence measurements is the stability of the sensor.⁴⁵ Fluorescent molecules will typically undergo rapid photobleaching after repeated on-off cycles

that causes a loss in signal.⁴⁵ For a robust sensing platform capable of being used for extended periods, fluorescence-based techniques are clearly inadequate. For this reason, absorbance methods are a better choice for this application because they are inherently more stable.⁴⁶ However, absorbance methods have been few in number for process monitoring applications because of their poor sensitivity in determining ppb-levels of heavy metals. Using dyes that have high ϵ values and proper method development, practical methods are possible.

1.3 Process Monitoring

Because challenges exist when developing a sensor for process monitoring, a practical method for real-time quantitation of metals at low levels in process streams is currently unavailable. Key aspects that must be considered are the sampling technique, concentration, matrix complexity, response times, and longevity of the sensor.⁴⁷ The sampling technique is a crucial consideration, which can vary from in-line, off-line or on-line.⁴⁸ When performing in-line analysis, the sensor is placed directly within the process stream so that the sample flows over the surface of the sensor. For off-line measurements, an aliquot of sample is collected and then taken to a separate location for analysis. Finally, on-line analysis is more similar to in-line analysis in that the chemical measurement is done near the process line. The sample is collected from the process stream and transported to the nearby instrument for measurement. On-line monitoring is typically used when some type of sample pretreatment is necessary to obtain a reliable response. The wastewater matrix is complex, and factors such as pH, conductivity, temperature, and turbidity can complicate matters, so filtering is needed. As mentioned earlier, there are no current affordable methods for real-time quantitation of metals in process streams. The goal of this project was to develop a reliable, sensitive, responsive, and rugged on-line process monitoring instrument to

quantify sub-ppm levels of heavy metals in wastewater over extended periods of time using novel azo-based metal-binding dyes.

1.4 Azo Dyes in Quantitative Analysis

Azo dyes have been used for many years because of their selective binding of heavy metals and consequent spectral properties of the dye-metal complex. They are the most popular chromophore in dye chemistry. They are commonly used in the textile industry⁴⁹, as food colorants⁵⁰, as pH sensors⁵¹, and in medical/pharmaceutical applications⁵². PAN and PAR are two well-known and commercially available dyes that bind to metals (Figure 2). Work has been done to determine their acidity constants and investigate the metal complexes formed.^{53–55} Using these dyes, a library of dyes was created for heavy metal sensing.

The covalent attachment of the dye molecules to a solid support is critical in creating a robust sensor. PAR possesses a non-ligating hydroxyl group in the *para* position, which can be utilized for covalent attachment to the support. However, PAN lacks a non-ligating moiety for this purpose, so a derivative (PAN-7OH) was devised for covalent attachment. Furthermore, PAN-7OH exhibits unique spectral characteristics that differ from the parent molecule, PAN, and therefore was investigated extensively.

Full characterization of these dyes is essential in developing a sensor. The metal responses must be carefully explored to identify possible interferences that can hamper the ability to measure the analyte accurately. Following the previous work on PAR and PAN,^{54–56} in this work, multivariate analysis was used to characterize their complexation with heavy metals. The acid dissociation constants (pK_a values) were evaluated to identify those pH regions where metal complexation would be optimal. Because the binding site contains an oxygen that can be

protonated, there is a competition between the proton and the metal ion at low pH. Additionally, the metal-dye stability constants were calculated in a similar fashion because it is critical to understand the strength of binding for the metal analytes.

1.5 Sensor Dye Films and Arrays

Using a set of azo dyes that have been developed based on PAN and PAR, the development of an on-line process monitor for heavy metals was undertaken. These dyes were extensively characterized to determine their pK_a values, binding characteristics, and stability constants for the metal ion analytes of interest. Thoroughly characterizing the dyes in this manner is the foundation for developing a robust sensing platform and optimizing it for specific applications. First, to successfully produce a sensor capable of being robust and reusable, the dyes must be attached to a solid support. This was accomplished by incorporating the chemosensors into hydrogel polymers that would, in turn, be covalently attached to glass.⁵⁷ Some of these dye films have been continuously tested for 8 months or more and most of them have proved to be robust, sensitive, selective, and repeatable in their response to specific metals. This is in stark contrast to similar studies in which the dyes were adversely affected by the process stream within hours.⁵⁸⁻⁶¹

Creating specific sensors with high selectivity is difficult because these dyes do not respond exclusively to a single analyte. Therefore, to quantify individual metals simultaneously, a method exploiting the spectral selectivity for dyes that bind and respond to multiple metals was needed. Different metal binding characteristics exist for each dye and specific spectral features can be used to differentially quantify metals in a mixture. This approach requires full spectra to be obtained and processed using chemometric (multivariate) analysis.

1.6 Multivariate Analysis Overview

Multivariate analysis is useful when characterizing the spectrophotometric response of dyes to metal binding.^{54,55,62,63} A multivariate analysis approach has several benefits in these applications. First, it is not productive to collect spectral data that will ultimately not be used in providing information.⁶⁴ In addition, instrumental noise has less impact on the computed values, assuming the noise is normally distributed. Moreover, the “model must fit the data at all wavelengths simultaneously”,⁶⁵ and therefore systematic error, interferences, and unknown species are revealed when significant deviations are revealed in the reduced spectra. A multivariate approach is also practical given the wide availability of multi-wavelength instruments, such as charge-coupled devices (CCD) and photodiode array (PDA) spectrophotometers, and the computational power of desktop computers. Finally, the multivariate approach can be used with complex equilibrium models or kinetics models without limitations on the number of chemical species, include “spectroscopically invisible” species, utilize known spectral profiles, and can be employed with other spectroscopic techniques.⁶⁶

Two distinct multivariate methods were used to analyze the absorption spectra of sensors and their metal complexes in this work, and these methods can be divided into two categories. A hard model is based on first principles and relies on the mathematical relationship among variables that can be derived or measured,⁶⁷ such as the Beer-Lambert Law for absorbance spectroscopy. A soft model is based on the variation and correlation in the data.⁶⁷ Soft models can be used in an exploratory fashion to determine which variables are significant and relevant for describing a system or used in a semi-empirical fashion for making predictions with a system. In the work described herein, the chemical equilibrium of two sensors was investigated using a hard-modelling approach by performing regression of the spectra with well-defined physicochemical models. A

soft-modelling approach was used with the sensors to predict the metal ion concentrations in an aqueous mixture using its absorbance spectrum. Although a hard model would seem more appropriate for quantification, the open-endedness of a soft-model can cope with noise, random error, baseline issues, unknown interferences, etc. Both analysis methods will be briefly described in this section.

1.7 Modeling Equilibrium Constants with Multi-Variate Analysis

Equilibrium constants can be determined from spectroscopic measurements. Consider an example where a metal (M) binds to a sensor (L) to form a complex (ML) to establish equilibrium. Also, L and ML have unique absorption profiles whereas M does not absorb light in the region of interest. A sample of L is titrated with M, and the absorbance spectrum is recorded at each titration step. Figure 3 shows a three-dimensional plot of the absorption data from this example experiment where the absorption band decreases for L and increases for ML as the sample is titrated with M. In the univariate or single-wavelength approach, the concentrations of L and ML can be determined from the two peak absorbance values by applying the Beer-Lambert Law if the molar absorptivity coefficients, ϵ , and the optical pathlength, l , are known. Subsequently, the equilibrium constant for the system can be determined by using non-linear regression. A diagram illustrating this process is shown in Figure 3.

A multivariate approach can be implemented using the entire spectrum by arranging the data into a matrix where the rows represent wavelength and the columns represent reagent concentration. This data matrix is the result of the concentration and spectral profile (ϵ) of each species during the experiment according the Beer-Lambert Law, which can also be expressed in matrix notation as illustrated in Figure 3. The concentration of each species can be determined

using linear algebra, and the equilibrium constant(s) can be determined with non-linear regression in the same manner as the univariate case. Several software packages perform this type of analysis with a variety of measurement techniques, including potentiometry, nuclear magnetic resonance (NMR), and other spectroscopies,⁶⁸ A similar analysis can be performed for kinetics measurements using the kinetics package. For example, Maeder and colleagues have reported theoretical multivariate approaches in the determination of equilibrium and kinetics parameters from spectral data.^{65,66,69}

1.8 Quantitative Analysis Using Multi-Variate Analysis

A multivariate approach is also advantageous for quantitative analysis using spectroscopic data, such as the detection determination of multiple metals in a mixture with a single sensor. However, the application of multiple linear regression (MLR) with full-spectrum calibration data is often unsuitable and may yield unsatisfactory results.^{70,71} First, the spectral data matrix must be “full rank” in that it must contain more rows than columns. Hence, this matrix must contain more calibration samples (rows) than wavelength values in the spectrum (columns). Also, the data values in a column must be independent for MLR, and spectroscopic data is often highly correlated (i.e., multi-collinear). Thus, MLR can only be performed at a select number of wavelengths. In addition, experimental noise can create numerical instabilities, and the results may be sensitive to variations in the noise.

Partial Least Squares (PLS) analysis, also known as Projection of Latent Structures, is a multivariate soft-modeling approach used in many disciplines, including the social, natural, and physical sciences.⁷² PLS assumes that a small number of underlying latent variables can relate two datasets, and the latent variables are not assumed to be independent. In short, PLS creates latent

variables that maximize the covariance between two datasets for prediction.^{73,74} More importantly, the latent variables are orthogonal, which solves the multi-collinearity problem. Also, PLS can be used with datasets that are large, contain noise, and/or have missing values.⁷⁰

PLS shares aspects of Principal Component Analysis (PCA) and principal component regression (PCR), such as dimensionality reduction, but these methods have important distinctions. PCA decomposes the data matrix (X) to obtain principal components that retain as much of the variation in X as possible, and PCR seeks principal components from X that best predict the output matrix (Y).⁷³ PLS seeks vectors that maximize the covariance between X and Y to best predict Y . These vectors are referred to as latent variables and not principal components. Also, the PLS scores are rotated relative to the PCA result.⁷⁵

The specific procedures for performing PLS regression depend upon the algorithm used, like Nonlinear Iterative Partial Least Squares (NIPALS) or SIMPLS^{76,77}, and various other methods described in the literature^{76,77}. A general overview of PLS regression is illustrated in Figure 4. A set of calibration samples is prepared, and spectra are obtained for the standard and unknown samples. X is the data matrix containing the calibration spectra where the rows represent wavelength and the columns represent an index for standard. Y is a factor matrix containing the concentration values for each target analyte (across the rows) for the corresponding calibration standard. Typically, the calibration data, X and Y , is mean-centered and scaled to have unit variance to remove bias from data with different ranges and units, ease computations, and improve numerical stability.^{78,79} The data in X and Y are decomposed into the scores (T and U), loadings (P and Q), and residuals (E and F) respectively. The score and loading coefficients transform the original data onto a subspace. The algorithm extracts scores in a manner that maximizes the covariance between X and Y . Regression of the scores (T and U) yields an estimate of the latent

variable with the regression coefficients B . Then, the latent variable is subtracted from the data removing its contribution, referred to as deflation.^{73,80} The process is repeated sequentially with the remaining latent variables until the errors are minimized. Also, another routine can be employed to select the number of relevant latent variables so the prediction quality is greatest without overfitting the noise in the data.⁷³ The resulting coefficients (B) can be re-expressed as regression coefficients β and β_0 for making direct predictions with new spectral data,⁷¹ such as predicting metal ion concentrations in an unknown mixture using a sensor and corresponding absorbance spectra.

1.9 Partial Least Squares

Partial Least squares (PLS) is a modeling technique for building predictive models, and it has been applied to a variety of spectroscopic methods. For example, PLS has been used to study heavy metals in a wide variety of difficult sample matrix, including: activated charcoal using graphite furnace atomic absorption spectrometry (GF-AAS) and inductively-coupled plasma optical emission spectrometry (ICP-OES)⁸¹, dental amalgams using potentiometric sensors⁶³, freshwater sediment with near-infrared (NIR) reflectance spectroscopy⁸², and aqueous samples using NIR transmission spectroscopy.⁸³ Also, PLS has been used to investigate Pb distributions in soils using AAS,⁸⁴ and the determination of heavy metals in soil using ICP-OES⁸⁵ and UV-Vis-NIR spectroscopy.⁸⁶ Additionally, PLS has been applied to biological samples, including the study of Cd and Zn in mussels using NMR,⁸⁷ Cd, Cu, and An in seabream fish using IR and Raman spectroscopy,⁸⁸ and Cr in plant leaves using laser-induced breakdown spectroscopy (LIBS).⁸⁹

Predictive modeling techniques have been widely used for sensors that measure heavy metal by UV-Vis absorbance spectrophotometry. These sensors typically exhibit a semi-selective

binding to metal ions, but also often exhibit a unique spectral response for each metal, which can be utilized for sensor characterization and the analysis of mixtures using a multivariate analysis approach. Ghasemi *et al*, has studied the protonation equilibria of PAR and its complexes with Al, Cd, Cu, Fe, Ni, and Zn.^{54,56} PAR was used in the simultaneous determination of Cd, Pb, Hg, and Zn using PLS and principal component regression (PCR), although the work was focused on the preprocessing of spectral data spectra, such as wavelet transformations and normalizations for more accurate results.⁵⁶ Mixtures of Cd, Cu, and Hg were determined using three sensors and prediction via artificial neural network (ANN).⁶² PAN was used in the determination of Co, Cu, and Ni in vitamin tablets and foodstuffs using continuous wavelet transformation (CWT).⁹⁰ PAN and PAR were included in an array of seven sensors that identified thirteen metals and quantified mixtures with five metals using hue-saturation-value (HSV) color values from an image sensor and prediction with an ANN.⁹¹

Through the power of multivariate data analysis, the individual dyes can be characterized and applied to quantitating multiple metals simultaneously. In this work, several azo dyes were investigated for use as heavy metal absorbance sensors. The protonation equilibria, metal binding affinities, and decomplexation under acidic and alkaline conditions were studied with a multivariate approach. Also, PAR and QAR were used for the simultaneous determination of mixtures containing Cu, Pb, Ni, and Zn using PLS. Replicate samples were used to estimate the accuracy and repeatability this approach for sensing applications.

1.10 Continuous Flow: Flow Injection Analysis (FIA)

Application of the sensor chemistry to an on-line process monitor requires the development of a continuous flow-based instrument. Of the approaches used over the past four decades, Flow Injection Analysis (FIA) has emerged as the preferred technique.⁹² In FIA, discrete sampling is achieved through injection of an analyte into a flowing stream. FIA is based upon the principles of flow dynamics and consequent dispersion of injected zones in a microscale flow manifold. In simple FIA, microscale volumes of samples and reagents are precisely manipulated through narrow-bore tubing to a detector. The basic manifold for an FIA instrument is shown in Figure 5. The components have great flexibility and many different experimental designs can be developed to fit the application.

FIA is efficient because the methods are typically fast and sampling can be done quickly (>100 samples per hour is not uncommon).⁴⁷ Another advantage of FIA is the ability to perform chemical analyses that are difficult by conventional methods. From injection, sample processing, and detection, FIA has many experimental options available. The injected sample can be processed in several ways such as pre-concentration, separation, dilution, or media exchange.⁴⁷ This makes FIA an ideal analytical tool for a vast number of applications such as chemical refining, biotechnology, manufacturing and environmental process monitoring. FIA is based upon the principles of flow dynamics and consequent dispersion of injected zones in a microscale flow manifold. In simple FIA systems, microscale volumes of samples and reagents are precisely manipulated through narrow-bore tubing to a detector. The basic manifold for an FIA instrument is shown in Figure 5. The components have great flexibility and many different experimental designs can be developed to fit the application. An example of the application for FIA to multiple

analytes and methods was shown in the work done by Balconi, *et al.* in 1990 evaluating detection methods for ammonia, Cu, hydrazine and other components of water in power-plant cycles.⁹³ The reaction methods previously shown to work were tested in a FIA setup and the ability to field deploy to power plants was explored.

1.11 Sequential Injection Analysis (SIA)

Sequential Injection Analysis (SIA) is a variation of FIA that was reported in 1990 which has significant advantages for process monitoring.^{47,94} SIA has simpler componentry than FIA and the two are sometimes referred to interchangeably. The implementation of flow schemes differs in that SIA has bi-directional flow, whereas in FIA the flow is uni-directional from the carrier. Figure 5 shows a comparison between FIA and SIA. SIA uses bi-directional flow dynamics to its advantage in experimental design. Consider the simple example shown in Figure 6 of an analyte (A) and reagent (R) reacting to form product (P). SIA creates radial and axial dispersion profiles that can aid in mixing and dilution of the liquids within the tubing. SIA gives some extra flexibility in reactions and processes that can be carried out. Regardless, the principles and results are still the same for FIA and SIA.

SIA instruments are simple in design and more versatile than FIA designs. Processes that can be performed include filtering, preconcentration, separation, and de-gassing.⁴⁷ The applications for SIA are also numerous because the design allows for simple modifications to methods without re-configuring the entire system, as would be necessary in FIA. Comparable to FIA in performance, results are typically acquired in a short amount of time (15-60 s), with small sample volumes (1-100 μL), and with high precision (typically <5% RSD). Additionally, the

hardware is much simpler and therefore more robust than FIA. A computer interface is used to accurately control the system and acquire data. Many practical applications for SIA have been reported in the past three decades.^{47,95–98} An example of SIA process monitoring is the application to the quantitation of TNT in aqueous and soil samples for a remediation site. TNT was measured using a molecular absorbance spectrophotometry (VIS) method with in-line solid-phase extraction, and a LOD of $0.5 \mu\text{g mL}^{-1}$ in aqueous samples and $80 \mu\text{g g}^{-1}$ in soil samples was observed.⁹⁹ Another application is the measurement of sulfuric acid in 1-butanol samples with in-line titrations.¹⁰⁰ The microscale titration developed demonstrated the ability for SIA to be used to monitor phenomena related to pH. This application also demonstrated the capability of SIA instruments to load and dispose of column resins readily which improves automation capability. SIA devices are flexible and can be used beyond one application. Components may need to be added/subtracted but the core components such as the pump and MPV can be used in many experimental designs.

In the work described herein, two types of flow systems were studied: conventional and SIA. The conventional system is large scale with wide tubing and high flow rates. The SIA instrument and method were developed for testing and evaluating sensor films as well as to explore a microscale approach, in contrast to the antiquated design used in the conventional system. Because SIA is automated, it is convenient for testing the effects of method factors on the binding of metals by the dyes. The SIA instrument used in this work consisted of a holding coil between the carrier and MPV and a flow cell designed to house the dye films. The MPV was used to feed different samples with factors (pH, [M], μ , etc.) altered. The flow cell was a Z-cell design with a cavity for holding the sensor. The flow cell also had optical component housings for measurement of the response. The device was controlled via a computer interface and data was processed.

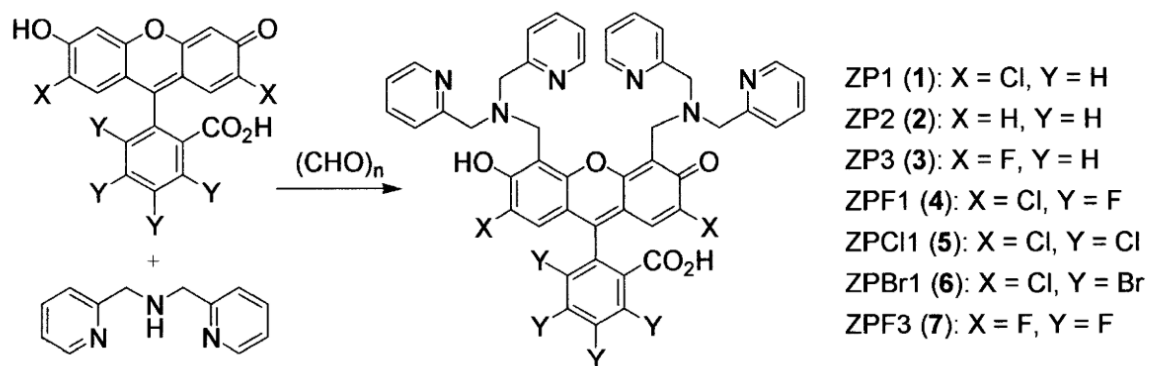


Figure 1: Synthesis of ZP family fluorophores. Changing the “X” and “Y” groups yields a fluorophore with unique excitation/emission wavelength, pK_a, and K_d values.³⁸

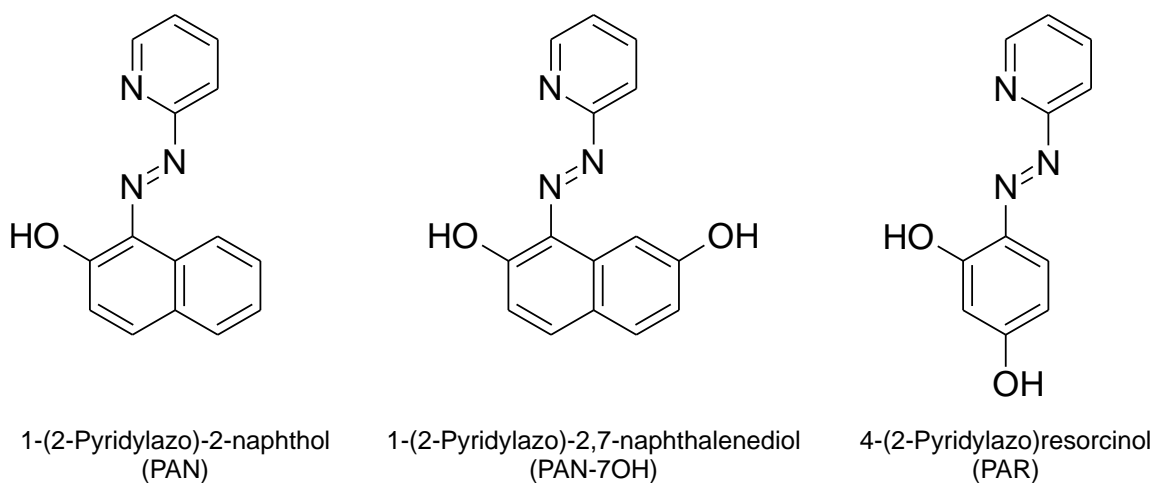


Figure 2. Chemical structures of commercial azo-based sensors (PAR and PAN) as well as the focus in this work (PAN-7OH). The conjugation and moieties lead to a change in spectral characteristics and responses of the dye.

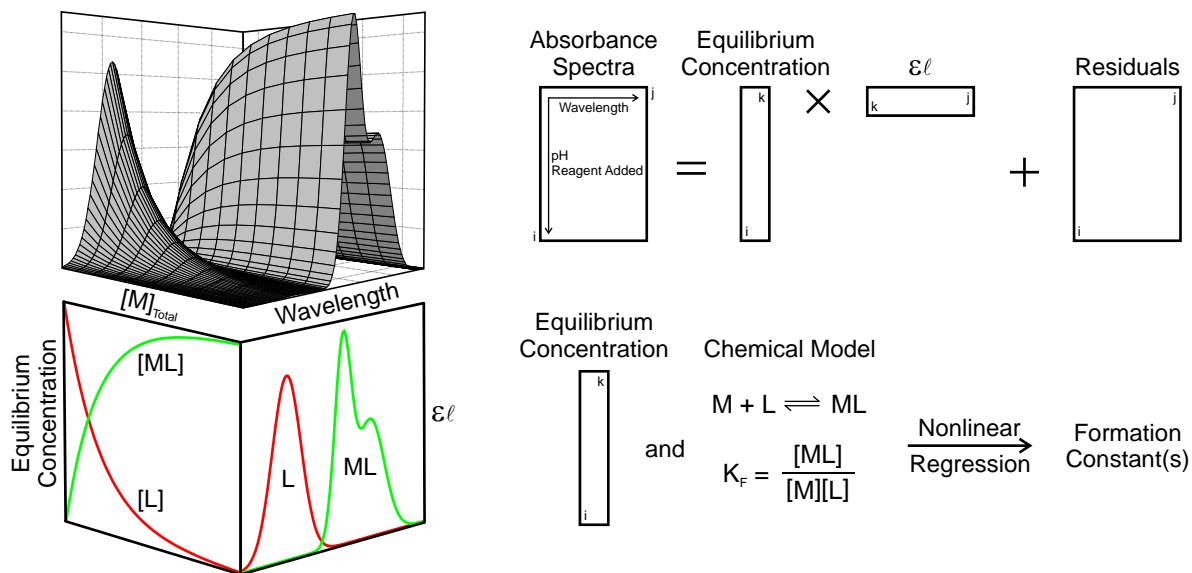


Figure 3: Illustration of multivariate analysis approach for the determination of equilibrium constants from absorption spectra adapted from Reference 65⁶⁵. Graphical illustration (left) shows the variable space where the complex formation $[ML]$ leads to a decrease in signal for the free dye $[L]$ and in an increase in signal for ML . The spectral data is iteratively fit to a model to minimize residuals and calculate equilibrium concentrations which are used to find the formation constants from nonlinear regression

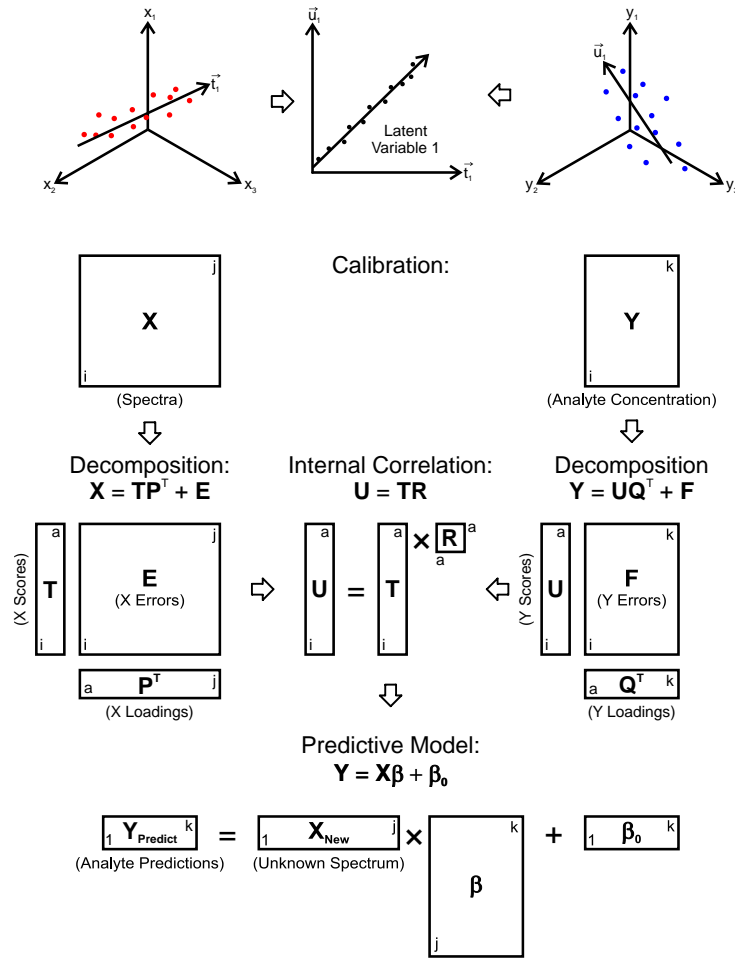


Figure 4. Illustration of projection of data onto subspace for determining latent variables and PLS regression for building a predictive model. Matrix dimensions are denoted with a lowercase letter. A portion of the figure was adapted from references 78, 101, and 102^{101,102,78}.

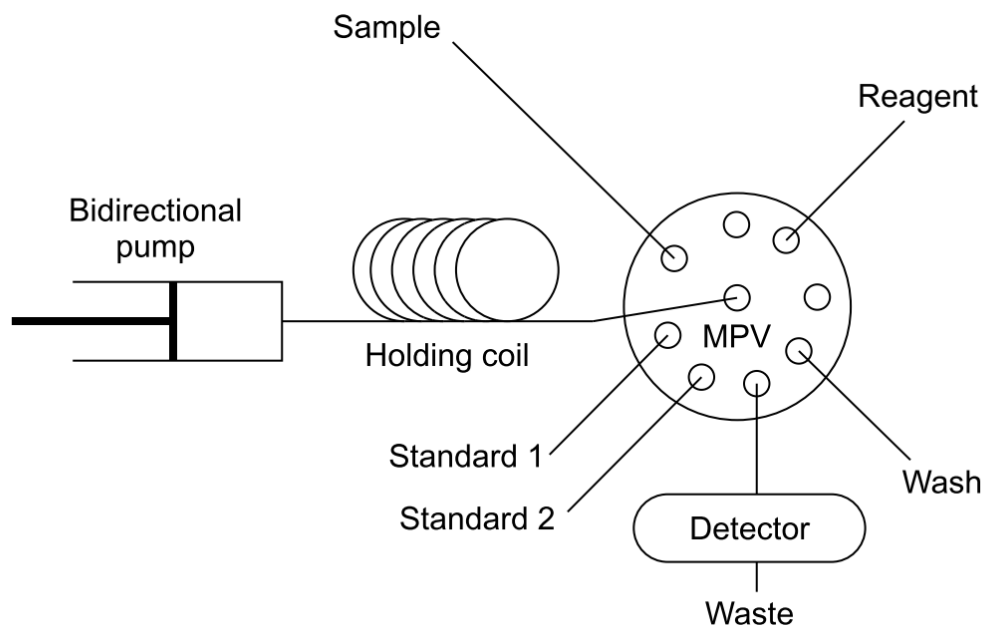
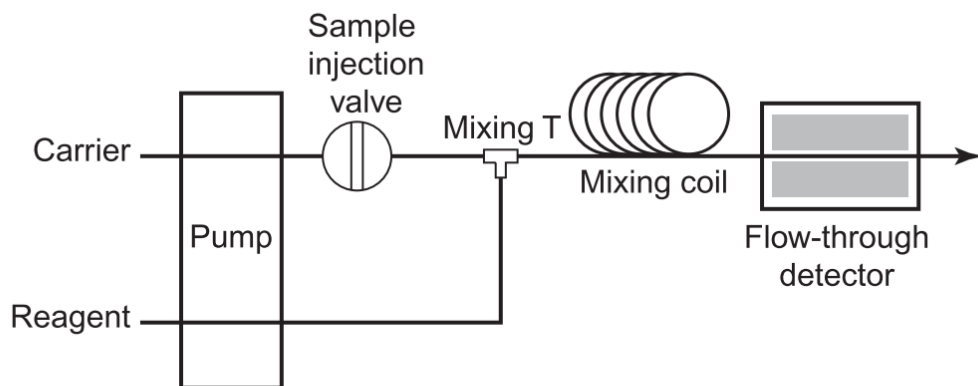


Figure 5: Schematic diagram of FIA (top) and SIA (bottom) instrument designs. In FIA, the flow is unidirectional, and a sample “plug” is injected into the carrier via a valve. The pumps used in FIA are typically peristaltic and the solution is taken through a mixing coil to improve homogeneity. In this example, there is an additional reagent line that mixes with the sample before the mixing coil. In SIA, the pump is bidirectional (syringe) and a multiposition valve (MPV) is used to stack reagent “zones” in the holding coil before dispensing them to the detector. These zones disperse and mix to a certain extent as they travel to the detector.

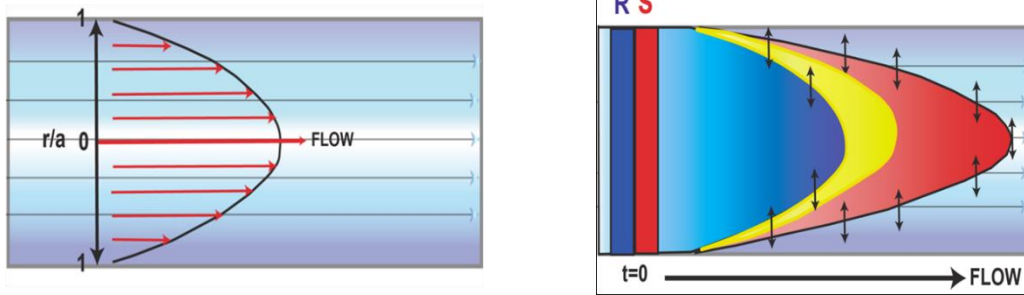


Figure 6: Dispersion profile created in FIA/SIA that forms a concentration gradient. When a sample zone (red) is in contact with the reagent zone (blue), a product zone (yellow) forms between them. This sandwiched zone is then sent to the detector. The size of this zone can be controlled by flow rates, volumes, tubing dimensions, etc.¹⁰³

Chapter 2: Experimental

2.1 Materials

2.1.1 Reagents

1-(2-Pyridylazo)-2-naphthol (PAN) and 4-(2-Pyridylazo)resorcinol (PAR) were purchased from Sigma Aldrich (Milwaukee, WI, USA). Standard metal solutions were prepared by dilution of 1,000 ppm (mg L^{-1}) atomic absorption standards (Sigma Aldrich). Stock dye solutions were typically prepared in Spectro grade methanol (Acros, Pittsburgh, PA, USA) or dimethyl sulfoxide (DMSO) (Fluka, Waltham, MA, USA). Buffers were prepared in the respective range using hydrochloric acid, potassium chloride, citric acid, sodium acetate, acetic acid, 2-(N-Morpholino)ethanesulfonic acid (MES), 3-(N-Morpholino)propanesulfonic acid (MOPS), 4-(2-Hydroxyethyl)-1-piperazinepropanesulfonic acid (EPPS or HEPPS), 2-(Cyclohexylamino)ethanesulfonic acid (CHES), 3-(Cyclohexylamino)-1-propanesulfonic acid (CAPS), and sodium hydroxide, and were purchased from Fisher Scientific (Beverly, MA, USA), MP Biomedicals (Santa Ana, CA, USA), Sigma Aldrich, and VWR (Radnor, PA, USA). Early experiments revealed an interference caused by trace metal impurities in the buffer reagents, so the buffer reagents were treated with Chelex 100 ion-exchange resin (Bio-Rad, Hercules, CA, USA) to remove these impurities.¹ Triton X-100 surfactant (Sigma Aldrich) was used to reduce scattering when aggregation was present. Reagent water with a resistivity of $18.2 \text{ M}\Omega \text{ cm}^{-1}$ was used for all experiments. Solvents used for the solvatochromism study included DMSO, acetonitrile, acetone, dimethyl formamide, pyridine, ethyl acetate, diethyl ether, triethylamine, chloroform, toluene, dichloromethane, methanol, ethanol, isopropanol, tert-butyl alcohol and were purchased from the same vendors as the buffers listed above.

2.1.2 Buffer Preparation

Preparation of the buffer solutions was done in one of two ways. In the first case, the 0.10 M buffer components (acid and basic salt) were prepared separately by dissolving into reagent water. These solutions were then mixed and adjusted to the desired pH. In second case, the buffer is prepared in one container by mixing the acid and basic salt at a ratio that would yield the desired pH. In both cases, these solutions were treated with Chelex 100 and then 2 mM Triton X-100 was added. EPPS, CHES, and CAPS were adjusted with 1 M NaOH was used to adjust their pH to the values required since the basic salts were not purchased.

2.1.3 Labware

Plastic labware was used to minimize interference from metal impurities. Samples were typically prepared in Class A volumetric flasks (VITLAB PMP, Grossostheim, Germany). All labware was cleaned using Citranox detergent (Alconox, White Plains, NY, USA). Additionally, glassware was immersed in 2% (v/v) nitric acid overnight and then rinsed with reagent water to remove metal contaminants. Eppendorf micropipettes were used for transferring small volumes. Spectroscopic cuvettes (1.0 cm) were either polymethylmethacrylate (PMMA, VWR) or Spectrosil™ quartz (Fisher). Long path cells (10.0 cm) were used for affinity studies (Starna Cells, Atascadero, CA, USA). Either glass or Spectrosil™ quartz cuvettes were used depending upon the spectral region in which the dye absorbed light.

2.2 Instrumentation

Ultraviolet-visible (UV-VIS) absorption spectra were recorded using either a Perkin-Elmer Lambda Model 650 spectrophotometer (Waltham, MA, USA) or StellarNet Black Comet spectrometer equipped with thermoelectric cooling (Tampa, FL, USA) and a tungsten-halogen (WX) and deuterium lamp. Schematic diagrams of the Lambda 650 and the Black Comet spectrometers are shown in Figure 7 and Figure 8, respectively. A Symphony pH meter from VWR was used for pH measurements.

The initial flow system, referred to as the "conventional" design, had three flow lines controlled individually by three peristaltic pumps (P). The lines were used for sample, buffer (0.10 M MOPS buffer), and acid (0.10 M HCl). The lines were connected to a T intersection (T) and flow continued through a flow cell (FC). The flow cell contained a slot in which a cartridge was placed that held the dye that was covalently bound to glass. The source (S) was a StellarNet tungsten-halogen lamp and the detector (D) was a StellarNet "Black Comet" series spectrometer.

2.3 Flow Studies Using the Conventional System

2.3.1 Flow Cell Design

The flow cell was designed so that the liquid flow was parallel to the film. The source was a StellarNet W/Kr lamp and the detector was a StellarNet CCD. The film thickness was 25.4 microns and the films were covalently attached to a glass microscope slide (1 mm thick) which occupied a compartment that was machined into in the body of the cell. For metal quantitation experiments, the film was cleaned with 0.10 M HCl and then equilibrated to pH 7.0 with 0.10 M MOPS buffer. These steps were optimized based on the particular film under study and were done

long enough for the baseline to become steady (~1 min). The acid and buffer washes were done at high flow rates ($>10 \text{ mL min}^{-1}$). Samples, prepared in 0.1 M MOPS unless otherwise stated, were introduced to the flow cell at 4.7 mL min^{-1} . The absorbance at λ_{max} vs time was plotted for data analysis.

2.3.2 Flow System Configuration.

Initially, a single-pump design in which high flow rates ($>4 \text{ mL min}^{-1}$) and large tubing ($>6 \text{ mm i.d.}$) was used to study the characteristics of the chemosensor dyes (Figure 1). Acid, buffer, and sample solutions were introduced sequentially by manually moving the tubing to the containers. The system was modified with the addition of two pumps (Figure 2). Thus, the acid, buffer, and sample solutions were pumped independently. A T-junction valve was used to connect the lines to the flow cell, that is, two of the lines (acid and buffer) shared a line before the junction. This caused carry-over, unlike the original manual design. The system was then modified by replacing the T-junction with an X-junction valve (Figure 3). This eliminated the common line for the buffer and acid prior to the T-junction. By replacing the T-junction with a X-junction, the pump system was again modified so that carry-over was eliminated (Figure 3). This final configuration, with independently pumped solutions and the X-junction valve, significantly improved the response and minimized artifacts (e.g., carry-over).

2.3.3 Quantitation Method

The general method for the conventional pump system involved introducing acid, buffer, and sample to the flow system. First, 0.1 M HCl was added at a large flow rate ($>20 \text{ mL min}^{-1}$) to

rinse the film and remove any bound metal. This typically took ~1 min to see no change in the spectral response. The film was then equilibrated with 0.1 M MOPS buffer (pH 7.0) to get it in the correct state for binding. This typically took 2-5 min to ensure the film was not changing protonation states. The baseline spectrum was taken and sample was then run through the flow cell while collecting a spectrum every minute. Samples were typically prepared in 0.1 M MOPS buffer (pH 7).

2.4 Flow Studies Using Sequential Injection Analysis

2.4.1 Flow cell design.

As an alternative to the conventional design, a Sequential Injection Analysis (SIA) system was studied. A schematic diagram of the SIA instrument is shown in Figure 12. Unlike the conventional design, SIA is a microscale approach to continuous flow analysis that is based upon a single bi-directional pump and multi-port selection valve. The flow cell for the SIA differed from the previous conventional design, as depicted in Figure XX. The flow cell was designed to incorporate the flow path of a conventional z cell but also had a well drilled in that was 1.076 mm thick to accommodate the 1 mm thick glass slide, the 25.4 micron thick film, and have a small excess. The flow would come in at the film and be dispensed to waste. The optics would be in line with the film to measure the absorbance of it.

2.4.2 Flow System Configuration.

The flow cell had excess space in the well because the depth was drilled with excess and depending on the exact cut of the glass slide, there was room on the sides also. A small piece of polyethylene tape (76.2

microns) that had a hole punched in it was placed over the film for several reasons. The tape served as a gasket for the cell, eliminated dead volume on the sides of the glass, and kept the film aligned with the optics. The flow was originally brought in at the 90° angle to the film but this caused film destruction more often. The flow coming in at the 45° angle was less destructive.

2.4.3 Quantitation method.

The method used for analysis involved 3 steps much like in the conventional flow system. First, the film would be rinsed with 0.1 M HCl to remove any metal. Then, the film would be equilibrated with 0.10 M MOPS (pH 7 with 2 mM Triton X-100). The baseline would be taken, and the buffered metal solution would be introduced. It was found that the flow rate should be kept under 20 $\mu\text{L s}^{-1}$ to avoid film delamination. The typical procedure was an acid wash of about 3 mL at 15 $\mu\text{L s}^{-1}$ was followed by carrier solution (buffer) at the same rate. The metal solution was then aspirated and dispensed. Typical volumes were 4.5 mL at a flow rate of 12 $\mu\text{L s}^{-1}$. The procedure was altered slightly based on experimental conditions.

In typical operation, after initially priming each line with the respective solution, the flow cell was washed with ~2 mL of 0.1 M HCl to remove metal, followed by ~4 mL of buffered carrier to equilibrate the protonation sites on the dye at neutral pH. Each time a new film was placed in the flow cell, the metal capacity ("loading") for that particular dye and metal analyte was determined. Additionally, the extent of washing the dye that was necessary to efficiently remove the metal also had to be adjusted.

Damage to the film at high flow rates was avoided by limiting the flow rate to $\leq 20 \mu\text{L s}^{-1}$. The amount used for the acid wash and buffer equilibration steps was therefore tailored to each

film. Typically, a volume of 2.00 mL was used for each step and adjusted accordingly as monitored by absorbance changes.

2.5 Treatment of Error

Error propagation was examined in the classical manner. Error in the K values was calculated by accounting for experimental error and adding it to the regression error that was calculated by the model. One source of error was the Symphony pH meter, which had errors of ± 0.02 and ± 0.002 for the probe and meter, respectively. Measurement of the temperature using the ATC probe (± 0.001) was also a source of error.

Additionally, calibration standards were prepared from solutions that had an uncertainty of ± 0.01 pH units (as specified by manufacturer). Other experimental uncertainties also existed in the reagents and laboratory processes. There was uncertainty in the initial dye concentration relative to the volumetric flasks (e.g., ± 0.002 mL) and scale used for weighing by difference (± 0.0001 g). The absorbance uncertainty was measured as ± 0.001 by measuring absorbance through a dichroic filter. The pathlength relative uncertainty was ± 0.001 , as specified by the cuvette manufacturer. Full error propagation calculations can be found at the end of the experimental. Error Propagation for the ReactLab Experiments is found in Appendix I.

| pH Region | Acid | Base |
|-----------|-------------|------------------|
| 1.0-2.0 | HCl | KCl |
| 2.0-4.0 | Citric acid | NaOH |
| 4.0-5.5 | Acetic acid | Acetate |
| 5.5-6.5 | MES acid | MES Sodium salt |
| 6.5-7.5 | MOPS Acid | MOPS Sodium Salt |
| 7.5-8.5 | EPPS | NaOH |
| 8.5-9.75 | CHES | NaOH |
| 9.75-11 | CAPS | NaOH |
| 11.0-13.0 | KCl | NaOH |

Table I. Buffers were prepared from acid and base (conjugate salt) in the region near the desired pH for a given experiment.

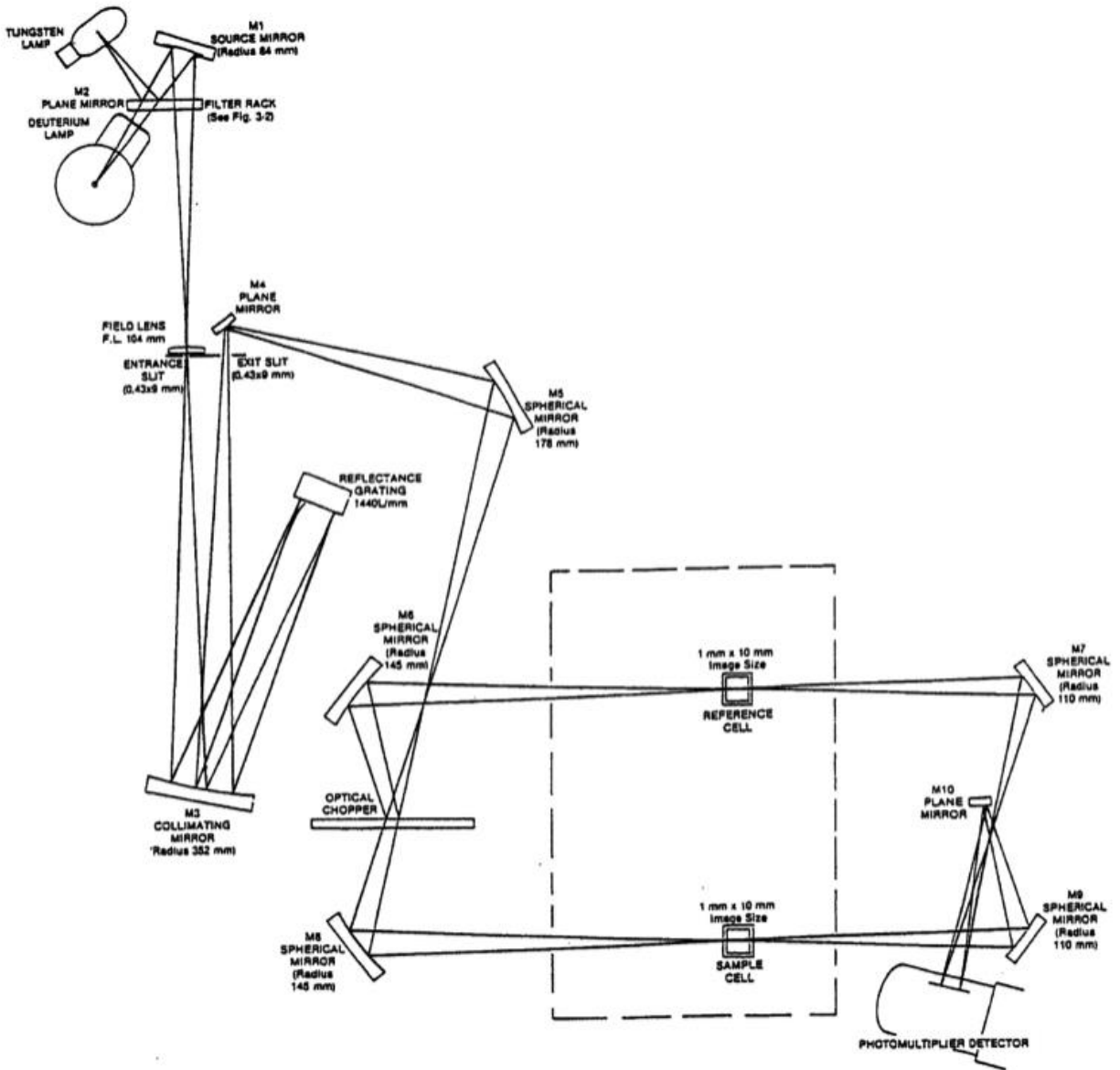


Figure 7: Schematic of the Perkin-Elmer spectrometer used in some UV-Vis experiments.

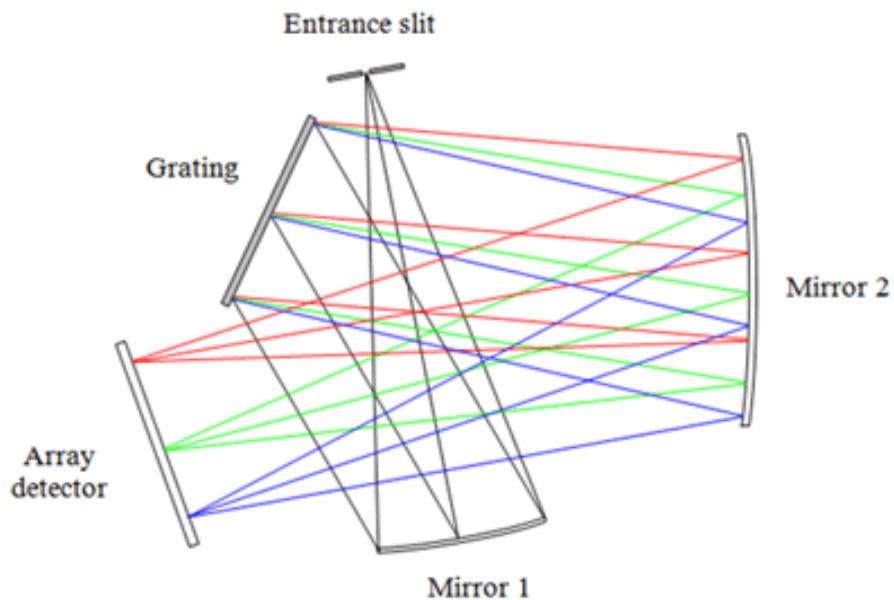


Figure 8: Schematic of the optical components (crossed Czerny-Turner) of the StellarNet Black Comet used in UV-Vis experiments.¹⁰⁴

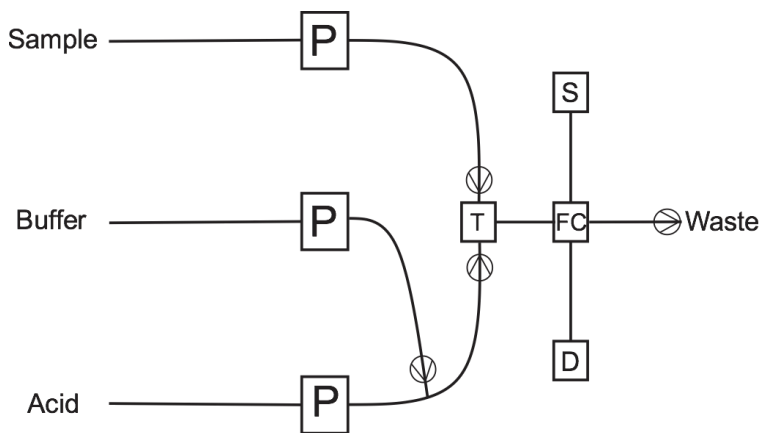


Figure 9: Conventional flow system (version 1) with combined buffer and sample flow lines.

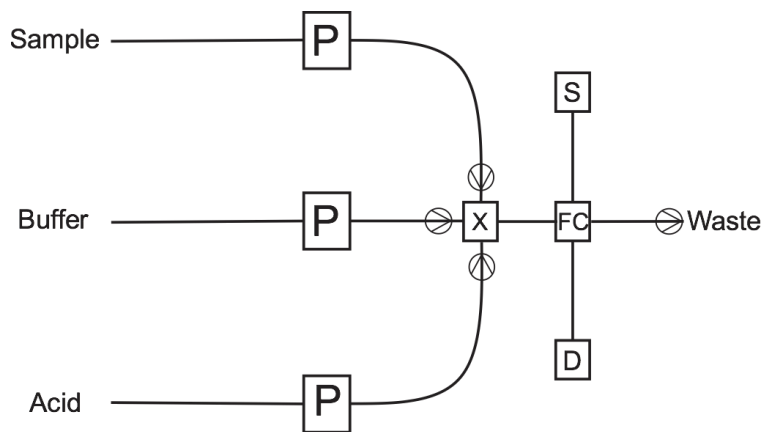


Figure 10 Conventional Flow System (version 2) with separate buffer and sample flow lines.

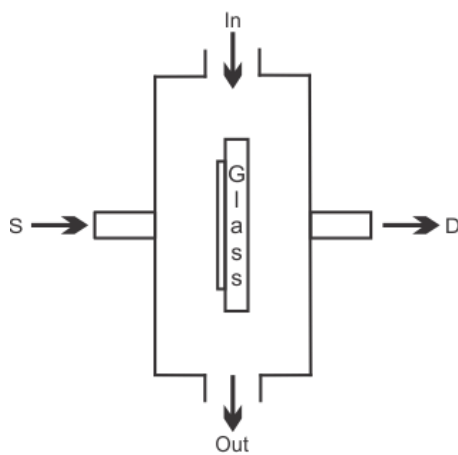


Figure 11: Schematic diagram of the conventional flow cell.

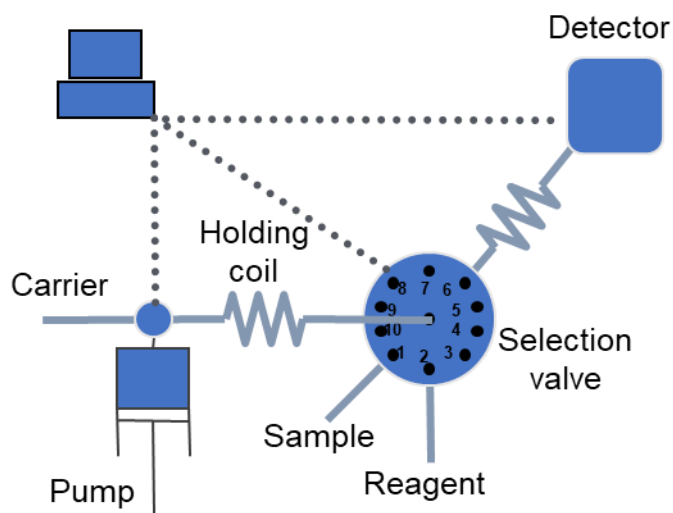


Figure 12: Schematic diagram of the SIA system.¹⁰³ The selection valve has multiple positions and is used to cycle between reagents, samples, standards, etc. The device is controlled via a computer interface that allows the user to easily manipulate zones of fluid to a detector.

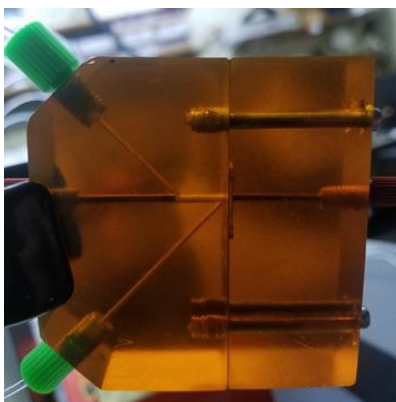


Figure 13: Picture of SIA flow cell showing optical path as well as the Z-type flow path

Chapter 3: Results and Discussion

3.1 Preface

This chapter will focus on the work done on the development of an optical sensing platform for heavy metals in aqueous samples. Azo dyes were synthesized by organic chemist collaborators. These dyes were characterized extensively to identify which were potential targets for a sensor array. The optical response to various heavy metals was tested, along with the binding characteristics for those which the dye was sensitive. For a given dye, it was shown that the protonation states of the free dye and metal complexes described can give insight into the effective pH range of the sensors. The modeling technique was applied to free dye samples with four different metals (Cu, Ni, Pb, and Zn) and was also tested for robustness. Two types of flow systems were tested with one dye. Zn was the metal focused on for initial testing. The more conventional flow cell with large volumes and flow rates was tested for response, repeatability, and flow rate effects. The microscale SIA design was used for extensive testing on the films. A flow cell was designed to house the dye attached to glass and allow optical and flow paths. The SIA flow system was used to test repeatability, robustness, as well as baseline, pH, and ionic strength effects. This information was used in development of a field-tested prototype with accurate and repeatable results.

3.2 Free Dye Characterization

The metal response was tested for various novel azo dyes in solution (or as the “free dye”). Stock solutions were prepared at ~5 mM in Spectro-grade MeOH, weighing them by difference. Alternatively, if the dye had low solubility in MeOH, DMSO or reagent water was used. To

determine molar absorptivity coefficients, "free dye" samples were prepared in a 1-cm PMMA cuvette with 0.10 M MOPS buffer (pH 7.0). Samples were typically made between 20-100 μM and used to gauge the proper concentration needed for the metal response testing. Based on the absorbance, most concentrations ranged from 20-350 μM . In some cases, 0.10M phosphate buffer (pH 7.0) was used for metals that complexed with MOPS. The metal was always kept in excess, assuming that 1:2 binding occurred.

The metal responses (absorbances) plotted for all dyes tested are shown in Figure 61 (Appendix 1). A table of the peak absorbance (λ_{max}) changes was constructed for viewing prospective dyes and the results are summarized in Table II. This information can be used to identify simply whether there was a significant response or not. Background subtraction was done in cases where excessive baseline shifting was seen. The absorbance at a longer wavelength (800 nm) where absorbance was negligible was subtracted from every data point. The information in this table is used to determine which dyes to further pursue. The table can provide a quick "snapshot" of the selectivity of a given dye for these metals. It can also be noted that most of these dyes did not show a response to Na^+ , K^+ , Ca^{2+} , and Mg^{2+} . These metal ions are commonly found in large quantities in water and would otherwise cause severe interference issues.

The responses of four different dyes are shown in Figure 14 and Figure 62. The dye that was most explored was PAN-7OH (Figure 14). This azo dye is structurally similar to commercially available PAN, although the spectral responses of PAN-7OH differ from those of PAN. The absorbance band(s) of the metal complexes with PAN are red-shifted relative to PAN-7OH. In many cases, the spectral profiles can differ greatly between the two sensors. For example, the absorption bands for the Cu(II) complexes have a similar shape but different λ_{max} values. The absorption bands for Co(II) are broad and weak for PAN while the shape and relative intensity are

noticeably different for PAN-7OH. Similarly, the absorption bands for the Ni(II) and Zn(II) complexes with PAN-7OH are more distinct than the corresponding absorption bands for PAN and PAR. Therefore, PAN-7OH has the greatest ability of the four azo sensors to distinguish Ni(II) from Zn(II) in a mixture. Although PAN-7OH is a structural analog of PAN, the distinctive spectral responses of its metal complexes can thus be employed to differentiate metal ions in a mixture.

3.2.1 Solvatochromism Study

Solvatochromism is the change in spectral response as a function of solvent polarity. Several dyes showed solvatochromatic properties during synthesis. To better understand the solvatochromic effect, the response of QAN-1,5OH (Appendix 1) to various solvents was studied. Quartz cuvettes were used in this case because the spectral response was observed across the UV-Vis region. Stock dye (104 μ L of 7.83 mM) was dissolved in 2.40 mL of solvent to yield a sample concentration of 325 μ M. The solvent was used as a blank and spectra were collected on the Stellarnet Black Comet spectrometer with the tungsten halogen lamp (W/Kr) and deuterium lamp (D₂) as the sources.

Significant spectral changes were observed for QAN-1,5OH as the polarity of the solvent changed (Figure 16). These changes can either be classified as negative or positive solvatochromism if there is a hypsochromic (blue) or bathochromic (red) shift in the absorbance spectrum with increasing polarity of the solvent.¹⁰⁵ As a measure of solvent polarity, dipole moment was examined as a means to better understand the data. Some of the less polar solvents such as toluene and chloroform had λ_{max} values of 492 and 476 nm, respectively, while some of the more polar solvents such as acetonitrile and DMF had λ_{max} values 563 and 579.5 nm,

respectively (Figure 15 and Figure 16) In most instances, this indicates that the dye exhibits positive solvatochromism with red shifting in more polar solvents. However, there are quite a few exceptions such as isopropanol, which is low in polarity with a dipole moment of 1.66 but has a λ_{\max} of 520nm, and triethylamine with a dipole moment of 2.8 and a λ_{\max} of 495 nm. Computation studies could provide more insight into energy levels and transitions affected by these solvents.¹⁰⁶ The actual mechanism of solvatochromism in this particular dye is unknown, however it could be relative to the close proximity of the hydroxyl to the quinoline moiety (Chapter 2). This could lead to charge transfer processes that are susceptible to conformation changes within various solvents.¹⁰⁷ Additionally, there are two hydroxyls that can partake in hydrogen bonding to various extents with the solvent. All these factors contribute to the antibonding (π^*) and bonding (π) molecular orbital energy levels. The conformation of the molecule can change orbital overlap and interactions. This changes the energy difference (ΔE) between π and π^* which changes the subsequent energy absorbed resulting in a different λ_{\max} .⁴⁶ If solvent choice became a priority and this or other solvatochromatic dyes were sensor targets, this phenomenon would need to be explored more.

3.2.2 MOPS Aggregation Study

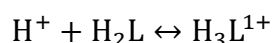
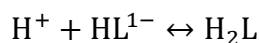
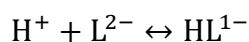
MOPS buffer has a strong interaction with Fe(II) and weak interactions with Mg(II), Mn(II), Co(II), and Ni(II), leading to aggregation and the subsequent scattering of light during the absorbance measurement. An example of this is the Ni and MOPS complexes reported by Poulson and Drever. Ni likely forms NiMOPS⁺ and more readily, Ni(OH)MOPS complexes with a log K value of 7.0.¹⁰⁸ In performing the metal response testing, it was seen that Fe(II) and Cr(III) were possibly forming aggregates with MOPS under the experimental conditions. To test this

hypothesis, Cr(III) and Fe(II) samples were prepared with PAN-7OH in a variety of buffers. The buffer concentrations used were 0.10 M and samples were placed in 1-cm PMMA cuvettes. The PAN-7OH concentrations were 30 μ M and the metal concentrations were 10 times the molar equivalents. EPPS buffer was initially used but it also showed some aggregation in forming a complex with Fe(II). For this reason, an acetate buffer was used for the Fe(II) samples while EPPS was used for Cr (III). Aggregation was seen in Fe(II) and Cr(III) testing with most of the novel azo dyes. To understand the response, PAN-7OH was tested with EPPS as the buffer. EPPS is capable of buffering near the MOPS pH range and was used for the samples at pH=7 to test for a Cr(III) response. Acetate was used to attempt to see a response at pH=4.7 for the Fe(III) as it is known to be more soluble at lower pH. This pH will leave the PAN-7OH protonated in the distal hydroxyl that is not involved in binding metals. This corrected the scattering effects and absorption was observed for Fe(II) at pH=4.7. There was no absorption difference seen with Cr(III) even when the scattering was corrected. These results are shown in Figure 17. The buffer change was successful in identifying a response to Fe(II) that was previously covered by scattering because of aggregation. It was also capable of clearing up the scattering seen in Cr(III) spectra to reveal that the dye did not respond. Additionally, phosphate and tris buffers were used at later dates for metal response testing and they removed scattering issues. Thus, if aggregation and scattering is seen for a dye/metal in MOPS, there are other options to see if there is a spectral response.

3.2.3 Free Dye pK_a Studies

To determine the pK_a values for the free dye in solution, pH titrations were performed. Collection of the spectral data while varying pH was used to determine the concentration of species in solution throughout the titration. Samples were prepared from stock dye to a concentration of

25 μM in 10 mL plastic volumetric flasks. Although the 10 mL polymethylpentene (PMP) volumetric flasks are resistant to acidic conditions, for low pH (<2), glass volumetric flasks were used as a precaution. The samples were buffered at pH values ranging from 1-13 using buffers that would not complex with metals. The buffers and corresponding pH ranges are listed in the table I of Chapter 2. The buffer components were prepared at a concentration of 0.10 M and Triton X-100 was added to a concentration of 2.0 mM as described in the Chapter 2. Typically, pH intervals of ~ 0.5 were used for "scout" titrations and ~ 0.2 - 0.3 for subsequent titrations. The flasks were not inverted until after filling to the line as this caused excessive bubble formation from the surfactant. Spectra were collected on either the Perkin Elmer or StellarNet spectrometer. For data analysis, the ReactLab Equilibria software package was used to model protonation reactions, as described below. Modeling was done based on absorbance changes as a function of the number of protonation sites present. The dye was expected to have three pK_a values corresponding to the two hydroxyl groups and the pyridyl nitrogen. Thus, the model used included three protonation steps:



Errors were calculated as described in Chapter 2. The errors are comprehensive by including all regression, experimental, and instrumental errors. They are estimates on the high end where possible to be cautious in reporting values. The biggest contribution to the error is the sample preparation and measurement because of the number of steps and intrinsic errors in the instrumentation. There is little contribution from the regression because the model is fitting well.

When isolating the sample preparation and regression components of the error propagation calculation, the regression error was typically one order of magnitude smaller than the sample preparation errors. This shows the effectiveness of the model to calculate accurate values given typical data sets. Most of the error was unavoidable such as the error in glassware tolerances, pH, and absorbance with conventional analytical equipment and instrumentation.

pH profiles for QAN-1,5OH and QAN-4OH were created by preparing dye solutions in 10 mL PMP volumetric flasks that ranged from pH 1-14 using the various buffers (0.1 M) that are listed in Table I (Chapter 2). A range of dye concentrations was used for QAN-1,5OH because at higher pH values the absorbances were higher than 1. The spectra were imported into ReactLab EQUILIBRIA for analysis using the same protonation model as shown above for PAN-7OH. Based upon the pK_a values that were obtained, the species distribution over the pH range was calculated. As before, the pK_a values of PAR were used for an initial estimate and the pK_a values of the dye were then solved iteratively.⁵³ Examination of the residuals plot and the decomposed spectra was done to identify whether satisfactory fitting had occurred. The initial estimate was also varied and the model was found to consistently reach a minimum at the same pK_a value.

The Reactlab Equilibria model was based upon $pK_w=14.17$ because the experiment was done at 20 °C. The program uses an iterative regression based upon minimizing the sum of the squares of the residuals. This regression yielded the concentration profile of each species during the titration, the decomposed spectra (molar absorptivity coefficients for absorbance data), and the regression residuals. In turn, the equilibrium constants (K) were calculated from concentration profiles. Additionally, the residuals plot was analyzed and determined to be randomly distributed with optimal (i.e., minimal) values. Finally, the decomposed spectra were examined because they should resemble the input spectra in each pH region. The output concentrations calculated by the

model were plotted as a species distribution plot over the pH range. Concentration is represented as mole fraction based on the initial dye concentration, as shown in Figure 18. The plot indicates where pK_a values occur, that is, when equimolar levels ($X=2$) for two given species are present (i.e., intersections). The pK_a values provide a useful indication of how metal binding will be impacted by pH changes. The binding pocket for metals exists between the pyridyl nitrogen, azo nitrogen proximal to the naphthol moiety, and the proximal oxygen of the naphthol. The first pK_a value of 2.702 can be assigned to the pyridyl nitrogen; the second pK_a to the distal hydroxyl on the naphthol moiety the “7OH” group; and the third pK_a to the proximal hydroxyl, as shown in Figure 18. This binding will be affected by the hydrogen ions present in solution competing with the complexation of the metal ion and ligand. The second pK_a will be eliminated when the dye is attached to the solid support as the oxygen provides the ability for covalent attachment.

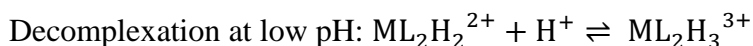
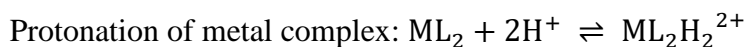
The three pK_a values for QAN-1,5OH were determined to be: 1.694, 9.240, and 11.415 for the quinoline nitrogen, para hydroxyl, and opposite hydroxyl respectively (as shown in Figure 19). A species distribution plot was created using the results and shows that the dye will have a large region in which pH should not affect the protonation state appreciably (Figure 19). As before, the middle pK_a would be eliminated with attachment to the film, thereby effectively allowing only one species (H_2L) to exist from pH 2-11. In the species distribution plot, it can be seen that HL^{1-} never reached a mole fraction of 1 as predicted by the model. This is likely because the second and third pK_a values are so close together, thereby broadening the pH region below these values. The decomposed spectra show that the protonated forms of the dye have a much larger molar absorptivity coefficient. Additionally, the experiment was done in two sets and the data were combined for the modeling. The sets spanned the pH values of ~1-5 and ~5-13 on two separate

days as there was error in preparation of some samples. This likely caused increased error in buffer preparation, calibration, etc. over two days rather than in one.

Using the ReactLab modeling, the spectral data for QAN-4OH was used to calculate pK_a values of 1.694, 9.240, and 11.415. These values were assigned to the quinoline nitrogen, proximal hydroxyl, and distal hydroxyl, respectively (as shown in Figure 20). The first two pK_a values were close together and this caused the H_2L mole fraction to never reach 1 in the model. Additionally, the decomposed spectra resembled each other which was probably the result of overfitting in the model. Overfitting occurs when the model begins to describe the random error and noise within the data set. This causes instability and can lead to poor fitting of subsequent data.

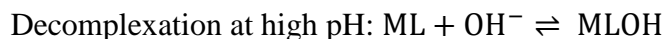
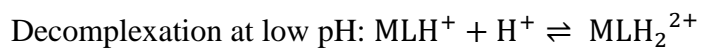
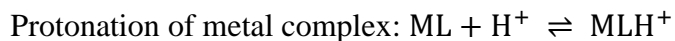
3.2.4 Determination of Metal Complex pK_a Values

For the pH titrations of the metal complexes, samples were prepared from stock dye solutions as described above for the free dye pK_a but with respective metal included. The model chosen for most metal complexes (except Pb) included decomplexation at low pH. Metal complex protonation and decomplexation were modeled in the following manner.



Where $ML_2H_2^{2+}$ is the di-protonated metal complex and $ML_2H_3^{3+}$ represents decomplexation and would be more accurately written as $M^+ + 2H_3L^+$. However, the modeling software only allows for one product to be written. These species are shown in Figure 22. The model chosen

for Pb included an additional step for the decomplexation at high pH. Additionally, it was modeled as a 1:1 complex.



Where MLOH would be more accurately written as MOH + L if it was possible to have two products in the modeling software. The spectra observed at low pH values looked similar, if not identical, to the free dye at low pH, thus decomplexation was modeled at low pH values (as shown in Figure 23). The other step included in the model represents a protonation of the metal ligand complex at the hydroxyl that is away from the binding site. This “pK_a” represents two protonations because the ligand forms a 1:2 complex with the metal. The microconstants (i.e., specific protonation sites) for these protonations could not be identified spectrophotometrically. Originally, a third step was included in all modeling. The decomplexation at high pH is thought to be caused by metal hydroxide formation. Metal hydroxides are known to form at high pH as shown in a pourbaix diagram of Pb (Figure 24) and this competes with the metal binding to the ligand. With most of the metals, there was spectral evidence that this was occurring. The spectrum of the metal complex would start to shift and mimic that of the free dye at high pH (i.e., completely deprotonated). Unfortunately, for all metals except Pb, there was not enough of a shift at the pH values tested to model this decomplexation process (Figure 23). Attempts at modeling this step resulted in poor convergence and large error. The same validation steps as described above for the

free dye studies were used to see if the model was a good fit. The species distribution plots are shown in Figure 25. The free dye and metal complex pH studies are summarized in Table IV.

The computed pK_a values for PAN-7OH can give some insight on binding affinity. The lower the first pK_a , the harder it is to displace the metal in the binding pocket with a proton. According to the order of pK_{a1} , the binding affinity of PAN-7OH should be increasing in the order of Cu, Co, Pb, Ni, Zn, and Cd. The pK_{a1} value of the Cd complex is quite high in comparison to the others. It is possible that this is an artifact of overfitting or a poor model. “Overfitting” occurs because the spectral characteristics of the Cd complexes do not differ much and the minimum that the model reaches might be inaccurate. Attempts were made at adjusting the starting guess to a lower value, but the same minimum was reached. The pK_{a2} values fall within similar areas which means that the hydroxyl that is not involved in binding is not affected much by the presence of the metal. The third pK_a was only modeled with Pb because it is believed to have been too high to accurately model in the other cases. As mentioned before, metal hydroxides form especially well at high pH values. This “third pK_a ” is not similar to the first two pK_a values because it represents the metal hydroxide rather than the free dye. The pK_a values for the free dye are comparable to previously potentiometric studies of PAN and PAR. PAN has reported pK_a values of <2 and 12.3, and PAR has been reported to have pK_a values of 2.3, 6.9, and 12.4.⁵³

3.2.5 Determination of Binding Ratios

To determine binding ratios near pH 7, titrations were performed on several dyes. These titrations were done in PMMA cuvettes with absorbance monitored from 350-750 nm. For example, for PAN-7OH, a sample was prepared in 0.10 M MOPS at pH 7.2. Steps of 0.1 [M]:[L] were taken to determine where there were no more significant changes in absorbance. Cu(II), for

example, was added in 9.53 μL aliquots to change the mole ratio by 0.1 for each step and the absorbance at λ_{max} was plotted vs. mole fraction (Figure 21).

The titration of PAN-7OH with Zn was initially used to approximate a binding ratio for modeling purposes that was representative. A dye concentration of 20 μM was found to produce a significant (>0.1) absorbance value. The λ_{max} of the metal ligand complex was observed to be 554 nm and was plotted against mole fraction of Zn. If the metal and ligand bind in a 1:2 ratio, the absorbance should effectively level off around a Zn mole fraction of 0.5 because the λ_{max} of the free dye will decrease as the metal-ligand (ML_2) complex forms. The maximum should occur when the Zn mole fraction is 0.5 because all binding sites should be occupied. As expected, a corresponding shift in the absorbance was seen when Zn was titrated because the metal complex formed has a different absorbance profile than the free dye. A leveling off slightly before the mole fraction of 0.5 was observed, so the titrations with the other metals were performed for comparison. Mixed results were found, with some leveling off at a mole fraction of 0.5 while others at different values. There are several possible reasons for explaining this unexpected behavior. First, the kinetics of binding are slow for some metals, in particular for Ni. When titrating, it was observed that the complex formation and subsequent color change was slow. Because MOPS buffer has weak interactions with Ni and several other metals, the slow rate of metal-dye complex formation that was observed was not unexpected. To try to overcome the sluggish kinetics, a small stir bar was added to the cuvette but the complexation rate was unchanged. Another issue that was identified was that the baseline was not flat (i.e., because of scattering). The addition of a surfactant helped minimize the baseline offset problem, however, it persisted and could only be corrected by subtracting a reference absorbance at 800 nm from all data points. Finally, and most problematically, was the observation that some of the metal could be forming a 1:1 complex rather

than a 1:2 complex. It is possible that at these low concentrations both the 1:1 and 1:2 complex are being formed. This was the case for the Pb complex, which leveled off slightly beyond a mole fraction of 1. Overall, it was assumed that the binding ratio for the affinity studies (described below) should be 1:2 for all metals except for Pb, which was 1:1. This assumption gave the best results when modeling the binding ratios. If other stoichiometric ratios were present, they would contribute to an error in these studies.

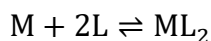
3.2.6 Study of Binding Affinities

Binding affinity was studied for PAN-7OH with Cd, Co, Cu, Ni, Pb, and Zn at pH 7.0 using 10-cm quartz cuvettes. The MOPS buffer was treated with Chelex to remove trace metals and a stir bar was placed inside the cuvette for efficient mixing. Metal was titrated into the dye solution and spectra were collected after each metal addition and mixing took place. The stir bar and cuvette were positioned identically for each measurement. The amount of metal pipetted in each step depended on the binding affinity and in some cases, several experiments had to be performed to identify the optimal amount. The spectral data collected were analyzed with ReactLab Equilibria to determine binding affinities.

Baseline issues were again observed in many instances and corrected for by subtracting the reference signal at 800 nm. The observations from the binding ratio studies described above were used to determine an appropriate initial dye concentration, with an initial concentration of 1 μM for Zn. Large titration steps were made to determine the overall shape of the binding curve, with the expectation that a hyperbolic curve would be observed if the initial dye concentration was near the K_D value. The model predicted the binding affinity in the form of a log K_F value, and K_D was calculated as:

$$K_D = \frac{1}{10^{\log K_F}}$$

For Zn, an initial 1:2 binding model was created to estimate the K_D at approximately 200 nM. This data was modeled and the K_D was found to be higher than the initial dye concentration. The experiment was repeated with the initial dye concentration set to 508 nM to make sure that an accurate binding affinity was obtained, with the initial dye concentration closer to the K_D . Zn was titrated in small aliquots until significant changes (<0.05) in the spectrum had stopped and then larger titration steps were made to ensure complete binding. The baseline of most spectra collected was offset toward negative values, and therefore had to be corrected by subtracting the minimum absorbance from 450-750 nm from all data points. The following step was used for the application of the Reactlab Equilibria software:



At high metal concentrations (above 500-fold molar excess for Zn) there appeared to be a 1:1 complex forming because spectral changes indicated the disappearance of the 1:2 complex and the appearance of a new species. Attempts were made at modeling a 1:1 complex forming at high metal concentrations, but this always resulted in a poor regression fit. It was difficult to model the fact that 1:1 binding does not start to become apparent until high metal concentrations. For 1:1 and 1:2 complex K_D values that differ greatly by many orders of magnitude, it is impractical to measure them with the same initial dye concentration. Because most practical applications will not have such high metal concentrations, the 1:1 step was ignored, and the model was simply built with 1:2 binding as its basis. The overall model fit after background subtraction was satisfactory with a

regression error in $\log K_F$ of < 0.003 . The decomposed spectra are shown in Figure 26, as well as the binding curve which exhibited good hyperbolicity because the $[L]_0$ was on the order of the K_D .

The determination of the binding affinity of PAN-7OH with Ni, Cd, Co, and Pb was completed in a similar manner as described above, and the data treatment was the same. The initial dye concentration was set to ~ 500 nM and the pH was ~ 7.0 for all experiments. Care was again taken to ensure thorough mixing, with longer mixing times used for the Ni titrations because of the slower kinetics. When trying to obtain the PAN-7OH binding affinity for Cd, it was found that the K_D was much higher (~ 5 mM) from a scout titration done at an initial dye concentration of 507 nM. This curve is extremely sharp and the K_D calculated is inaccurate because the $[L]_0 \ll K_D$. The $[L]_0$ was set at 5.07 mM and the titration was repeated. $\log K_F$ was calculated and converted to K_D for each metal and the fitted results are shown in the binding curves in Figure 27-Figure 31.

Special care was taken when analyzing the Cd titration data. The Cd complex was shown to have a pK_a near 7. The pK_a data from earlier experiments was used to make an adjustment to the concentration values that were used in the model. The initial dye concentration used was 507 nM; however, this does not account for the fact that some of the dye would be protonated and unable to bind the metal. Attempts were made at including this protonation step into the model itself, but this caused convergence issues. Thus, the pH used for this experiment, 7.093, was used to extract a value for how much dye was protonated using the pK_a data. Without extensively fitting the data to a function, the best estimation was to fit a b-spline and select the closest pH value. At $pH=7.096$ there was 32% of the dye was protonated. This meant that 68% of the dye was available for binding and therefore, 0.68 was multiplied by all $[L]_0$ values that were included in the model. The Pb titration was modeled as a 1:1 complex given the binding ratio data obtained in previous experiments. Several scout titrations showed that the Pb complex had a slightly higher K_D and

aggregated, which caused issues with scattering. The scattering was overcome by titrating the metal into the blank as well as the sample, which minimized the micellar scattering that occurs when the metal and surfactant interact. Subsequently, the initial dye concentration was set at 1.507 μM because the scout titrations showed a higher K_D .

The binding affinities for the metals tested follow the trend with increasing affinity from $\text{Cu} < \text{Co} < \text{Zn} < \text{Ni} < \text{Cd} < \text{Pb}$. The likely explanation for this order is relative to the size of the metal ions. As shown in Figure 32 and Table V, the larger Pb^{2+} and Cd^{2+} have much higher (order of magnitude) K_D values. The K_D' values are the square root of the K_D values for the metals that bind in a 1:2 fashion which is a more realistic comparison to the 1:1 coordination of Pb. The binding affinities toward certain metals might be improved if the binding pocket were made larger. A larger binding pocket, such as moving the hydroxyl or changing the ring structures, might have more selectivity for larger ions such as Pb^{2+} and Cd^{2+} . One must be careful in this approach as making too large of a binding pocket could lead to very weak binding and an ineffective sensor.

3.2.7 Development of a PLS Model

To evaluate the performance of the chemosensors in monitoring multiple metals simultaneously in near-real time at low levels in a process environment, it was necessary to develop a modeling method. As mentioned in Chapter 1, Partial least squares (PLS) was chosen because it is a “soft” modeling technique for building predictive models. PLS is very robust and capable of handling large datasets quite readily with its reduction in dimensionality. By collecting data on metal responses from various dyes, a model could therefore be built to predict metal concentrations in process samples. PLS requires a set of training data to quantify analytes, thus a model was constructed with a set of known spectral responses to the metal:dye mixtures (“pseudo-unknown

samples”), and then the entire spectral data set was used as the input to the model. PAR and QAR were studied together in a model capable of quantifying four metals (Cu, Ni, Zn, Pb) in mixtures. The total metal concentration was $\leq 10 \mu\text{M}$ and dye concentrations were $\leq 20 \mu\text{M}$ (0.10 M MOPS at pH 7.0 and 500 μM Triton X-100).

In developing the PLS model, a variable importance plot (VIP) was generated as shown in Figure 33. The VIP represents the contribution of each spectral value in the predictive model. Note that 0.8 is set as a threshold in which the corresponding spectral values do not contribute strongly to the predictive model.¹⁰⁹ This plot provides insight into the relative importance of spectral regions within the entire spectral data set. Another PLS model was constructed with data that was cropped using the VIP criterion, and a small increase in the prediction errors was observed. This was expected because the VIP is a measure of the most pertinent data for modeling. By cutting out extraneous information, the model should have become more accurate and stable. This was not observed which indicates that the model was already capable of distinguishing which regions were important. However, issues with baseline drift were not encountered in model development because the wavelength used for background correction (800 nm) showed very low importance.

The VIP is a more practical interpretation for spectral data than the score and loading values because it provides insight into the most useful spectral data in modeling.¹¹⁰ Trends are present when comparing the spectra in Figure 62 and the VIP in Figure 33. The VIP plot has peaks near the λ_{max} values of the metal complexes. This was expected as these regions are the most important in modeling. Also, the VIP values were high for QAR in spectral regions where PAR was diminished and vice versa. This could be relative to how well QAR compliments PAR, but this observation may have been a coincidence because PLS does not form a causal relationship between latent variables. Rather it assumes that latent variables are related to the same underlying causes.

This comparison connected the observed spectra to the predictive PLS model, provided a basis for spectral selectivity with a predictive model, and conceptualized the abstract latent variables in the model.

The PLS model was validated using 15 pseudo-unknown samples (Figure 34 and Table VI), and the prediction repeatability of the model was examined using 19 replicate measurements where the samples contained approximately the same concentration of each metal (Figure 35 Table VII). The prediction errors were modest, and the greatest values were 0.24 μM (15 ppb) for Cu, 0.50 μM (33 ppb) for Ni, 0.44 μM (27 ppb) for Zn, and 0.22 μM (46 ppb) for Pb. Also, the total prediction error was below 0.9 μM in all 15 cases. Examining the plots in Figure 34, the predictions were slightly overestimated for Cu and Pb, overestimated for Ni, and underestimated for Zn. Also, examining the values in Figure 34, the prediction errors were larger for Ni and Zn, relative to the prediction errors for Cu and Pb. The spectral profiles of the complexes of both PAR and QAR with Ni and Zn were quite similar at pH 7.0 while the complexes Cu and Pb had distinct profiles (see Figure 62 in appendix 1). This suggested that a different sensor that exhibits a unique response for Ni and Zn would improve the prediction accuracy for these two metal ions. In addition to the VIP analysis, the mean prediction errors for replicate measurements were determined. For the four metals studied, the following values were obtained: 0.19 μM (12 ppb) for Cu, 0.36 μM (21 ppb) for Ni, 0.26 μM (17 ppb) for Zn, and is 0.14 μM (29 ppb) for Pb, and the corresponding standard deviations were below 10 ppb. Figure 35 is a plot of the distribution of the absolute prediction errors for the replicate measurements and shows underestimated predictions for Cu and Ni and overestimated predictions for Pb and Zn. Also, the mean prediction error for Ni is approximately the same as the mean prediction error for Zn. Moreover, these sets both contain an outlier for the same sample. As mentioned previously, the spectra of both PAR and QAR for Ni and Zn are

similar at pH 7.0, and therefore do not have a high spectral selectivity for these two analytes, resulting in the gross error for the outlier sample and elevated prediction errors for Ni and Zn. In addition, the distribution widths are similar for Cu, Ni, and Pb while the distribution for Pb is relatively narrow. QAR does not bind appreciably to Pb and therefore does not generate an appreciable spectral response. This feature improves the prediction ability of the model for Pb because QAR can identify whether it is present. If simply using PAR, it is not possible to know if the signal is from lead or another metal.

The results of the application of the PLS model demonstrate that two azo-based absorbance sensors can be used to simultaneously to quantify four metal ions in an aqueous mixture at sub-ppm levels. Even though both sensors bind to multiple metals, the distinct spectral responses of the sensors to each metal allows for discrimination of metals in a mixture by the PLS model, and greater “spectral selectivity” yields more accurate and reliable predictions from the PLS model. Furthermore, the response of two sensors, one that responds to an analyte and one that does not, can be combined to yield an accurate and precise prediction even though neither sensor is specific to the given analyte. Potentially, this approach can be expanded to include additional sensors with varying binding properties and spectral selectivities, and a sensor array could quantify metal ions in a comparable manner to a set of specific sensors. Also, other measurements could be included in a predictive model if they have a significant effect on the absorbance spectrum, such as pH, ionic strength, and temperature. However, the main drawback of course is that the amount of calibration data increases dramatically as predictive models become more complex.

Additionally, the construction of the model was explored by using the PAR data. The pseudo-unknowns that were prepared fell into four categories: Unitary, Binary, Ternary, and Tertiary. To determine the effect of the mixture type, four different PLS models were built. The

first included only unitary samples, the second was made from unitary and binary mixtures, the third from unitary, binary, and ternary, and the last was made from all the mixed samples. The average error in the prediction was then used to compare the accuracy of the models (

Figure 36). Surprisingly, the binary model, which contained unitary and binary mixtures, had a huge error in comparison to the others. There appeared to be correlation introduced that was based on the experimental procedure. That is, the samples were prepared in a sequential pattern where metal was titrated in series to reduce the number of samples that needed to be prepared. Consequently, this meant that many samples were integer increments in the metal concentrations. Any correlation such as this in PLS cripples the modeling ability because it leads to overfitting. A more random distribution of concentration values would avoid this issue and the model would have more stability. The increase in modeling ability when the ternary mixtures were added is likely because to the increase in the number of samples because the model is given more detailed information on metal interactions with the dye. Surprisingly, the model worked exceptionally well with simply the single metal samples. This either means that the metals did not interfere with one another significantly or the model is simply powerful enough to determine metal concentrations from individual responses. The black bars in the graph represent all the spectral data being included while the red bars represent the results when data below the variable importance of 0.8 was omitted. In most cases this was the baseline data and overall, trimming this data did not help or hinder the model, thus showing the ability of the model to identify the most important regions of the spectra and ignore any baseline issues.

3.2.8 Dye Longevity Study

To determine the stability of the dyes over time, a longevity study was performed by placing capped cuvettes containing the dye solutions in a humid environment for several weeks. The dye concentrations were chosen based on their ϵ values so that the absorbance was ~ 0.5 units. Although the cuvettes were placed in a glass container that was humidified, they had to be periodically weighed to correct for changes in volume because of evaporation.

The study done to determine longevity showed that the molar absorptivity coefficient for some dyes dropped off quickly within 3 weeks while some were stable (Figure 37). In some cases, the normalized ϵ values increased from one week to the next. This was typically because of scattering, which was simple to identify in the spectra because of a baseline offset at shorter wavelengths. Thus, the surfactant included was not able to overcome the tendency for some dyes to aggregate. Careful mixing was attempted but some dye would get stuck between the cap and the wall of the cuvette. Future iterations of this experiment could include stir bars that would be permanently placed in each cuvette so that mixing could take place without loss of dye. However, the dye can sometimes aggregate on the stir bar so artifacts would still appear. It would also be important to cap the cuvettes better. A rubber septum might be a better option than the plastic caps used. This would allow for water to easily be added by syringe without removing the cap and risking the loss of dye.

3.3 Flow Experiments

There were two different flow systems used in the development of the optical sensing platform. The conventional system used large tubing and high flow rates while the SIA method

used small tubing and low flow rates as described in Chapter 2. Some important aspects of each design were tested including the response and repeatability, as well as the metal concentration, flow rate, and pH effects. The films tested mainly consisted of PAR films because of the accessibility and this dye being a promising candidate for process applications of the sensor. The metal used was typically Zn because the demand for a Zn sensor, but other metals were also tested as well. For either flow-based instrument design, the chemosensors must be stable for long periods of time. This means that they must be securely attached to a solid support and not wash away. Therefore, the sensors were incorporated into hydrogel polymers and covalently attached to glass to be inserted into a flow cell, as described below.

3.3.1 Conventional Flow Experiments

The conventional system (described in detail in Chapter 2) had a large flow cell volume and operated at high flow rates. This system was tested with a flow cell design that included a slot for the cartridge containing the dye that was attached to glass. The flow was parallel to the dye and the optics were perpendicular to the flow. The system was tested in several different configurations as described in Chapter 2; however, there was negligible difference in performance observed among the designs. The studies described were aimed at determining the capability of this system as an optical sensing platform.

3.3.1.1 Initial Response Testing

Testing of the conventional system was first done by studying the response rate of a PAR film to Zn at three different metal concentrations (10, 20, and 30 ppm). Plotting the

absorbances at λ_{\max} for the PAR film between 10-30 ppm, gives a good binding rate comparison between different metal concentrations.

It can be seen in Figure 38 that the rate of response increased as the concentration increased. The reason for the negative absorbance is that the free dye peak was disappearing. The spectrum should have been increasing where the metal complex exists. This was not the case for these data sets and there are several possible reasons for this. The most likely is that the buffer concentration of 0.010 M was being overloaded by the 2% (v/v) HCl in the Zn AAS standard. The buffer capacity was 0.05, so the added HCl would have overwhelmed it. The lower pH would have affected the observed spectrum because the baseline was done on buffered solution at \sim pH 7.0. This could contribute to the metal complex peak being masked by the spectral changes because of pH. Additionally, the minimum absorbance value reached in each case differs. This can also be explained as a pH effect because the higher the metal concentration, the more of the acidic AA standard was used. In subsequent experiments, the buffer concentration was increased to 0.10 M to ensure that a sufficient buffer capacity was obtained. Nevertheless, as of course expected, this set of experiments showed that the rate of the response is, in fact, dependent on the metal concentration, as expected.

To determine if the buffer concentration was adequate, a 5 ppm Zn solution was prepared at pH 7.4 and buffered by 0.10 M MOPS and introduced to a PAR film. The absorbance at λ_{\max} was plotted vs the time in Figure 39 to explore the rate of complexation. The overall response is also shown, and negative and positive peaks are seen corresponding to the free dye and metal complex, respectively. This shows that the previous buffer concentration was not adequate and that it was being overloaded by the acidic AA standard.

3.2.1.2 Repeatability Studies

Several repeatability studies were done over the course of testing the conventional system. Multiple trials of the same metal concentration were performed. These studies were important in providing a look at the precision of the device and the ability to produce results consistently. The relative standard deviation (RSD) was calculated as an analytical figure of merit for each test. The goal was to have an RSD of less than 5% when testing multiple films with several different metals.

The repeatability of an OAN-4-DPA-SA (hex) film was tested by comparing six consecutive runs of 1 ppm Zn. The 3-pump design showed good repeatability as shown in Figure 40 where the response is clearly seen when the metal is binding. There is a peak increasing in intensity near 553 nm which is in the general region of Zn peaks for most zo dyes studied in this work. The acid wash is also shown as the peak becomes negative and levels off, indicating that all the metal is removed between experiments. The small differences in the 6 runs can be attributed to fluctuations between experiments. The average RSD for all data points was 2.3% which is quite acceptable in this application.

The repeatability of a cationic PAR film can be seen in three different experiments. First, by comparing five consecutive runs of ~11 ppm Zn, then comparing three consecutive runs of 1 ppm Ni and finally, two runs of 100 ppb Zn (Figure 41, Figure 42, and Figure 43). The absorbance at 514 nm was plotted against time for each run because Ni and Zn have the same λ_{\max} values. These concentrations and metals were chosen to observe how well the film performed in different situations. The concentrations yielded absorbance changes in a reasonable time period. For the 11 ppm runs, the data was concatenated for all runs and not overlaid to provide a different view of the results. The average slope of these lines was 0.0178 absorbance units min^{-1} which was faster than the OAN film likely because of higher loading. The return to an absorbance of zero between

trials is because the acid washing followed by equilibration at neutral pH. The RSD for these five runs was 17.2%. This value is high because the method that was used to collect data. The method collected a spectrum every minute; however, the time needed to store the data varied. Therefore, the time stamps over several runs did not overlap. The three Ni trials had an average RSD of 1.5% for all data points and the overlaid runs have good precision between consecutive trials with an average RSD for all data points of 1.54%. This was lower than the trials done with the OAN film which is likely because to the loading and concentration of metal used. The signal approached 0.4 absorbance in the Zn runs whereas in the OAN repeatability studies, the signal was only near 0.16 at the maximum. The fact that the λ_{max} is the same for both metals would be a consideration to make when apply any sort of model to the binding because it would be difficult to distinguish between the two metals.

3.3.1.3 Flow Rate studies

The effect of flow rate on the binding rate of the metal ions to the chemosensor dyes was studied in a flowing stream and as well as under quiescent ("stopped-flow") conditions. In this way, the effect of convection could be studied relative to mass transport solely by diffusion. The rate of response is expected to increase as the higher flow rates increase because convection would facilitate transport to the binding sites on the sensor. It is expected that under stopped-flow conditions, the response will change at a given rate before slowly levelling off because the depletion of analyte within the flow cell.

A cationic PAR film was tested with Zn standards at pH 7.0 at two different flow rates to better understand the extent of diffusion, and the flow was stopped at approximately the halfway

point of the last experiment. The volume of metal dispensed remained constant and the absorbance at 516 nm was plotted vs. time for these runs (Figure 44). The response is larger for the faster flow rate, reaching an absorbance of nearly 0.20 rather than 0.15. The mean slope of the slower and fast rate runs was 9.18×10^{-3} and 9.09×10^{-3} absorbance units min^{-1} respectively showing that flow rate does increase the response rate. Figure 45 shows the effect of stopping the flow for a longer period. The flow was stopped at the point marked on the dotted line. In comparison to the continuous flow experiment (solid line), the film appears to be accumulating more Zn but the absorbance starts to level off. Diffusion of the analyte through the film depletes the concentration in solution. Initially, the binding will proceed normally but after some of the Zn is bound to the dye, there will be a slower rate until all Zn in the flow cell is used up or an equilibrium is reached, and no net binding occurs. At that time, there should be no spectral changes occurring. A few longer runs were done to reach saturation and observe this state. The PAR film was used in a 100 ppb Zn experiment. The 100 ppb Zn was prepared at $\text{pH} \approx 7$ as previously described. The results are shown in Figure 46 and it can be seen that saturation was not reached over 250 min and the film still had a linear response to the metal solution. A run with Cu was performed in Figure 47. The λ_{max} was slightly blue shifted from the response of Zn. The response also seemed slightly more curvilinear. In real-world applications, there may need to be some intervention such as acid washing to clean the film before this amount of time is reached. For many of the spectral responses, there was an artifact that exist at the beginning. This is likely because some refractive index change or pressure differential.

3.3.2 SIA Experiments

SIA experiments were performed to test the dependence of the response on factors such as flow rate, analyte concentration, pH, and ionic strength. As mentioned in Chapter 1, the microscale SIA system is an excellent platform for high-throughput testing of the films. The films are expected to respond faster with increased flow rates and analyte concentrations as both facilitate more efficient diffusion. The response is expected to be best at neutral pH values where there is less competition for protonation of the binding pocket (low pH) and metal hydroxide formation (high pH). Higher ionic strength is expected to improve transport rates because it helps diffusion of charged metal ions into and out of the film. Additionally, the baseline effects were studied to see if baselining in acid was sufficient. The acidic baseline is expected to slow the response as the film must equilibrate to neutral pH before binding can take place.

3.3.2.1 Flow Cell Design

The flow cell for SIA (Figure 48) is a standard Z-type design with a depression (“well”) to hold the glass slide that contained the covalently attached films. Because the “well” (Figure 48) was designed only to the depth of the glass slide (1 mm), it had to be modified to better accommodate the film.. To overcome this, the flow cell was re-machined to increase the depth of the well to 3.08 mm and several types of gasket materials were studied, including washers made of silicone, polyethylene (PE), and Teflon. A silicon adhesive was also used to prevent leaking once the washer was in place. PE tape (76 μm thick) proved to be the best material because, in addition to its

function as a gasket, it kept the glass slide in place and blocked the dead volume that is found between the edges of the glass slide and the well.

3.3.2.2 Method Development

An example of the method development that was done before each SIA experiment is shown in Figure 49 and Figure 50 for a QAR film. The amount of acid needed to completely rinse the metal out of the flow cell was determined. As shown in Figure 49, a negative peak appeared when acid entered the flow cell. In Figure 50, time zero represents the baseline that is taken in the carrier solution (0.10 M MOPS pH \approx 7) and the introduction of the solution at 30 $\mu\text{L s}^{-1}$. The initial amount was 2000 μL and this was reduced to 1000 μL for the refined experiment after seeing how much acid was needed to stabilize the signal at the maximum negative value. The deep negative peak signifies the disappearance of the deprotonated dye species and the removal of the metal. The return to baseline as shown in Figure 51.

3.3.2.3 Repeatability Studies

The repeatability of the SIA method was tested, as shown in Figure 52 where two 3.3 ppm runs with the anionic PAR are depicted. Nearly identical responses were observed, and the response is linear and then levels off as saturation occurs at an absorbance value of 0.3 for these runs. The average RSD for all data points was 2.07% after the absolute value was taken because negative absorbance values caused by noise at the beginning of the run, i.e., before metal started

to accumulate. This is an exceptional that would be more than acceptable for repeatability in a prototype process monitoring device.

3.3.2.4 Influence of Metal Concentration

The impact of the metal concentration can be seen throughout several different experiments. The initial experiments were done to show the general trend of flow rate increasing with metal concentration. Further investigation was done to determine the exact effect in later experiments. Figure 53 shows the comparison between 3.3, 6.6, and 20 ppm Zn trials. The initial rate increases with increases in concentration while the saturation levels is essentially the same. To test this further and compare the initial rates to the metal concentrations, a test with five different Zn concentrations showed that the response change is significant over the range of 1-100 μM . The three higher concentrations reached saturation before the end of the experiment while the lower concentrations had not reached the 50% level (Figure 54). The initial rates of the 1-100 μM trials were compared in Figure 55 and a discontinuity was observed that was likely because the low signals and somewhat curvilinear responses. The overall trend was that the rate increased with the concentration of the metal, i.e., a gradient in the analyte concentration was established. The gradient starts to be depleted as the sensor sites become occupied and the film eventually reaches a saturation level in which the metal binding ceases.

The repeatability of the response of new films over the concentration range of 1-100 μM (65 ppb to 6.5 ppm) in 0.1M MOPS buffer at pH 7.0 was examined. After rinsing the film with ~ 3 mL of 0.10 M HCl at a flow rate of $15 \mu\text{L s}^{-1}$ and then buffering to obtain a stable baseline, the analyte zone was introduced at a flow rate of $12 \mu\text{L s}^{-1}$ and spectra were collected every at 1 s intervals.

Replicate measurements were plotted, and the initial rate of change was determined (Figure 56). Errors bars were calculated as the 95% confidence interval (corrected by Student's t-test). This film was mixed ionic with anionic sulfobenzamide and cationic amine moieties, and showed linear behavior with higher concentrations reaching saturation within the experiment window. The rate is linearly dependent upon the concentration when it is below 3 ppm but deviates at higher concentrations. The slope for samples below 3 ppm was 4.31 absorbance units s^{-1} ppm $^{-1}$ with R^2 of 0.97. (including higher concentrations decreased the R^2 by 0.03). Thus, the "mixed mode" film would be useful at lower concentrations but analysis at higher concentrations would be problematic. Response testing was later repeated using other types of films to see if a broader range could be obtained.

3.3.2.5 Baseline Studies: Acidic vs. Neutral

During studies of the chemosensor films, the baseline response was obtained by using buffer after the acid-washing step so that the film was in the proper pH state for metal binding. The metal would cause an absorbance changes to occur as the it complexed with the dye. In the industrial setting, there may be practical advantages to establishing the baseline only with acid instead of following that treatment with buffer in that one can save time and avoid the cost of buffer reagents. For this reason, acid-washing by itself was studied to determine how effectively the baseline could be established.

Figure 57 shows that when compared to the data that was obtained when baselined on buffer, the response followed a similar trend but the initial rate values were smaller in all cases. This is likely because a "lag" time where the film must equilibrate to a higher pH value. At low

pH, the film is protonated at the pyridyl nitrogen in the binding pocket. This prevents the metal from binding. As the buffered metal solution enters the flow cell and encounters the film, the azo nitrogen is deprotonated, and the metal is then capable of binding. In other experiments, with the buffer as the baseline, the film is already in this deprotonated state ready for binding. For this reason, it may be better to baseline on buffer as sensitivity is lost when using an acidic baseline.

3.2.2.6 pH Effect on Binding

The pH profile for each dye was studied using buffered Zn solutions (35 μM) at pH values from 4-11 (n=4). The effect of pH on the response was examined to see the optimal pH region for using the sensor. It was expected that the rate would vary because the pH affects the protonation state of the binding pocket. At lower pH values, the pyridyl nitrogen is protonated and unable to participate in binding. At higher pH values, there is a tendency for metal hydroxides to form and there is a lower concentration of metal ions. The best response was seen from pH 6-8 (Figure 58).

3.2.2.7 Effect of Ionic Strength

An anionic PAR film was used to study the effect of ionic strength on the binding rate. Using NaCl, ionic strengths ranging from 100-500 mM were examined. The slope of the response was analyzed to determine if there was significant change because ionic strength. Figure 59 shows that the ionic strength does not affect binding rate significantly. The error bars are large because

to small absorbance caused by poor dye loading on the films leading to a low signal-to-noise ratio. These errors account for the deviations in the observed rates; however, the change is relatively small when considering the wide range of ionic strength tested.

3.2.2.7 Response Rate and Metal Concentration

Additional testing was done with varying the metal (Zn) concentrations from 50 to 6540 ppb with a 32% anionic PAR film at pH 7.0. These runs were done at a flow rate of $12 \mu\text{L s}^{-1}$ and one of the 50 ppb runs was also done at $6 \mu\text{L s}^{-1}$. The initial rates were taken by finding the slope of the response curve.

The response rate was found by taking the initial slope of the response curves and changes significantly with metal concentration as shown in Figure 60. The slower 50 ppb run that was not included in the linear fit of the response rate change and showed a slower rate as expected. The response rate appears to change in a linear fashion with respect to Zn concentration with a R^2 of 0.996 over the entire concentration range tested. This linear response was much better than the previous film mentioned in the repeatability section. This is likely because the loading and overall film synthesis as improved methods were used for a more stable and robust film.

| Dye / λ_{max} (nm) | Al ³⁺ | Cd ²⁺ | Ca ²⁺ | Cr ³⁺ | Co ²⁺ | Cu ²⁺ | Fe ³⁺ | Pb ²⁺ |
|-----------------------------|------------------|------------------|------------------|------------------|------------------|------------------|------------------|------------------|
| PAN-7OH / 460 | NR | 519 nm/565 nm | NR | 454 nm (S) | 530 nm | 536 nm | 464 nm (S) | 515 nm |
| PAN-4OH / 424 | NR | NR | NR | NR | 481 nm | 476 nm | 419 nm (S) | NR |
| PAN-1,5OH / 480 | 365 nm | 568 nm | NR | NR | 636 nm | 602 nm | 600 nm | 585 nm |
| DAR / 433 | 335 nm | 305 nm/410 nm | 310 nm/417 nm | 332 nm/416 nm | 353 nm (S) | 344 nm (S) | S | 301 nm/411 nm |
| QAN-1,5OH / 532 | NR | NR | NR | 545 nm | NR | 547 nm | S | 534 nm (S) |
| QAN-1A / 500 | NR | NR | NR | 498 nm (S) | 582 nm | 533 nm | 471 nm (S) | NR |
| QAN-4OH / 460 | NR | NR | NR | 456 nm (S) | 568 nm | 526 nm | S | 450 nm |
| QAN-7OH / 482 | NR | NR | NR | 473 nm (S) | NR | 485 nm | S | NR |
| PAR / 450 | NR | 497 nm | NR | S | 509 nm | 509 nm | 491 nm/530 nm | 521 nm |
| QAR / 413 | 468 nm | 453 nm | NR | NR | 525 nm | 492 nm | S | 453 nm |
| DAN-4OH / 454 | NR | 491 nm | NR | NR | 499 nm | 492 nm | NR | 491 nm |
| TMH-3-107C / 457 | NR | 460 nm | NR | NR | 504 nm | 491 nm | NR (S) | 466 nm |
| TMH-3-114C / 454 | NR | NR | NR | NR (S) | NR | 482 nm | NR (S) | 463 nm |
| TMH-3-109B / 462 | 464 nm | 457 nm | 479 nm | 471 nm | 477 nm | 493 nm | S | 446 nm |
| TMH-3-111c / 457 | NR | 461 nm | NR | NR | 491 nm | 489 nm | NR (S) | 466 nm |
| OAN-4OH-5A-DPA / 447 | NR | 491 nm | NR | NR | 492 nm | 492 nm | NR | NR (S) |
| OAN-4-5A-DPA / 481 | 481 nm | 560 nm | NR | 480 nm | 555 nm | 558 nm | 479 nm | NR (S) |
| OAN-2-5A-DPA / 486 | NR | 527 nm | NR | NR | 566 nm | 530 nm | NR (S) | 530 nm |
| Dye / λ_{max} in nm | Mg ²⁺ | Mn ²⁺ | Hg ²⁺ | Ni ²⁺ | K ¹⁺ | Na ¹⁺ | Sn ²⁺ | Zn ²⁺ |
| PAN-7OH / 460 | NR | NR | 447 nm | 525 nm/564 nm | NR | NR | 443 nm | 513 nm/550 nm |
| PAN-4OH / 424 | NR | NR | 393 nm | 492 nm | NR | NR | 404 nm | 492 nm |
| PAN-1,5OH / 480 | NR | 567 nm | 573 nm | 602 nm | NR | NR | 482 nm | 568 nm |
| DAR / 433 | 333 nm/424 nm | 330 nm | 303 nm | 344 nm | 329 nm | 330 nm | 411 nm | 338 nm |
| QAN-1,5OH / 532 | NR | NR | 544 nm | NR | NR | NR | NR | NR |
| QAN-1A / 500 | 494 nm (S) | NR | 512 nm | 540 nm | NR | NR | NR | 528 nm |
| QAN-4OH / 460 | NR | 471 nm | 480 nm | 550 nm | NR | NR | 460 nm | 529 nm |
| QAN-7OH / 482 | NR | NR | NR | NR | NR | NR | NR | NR |
| PAR / 450 | NR | NR | 414 nm | 495 nm | NR | NR | 393 nm | 491 nm |
| QAR / 413 | NR | 463 nm | NR | 386 nm/492 nm | NR | NR | 413 nm | 388 nm/490 nm |
| DAN-4OH / 454 | NR | 503 nm | NR (S) | 502 nm | NR | NR | 465 nm | 491 nm |
| TMH-3-107C / 457 | NR | 463 nm | 458 nm | 491 nm | NR | NR | 473 nm | 487 nm |
| TMH-3-114C / 454 | NR | NR | 462 nm | NR | NR | NR | 477 nm | NR |
| TMH-3-109B / 462 | NR | 474 nm | S | 468 nm | 481 nm | NR | 447 nm | 467 nm |
| TMH-3-111c / 457 | NR | NR | 460 nm | 479 nm | NR | NR | 478 nm | 484 nm |
| OAN-4OH-5A-DPA / 447 | NR | 477 nm | NR | 488 nm | NR | NR | 454 nm | 486 nm |
| OAN-4-5A-DPA / 481 | NR | NR | NR (S) | 555 nm | NR | NR | 467 (S) | 566 nm |
| OAN-2-5A-DPA / 486 | NR | 523 nm | 485 nm | 534 nm | NR | NR | 485 nm | 521 nm |

Table II: Quick reference for metal response of azo dye library. In some cases, scattering was seen and is noted in the table with an “S”.

The responses for most dyes were a red shift in the absorbance spectrum. Green boxes indicate a significant shift in the spectrum when the metal is bound to the dye. Yellow boxes indicate where only a small shift (~10 nm) was seen, and red boxes are denoted with “NR” for “no response”.

| Solvent | Dipole moment (D) | λ_{\max} (nm) |
|---------------------------|--------------------------|---|
| Toluene | 0.3 | 492 |
| Chloroform | 1.2 | 476 |
| Diethyl Ether | 1.2 | 487 |
| Methylene Chloride | 1.6 | 502 |
| Isopropanol | 1.7 | 520 |
| Ethanol | 1.7 | 507 |
| T-butanol | 1.7 | 504 |
| Methanol | 1.7 | 510 |
| Ethyl Acetate | 1.8 | 491 |
| Pyridine | 2.4 | 591 |
| Triethyl Amine | 2.8 | 495 |
| Acetone | 2.9 | 508 |
| DMF | 3.8 | 580 |
| Acetonitrile | 3.9 | 563 |
| DMSO | 4.0 | 513 |

Table III: List of solvents tested while exploring the solvatochromism of QAN 1,5-OH. The dipole moment of the solvent was used as a measure of polarity. There appears to be a positive solvatochromic behavior but there are several unexplained exceptions that would be interesting to explore in the future work.¹¹¹⁻¹¹⁴

| PAN-7OH | Free Dye | Cu | Ni | Zn | Pb | Cd | Co |
|------------------------|--------------|-------------|--------------|--------------|--------------|--------------|-------------|
| pK_{a1} | 2.70 | 1.75 | 3.18 | 5.21 | 3.10 | 6.76 | 2.03 |
| total error (±) | 0.24 | 0.19 | 0.19 | 0.18 | 0.11 | 0.19 | 0.16 |
| pK_{a2} | 9.07 | 8.52 | 10.62 | 10.43 | 10.31 | 10.59 | 7.46 |
| total error (±) | 0.24 | 0.19 | 0.20 | 0.18 | 0.11 | 0.19 | 0.16 |
| pK_{a3} | 12.14 | N/A | N/A | N/A | 12.34 | N/A | N/A |
| total error (±) | 0.24 | N/A | N/A | N/A | 0.11 | N/A | N/A |

Table IV: Summary of pH studies for PAN-7OH and its metal complexes. The pK_a values for most metal complexes are similar to the free dye. The errors shown include regression and experimental errors. pK_{a3} was only modeled for Pb because it was too high to be modeled accurately for the others.

| PAN-7OH | K _D | K _D ' (M ⁻¹) | Ionic Radius (Å) |
|-----------|--|-------------------------------------|------------------|
| Cu | (3.999 ± 0.035) x 10⁻¹³ M⁻² | 6.324E-07 | 0.73 |
| Co | (7.396 ± 0.052) x 10⁻¹³ M⁻² | 8.600E-07 | 0.75 |
| Zn | (9.078 ± 0.050) x 10⁻¹³ M⁻² | 9.528E-07 | 0.74 |
| Ni | (9.419 ± 0.098) x 10⁻¹³ M⁻² | 9.705E-07 | 0.69 |
| Cd | (6.592 ± 0.013) x 10⁻¹¹ M⁻² | 8.119E-06 | 0.97 |
| Pb | (1.799 ± 0.050) x 10⁻⁵ M⁻¹ | 1.799E-05 | 1.2 |

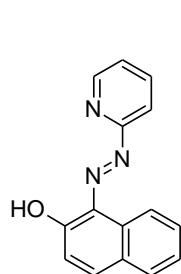
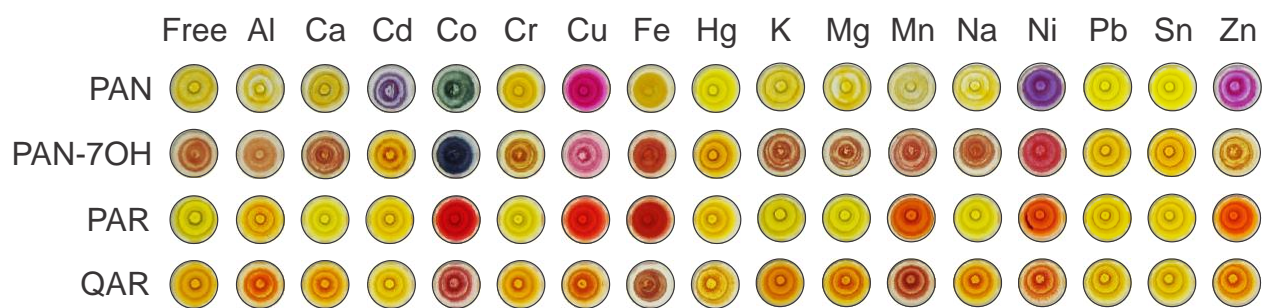
Table V: Binding affinities for metals. The K_D values for PAN-7OH and the metals that it binds. The K_D' value represents the square root of the K_D (for the 1:2 complexes) and are akin to a 1:1 binding affinity. The affinity for first row transition metals Cu, Ni, Zn, and Co are all very similar while the binding affinity is significantly less for bigger metals Pb and Cd.¹¹⁵ The size of these metal ions likely causes weaker binding to occur

| Sample Index | Prepared Concentration (μM) | | | | Model Predicted Concentration (μM) | | | | Error (μM) | | | | Total Error (μM) |
|--------------|--|------|------|------|---|------|-------|------|-------------------------|-------|-------|-------|-------------------------------|
| | Cu | Ni | Zn | Pb | Cu | Ni | Zn | Pb | Cu | Ni | Zn | Pb | |
| 1 | 0.00 | 2.73 | 0.00 | 0.00 | -0.04 | 2.90 | -0.20 | 0.13 | -0.04 | 0.17 | -0.20 | 0.13 | 0.54 |
| 2 | 3.78 | 2.04 | 1.84 | 0.00 | 3.53 | 2.00 | 1.87 | 0.07 | -0.24 | -0.05 | 0.03 | 0.07 | 0.39 |
| 3 | 1.89 | 2.11 | 2.20 | 0.00 | 1.93 | 2.38 | 2.20 | 0.07 | 0.05 | 0.27 | 0.00 | 0.07 | 0.38 |
| 4 | 1.95 | 2.73 | 2.14 | 0.00 | 1.93 | 2.78 | 2.05 | 0.11 | -0.02 | 0.05 | -0.09 | 0.11 | 0.27 |
| 5 | 1.51 | 2.52 | 2.81 | 0.00 | 1.57 | 2.56 | 2.53 | 0.06 | 0.05 | 0.04 | -0.29 | 0.06 | 0.44 |
| 6 | 3.15 | 3.41 | 0.61 | 0.00 | 3.07 | 3.40 | 0.65 | 0.01 | -0.08 | -0.01 | 0.04 | 0.01 | 0.15 |
| 7 | 2.14 | 2.45 | 1.71 | 0.00 | 2.04 | 2.47 | 1.67 | 0.03 | -0.10 | 0.02 | -0.04 | 0.03 | 0.20 |
| 8 | 1.83 | 2.11 | 1.77 | 1.74 | 1.90 | 2.30 | 1.45 | 1.76 | 0.07 | 0.19 | -0.32 | 0.02 | 0.61 |
| 9 | 1.76 | 1.98 | 1.65 | 2.32 | 1.95 | 2.21 | 1.52 | 2.42 | 0.19 | 0.24 | -0.14 | 0.10 | 0.66 |
| 10 | 1.57 | 1.70 | 1.53 | 3.07 | 1.71 | 2.11 | 1.37 | 3.09 | 0.14 | 0.41 | -0.16 | 0.02 | 0.73 |
| 11 | 1.32 | 1.43 | 1.28 | 3.59 | 1.47 | 1.66 | 1.01 | 3.37 | 0.15 | 0.23 | -0.27 | -0.22 | 0.86 |
| 12 | 0.94 | 1.02 | 0.92 | 4.11 | 1.01 | 1.52 | 0.72 | 4.16 | 0.07 | 0.50 | -0.20 | 0.05 | 0.81 |
| 13 | 2.33 | 1.43 | 2.08 | 0.64 | 2.46 | 1.68 | 1.71 | 0.67 | 0.13 | 0.24 | -0.37 | 0.03 | 0.79 |
| 14 | 2.14 | 2.79 | 0.67 | 0.93 | 2.32 | 3.07 | 0.49 | 0.94 | 0.18 | 0.28 | -0.18 | 0.01 | 0.65 |
| 15 | 2.14 | 1.16 | 2.51 | 1.27 | 2.24 | 1.41 | 2.10 | 1.40 | 0.10 | 0.25 | -0.41 | 0.12 | 0.89 |

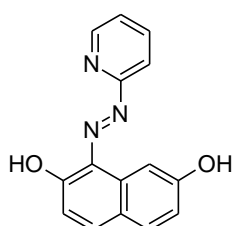
Table VI: PLS prediction results for the simultaneous determination of 4 metals. The determination of Cu, Ni, Zn, and Pb using PAR and QAR at pH 7.0 and 20°C was achieved with very little error ($<1\mu\text{M}$ total in all cases).

| Sample Index | Prepared Concentration (μM) | | | | Model Predicted Concentration | | | | Error (μM) | | | |
|---------------------------|--|------|------|------|-------------------------------|------|------|------|-------------------------|-------|-------|------|
| | Cu | Ni | Zn | Pb | Cu | Ni | Zn | Pb | Cu | Ni | Zn | Pb |
| 1 | 1.83 | 2.11 | 1.77 | 1.74 | 1.90 | 2.30 | 1.45 | 1.76 | 0.07 | 0.19 | -0.32 | 0.02 |
| 2 | | | | | 1.63 | 1.65 | 2.08 | 1.79 | -0.20 | -0.46 | 0.31 | 0.06 |
| 3 | | | | | 1.53 | 1.61 | 2.15 | 1.94 | -0.30 | -0.51 | 0.38 | 0.21 |
| 4 | | | | | 1.60 | 1.62 | 2.07 | 1.83 | -0.22 | -0.49 | 0.30 | 0.09 |
| 5 | | | | | 1.67 | 1.71 | 1.99 | 1.88 | -0.16 | -0.41 | 0.21 | 0.15 |
| 6 | | | | | 1.30 | 1.77 | 2.17 | 1.91 | -0.53 | -0.34 | 0.39 | 0.17 |
| 7 | | | | | 1.69 | 1.75 | 2.12 | 1.89 | -0.14 | -0.36 | 0.35 | 0.15 |
| 8 | | | | | 1.59 | 1.67 | 2.11 | 1.91 | -0.23 | -0.44 | 0.34 | 0.17 |
| 9 | | | | | 1.76 | 1.75 | 2.03 | 1.90 | -0.07 | -0.36 | 0.26 | 0.16 |
| 10 | | | | | 1.68 | 1.74 | 2.04 | 1.87 | -0.15 | -0.38 | 0.26 | 0.13 |
| 11 | | | | | 1.71 | 1.74 | 2.16 | 1.92 | -0.11 | -0.37 | 0.38 | 0.18 |
| 12 | | | | | 1.56 | 1.69 | 2.08 | 1.88 | -0.27 | -0.43 | 0.30 | 0.15 |
| 13 | | | | | 1.57 | 1.76 | 2.12 | 1.85 | -0.26 | -0.35 | 0.35 | 0.11 |
| 14 | | | | | 1.71 | 1.79 | 1.99 | 1.91 | -0.11 | -0.33 | 0.21 | 0.17 |
| 15 | | | | | 1.71 | 1.76 | 2.02 | 1.89 | -0.12 | -0.36 | 0.25 | 0.15 |
| 16 | | | | | 1.65 | 1.67 | 2.08 | 1.88 | -0.17 | -0.44 | 0.30 | 0.14 |
| 17 | | | | | 1.58 | 1.79 | 1.97 | 1.89 | -0.25 | -0.32 | 0.20 | 0.15 |
| 18 | | | | | 1.57 | 1.76 | 2.04 | 1.92 | -0.26 | -0.35 | 0.27 | 0.18 |
| 19 | | | | | 1.77 | 1.76 | 2.02 | 1.88 | -0.06 | -0.35 | 0.25 | 0.14 |
| Mean | | | | | | | | | -0.19 | -0.36 | 0.26 | 0.14 |
| Standard Deviation | | | | | | | | | 0.12 | 0.14 | 0.15 | 0.04 |

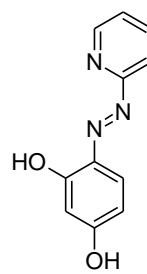
Table VII: PLS prediction results for solutions (n=19) of Cu, Ni, Zn, and Pb using PAR and QAR at pH 7.0 and 20°C. The mean error was less than 0.4 μM and the standard deviation was less than 0.15 for all metals.



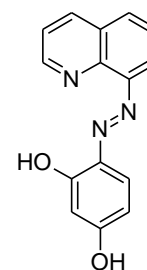
PAN



PAN-7OH



PAR



QAR

Figure 14: Visual response of four dyes to 16 metals (pH 7.0). Even for similar responses, there is enough spectral information so that multiple metals can be distinguished.

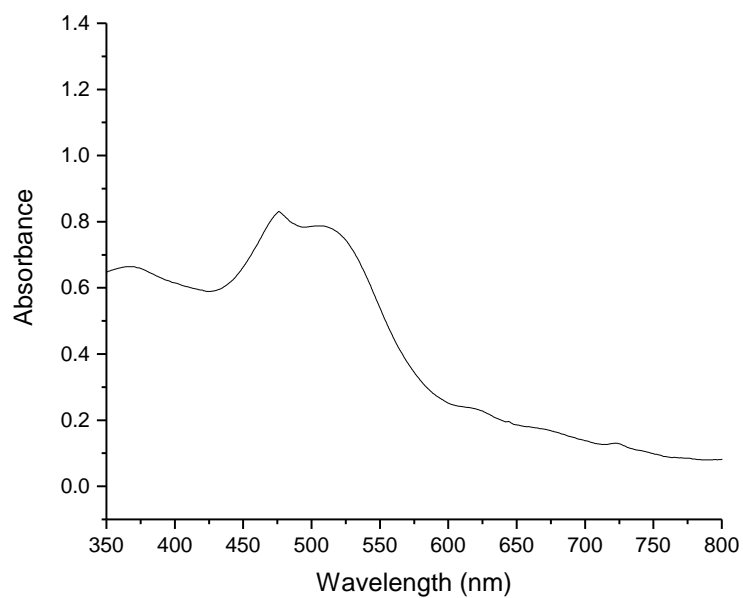
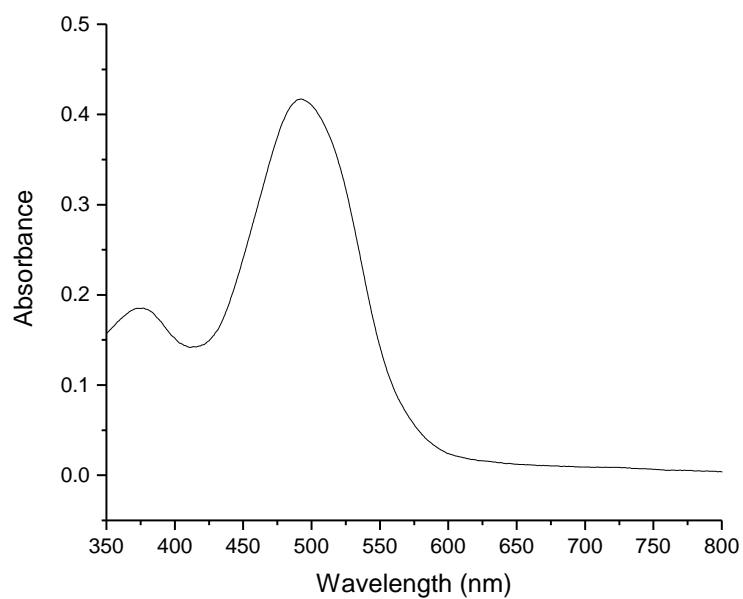


Figure 15: QAN 1,5-OH (325 μ M) in less polar solvents toluene and chloroform. The λ_{max} is blue shifted relative to several more polar solvents. This would lead to the classification of positive solvatochromism for this dye.

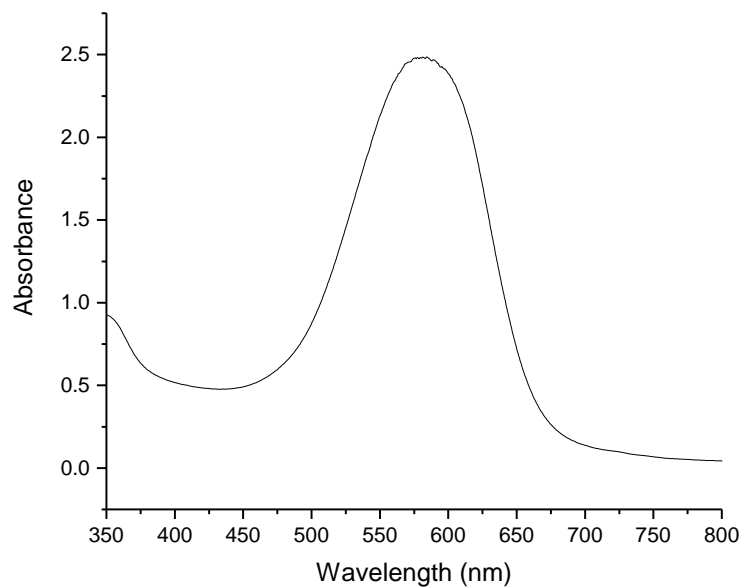
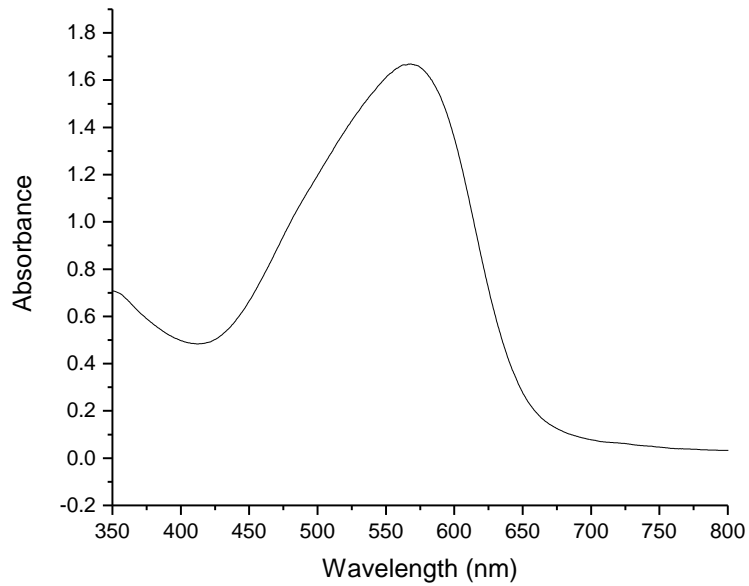


Figure 16: Solvatochromism of QAN-1,5OH in more polar solvents (acetonitrile and DMF). The spectra are red shifted in these solvents with higher polarity which indicates that QAN 1,5-OH can be classified as a positive solvatochromic dye.

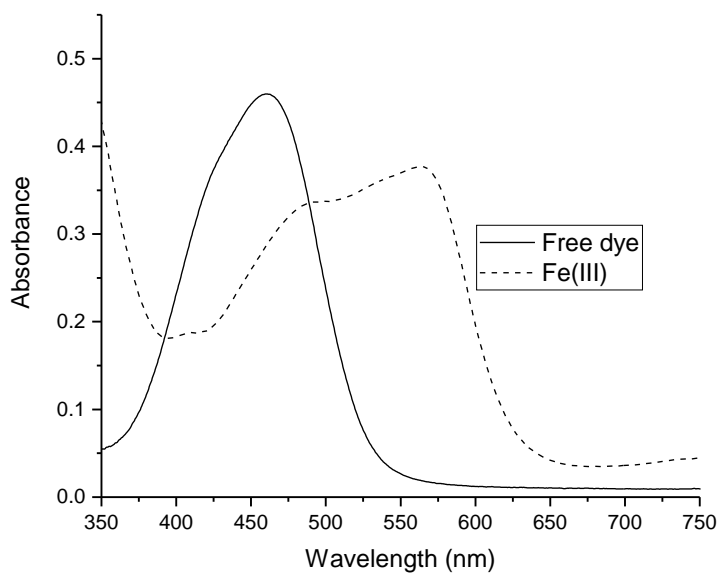
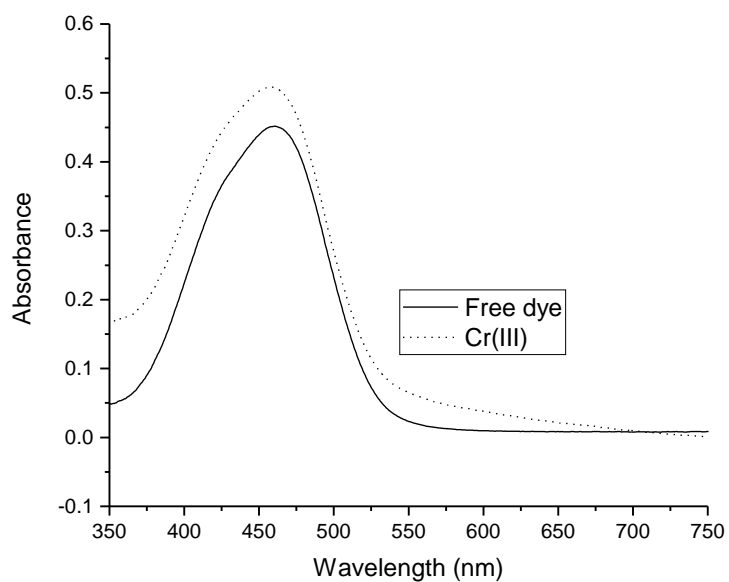


Figure 17: Metal complex aggregation is seen with certain buffers. The scattering was eliminated for PAN-7OH with Cr(III) and Fe(II) by using different buffers. There was no response for Cr(III) in EPPS buffer at pH 7.5 (top) while there were spectral changes seen for Fe(II) in acetate buffer at pH 4.7 (bottom).

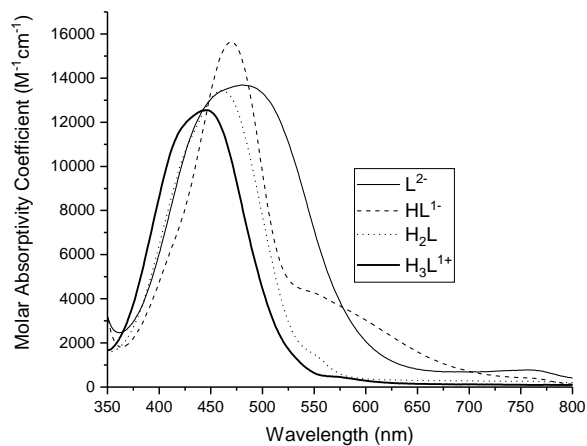
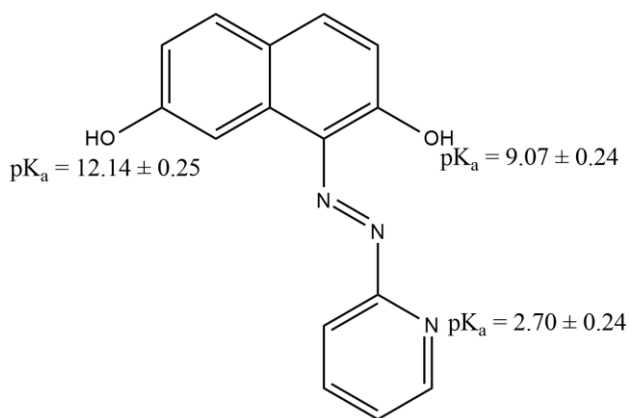
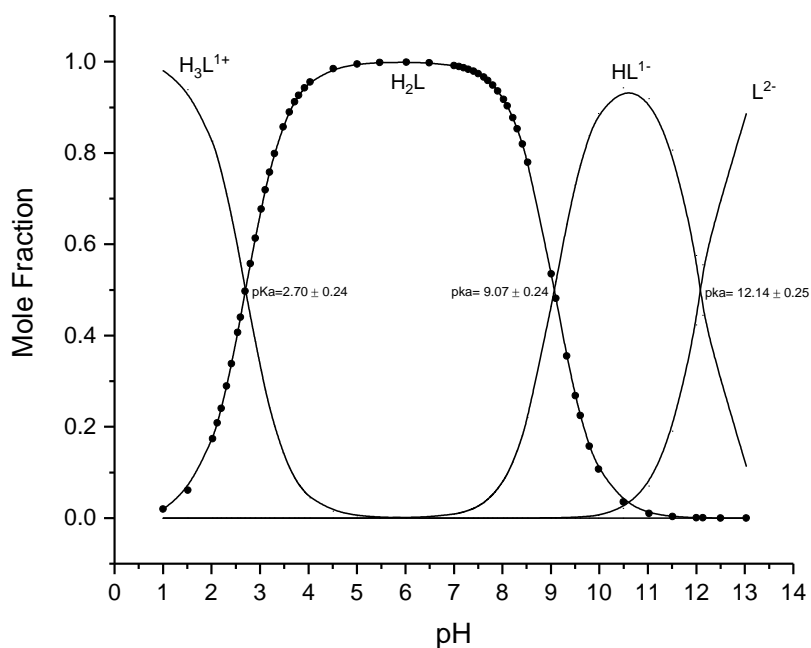


Figure 18: PAN-7OH pK_a results. The results for the pK_a testing on PAN-7OH are shown with the species distribution and decomposed spectra from Reactlab analysis. The decomposed spectra show 4 distinct species that exist over the pH region tested. The species distribution identifies pK_a values where species exist in a 50:50 ratio.

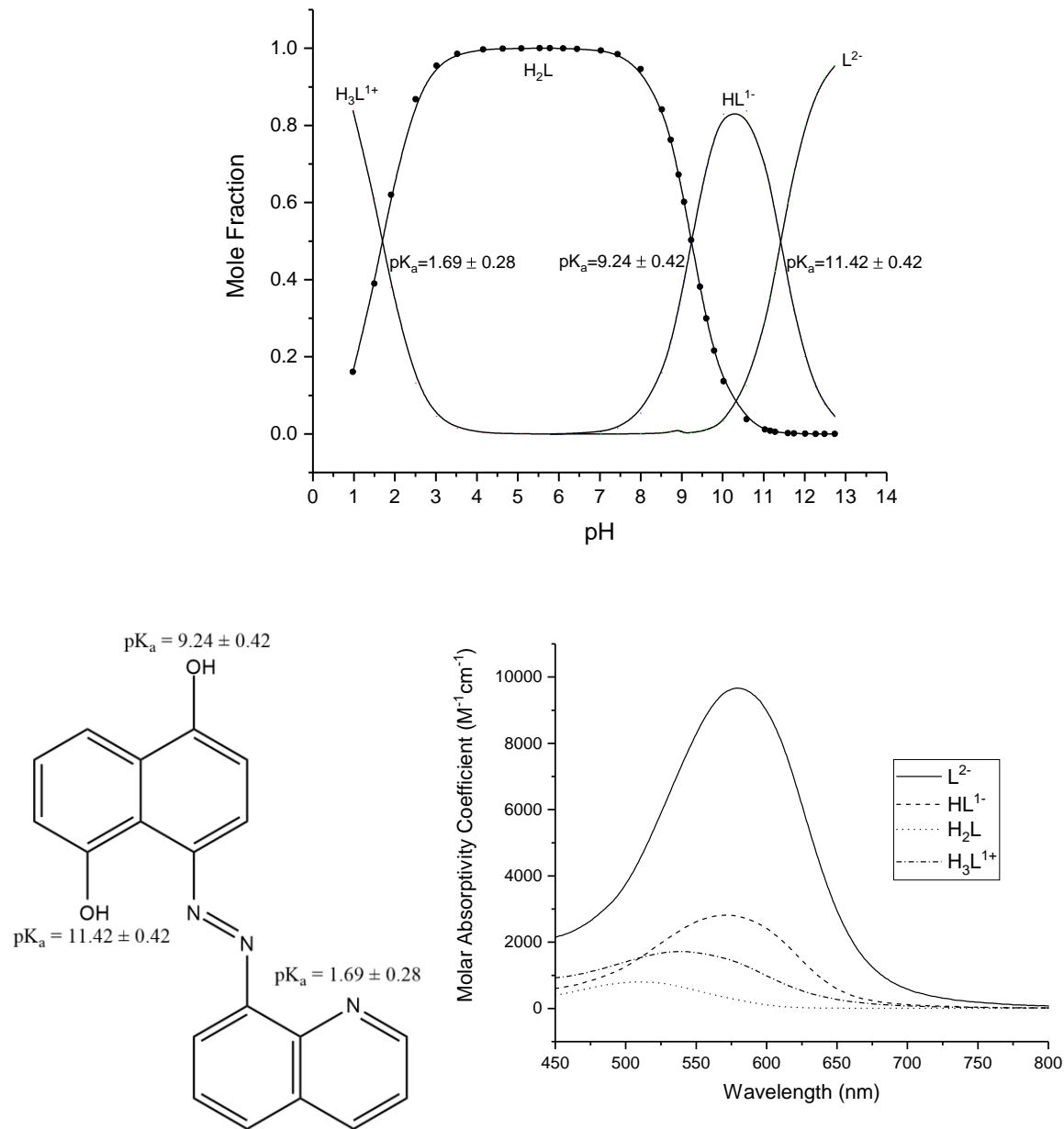


Figure 19: QAN-1,5OH pK_a values. The results for the pK_a testing on QAN-1,5OH are shown with the species distribution and decomposed spectra from Reactlab analysis. The first and third pK_a values are lower than PAN-7OH and the middle pK_a is slightly higher. The decomposed spectra show that the completely deprotonated has a molar absorptivity coefficient that is nearly five times higher than that of the other species.

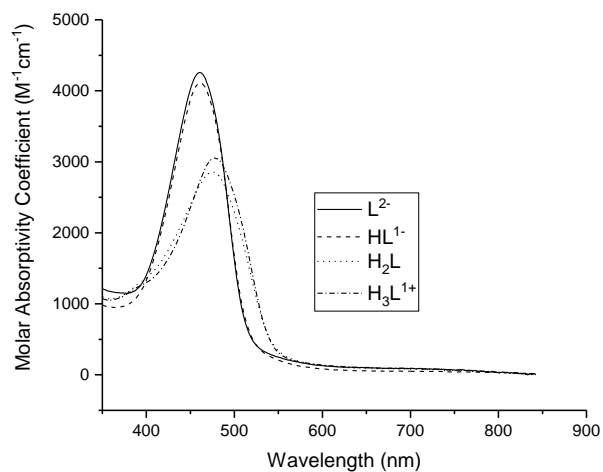
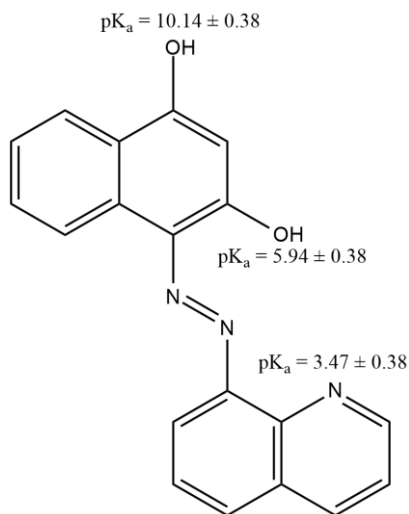
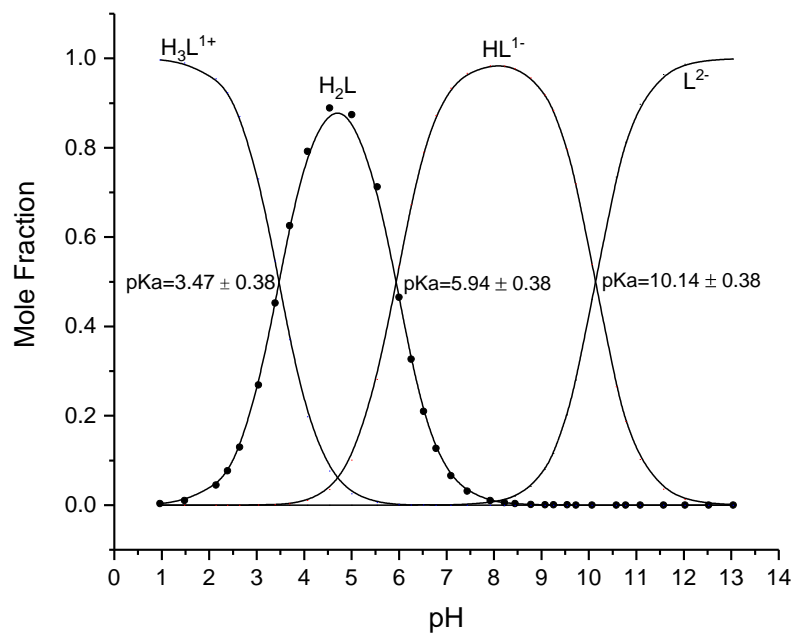
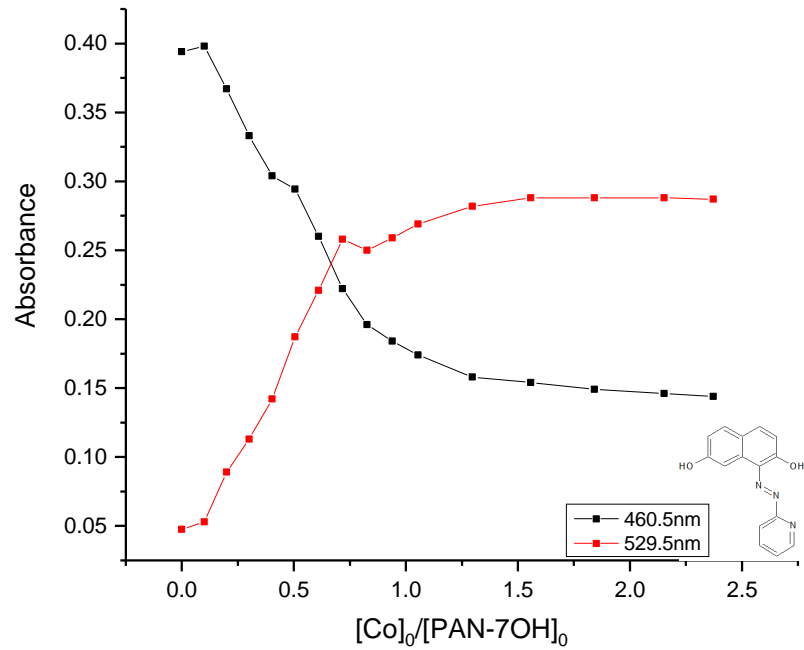
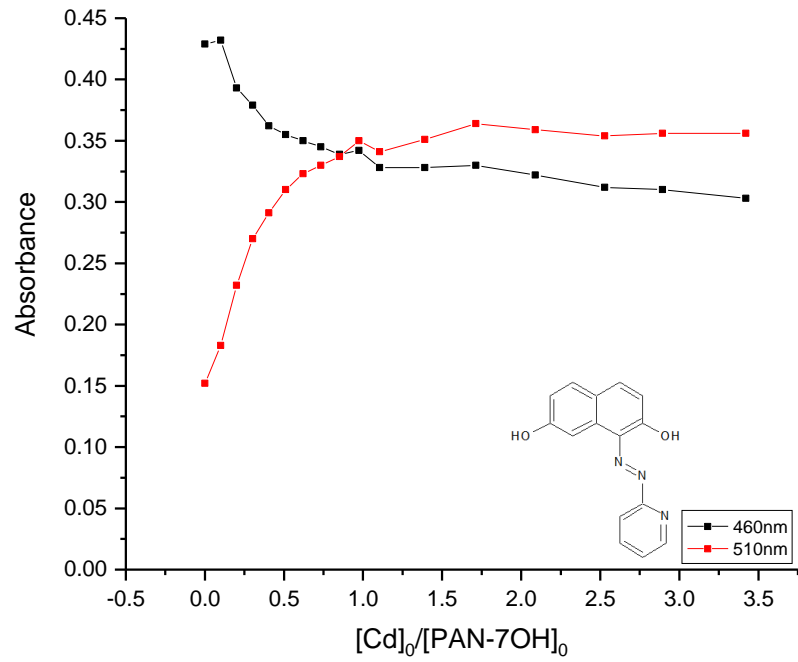
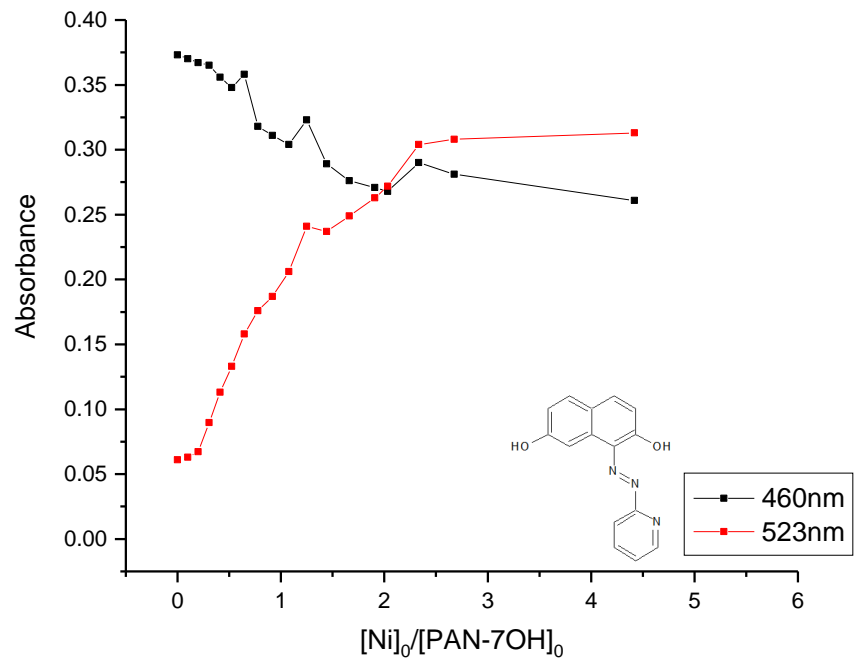
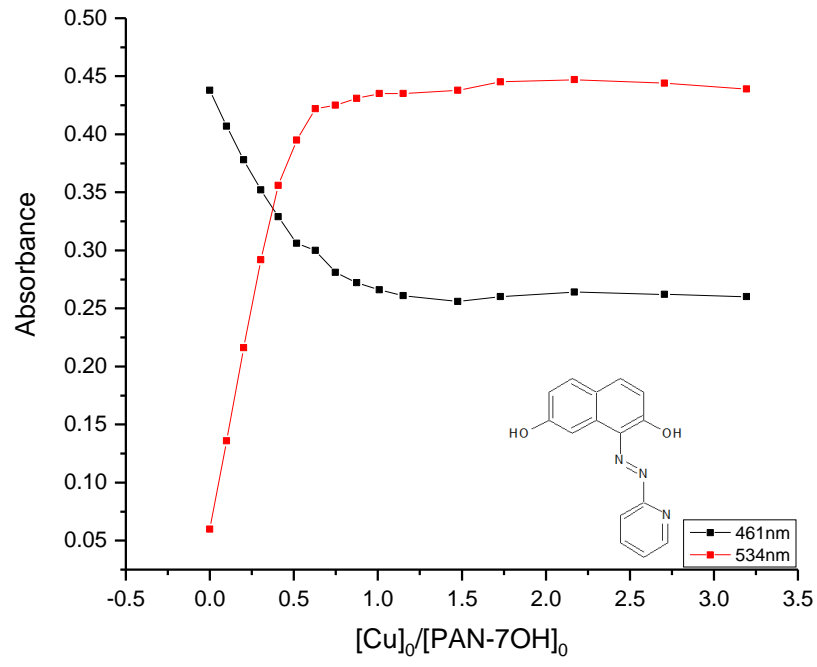


Figure 20: QAN-4OH pK_a results. The results for the pK_a testing on QAN-4OH are shown with the species distribution and decomposed spectra from Reactlab analysis. The L^{2-} and HL^{1-} decomposed spectra are very similar and this may be a result of the model overfitting. This results in the first two pK_a values being very close together.





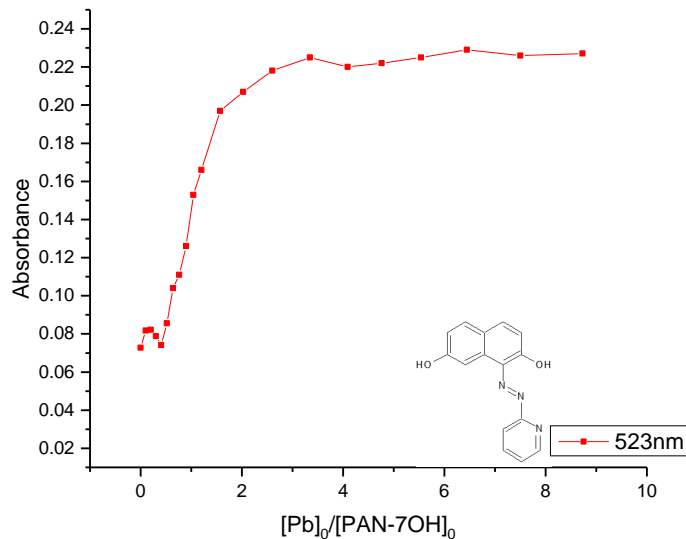
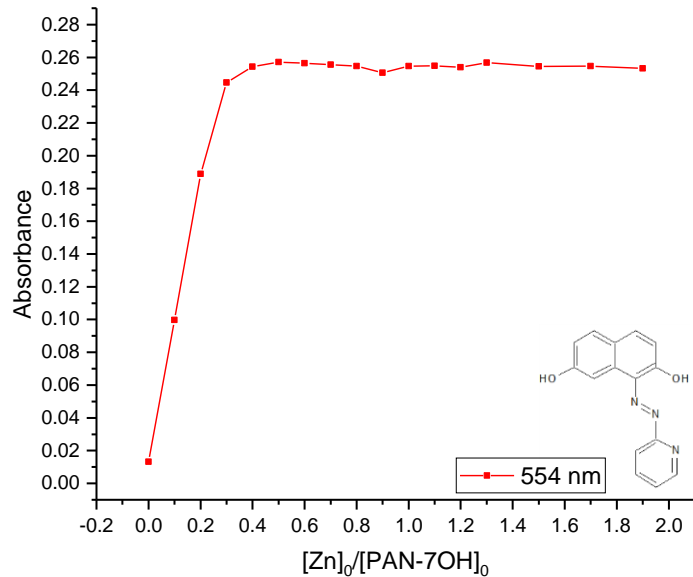


Figure 21: Initial binding ratio studies for PAN-7OH. All metals bind in a 1:2 (M:L) ratio except for Pb which shows 1:1 binding. By tracking the disappearance of the free dye spectral peak (red) or appearance of the metal-dye complex peak (black) the binding ratio can be determined. Some binding curves, such as Ni, are not clear results. Nevertheless, the 1:2 binding model was used for all metals except Pb because previous studies and model fitting.

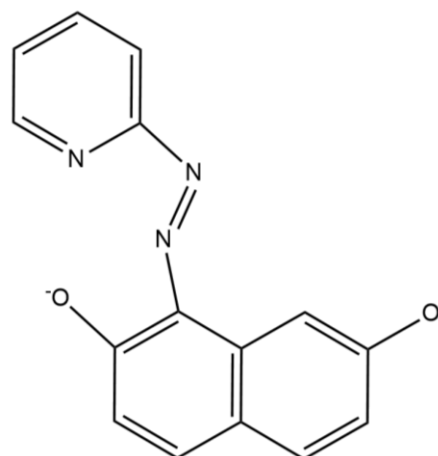
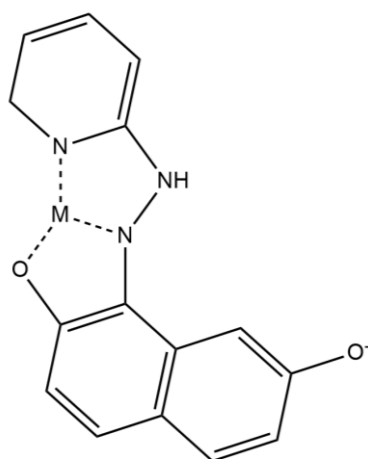
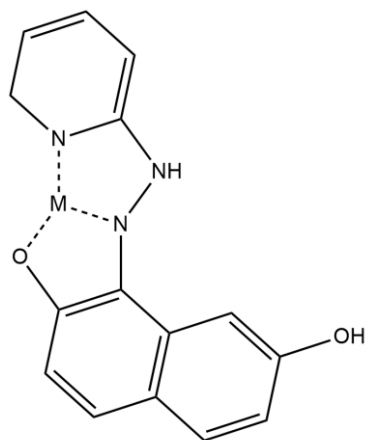
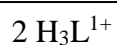
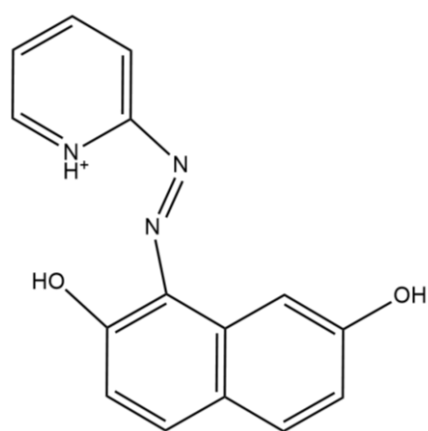


Figure 22: Modeled species for metal complex pH studies. The decomplexation occurs in all cases at low pH. It appears that it also occurs at high pH but was only modeled effectively in the case of Pb. There is only one dye shown in these structures for simplicity, but they do bind in a 1:2 fashion for all metals but Pb.

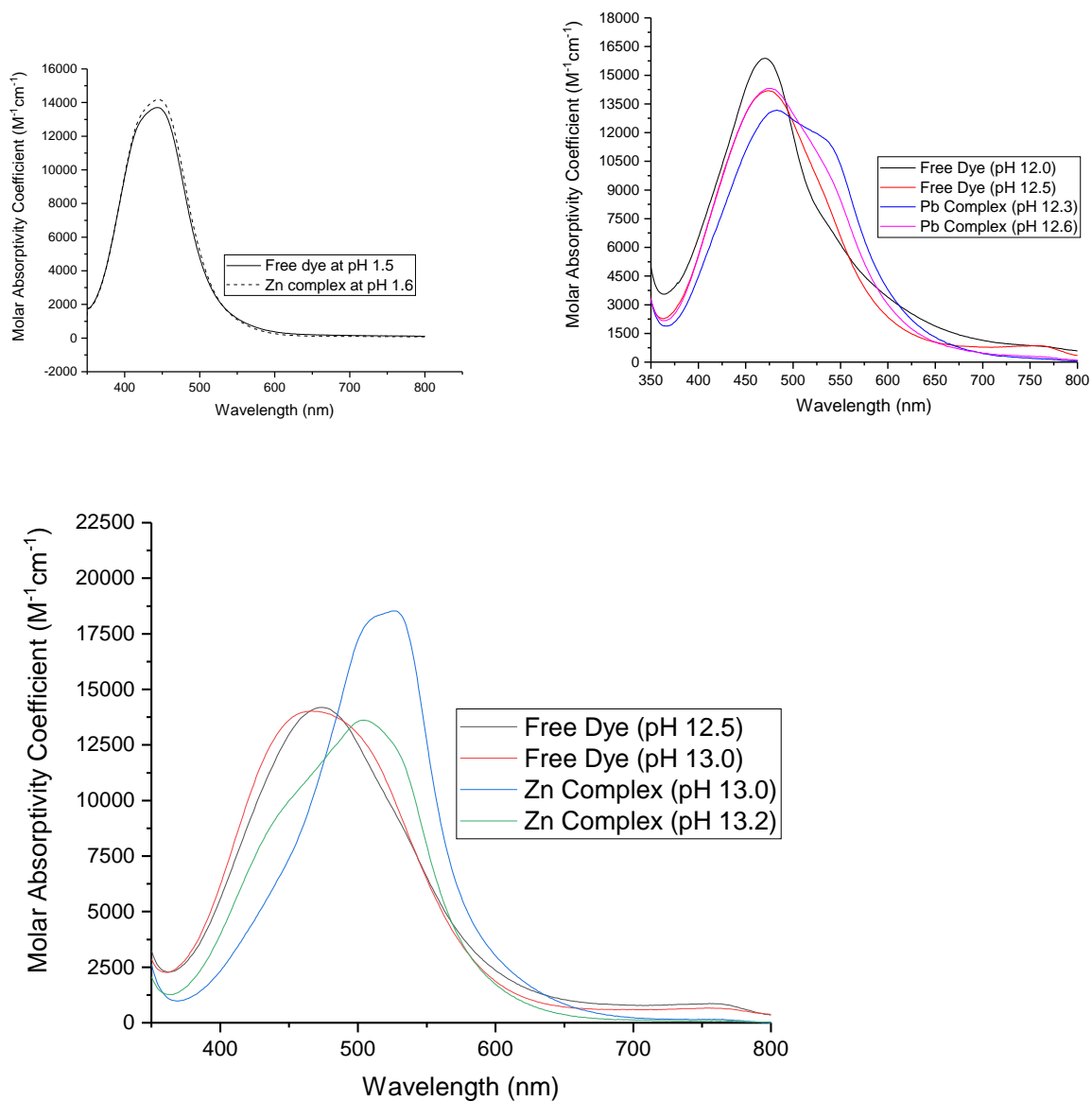


Figure 23: Decomplexation at low and high pH. The metal complex spectra for the Zn experiment looks like the free dye at low pH (top left). The spectra for the complex shown at high pH begin to shift towards the free dye peak but this is not enough to accurately model (top right). The decomplexation of the Pb complex is complete enough to model at the pH values tested (bottom left).

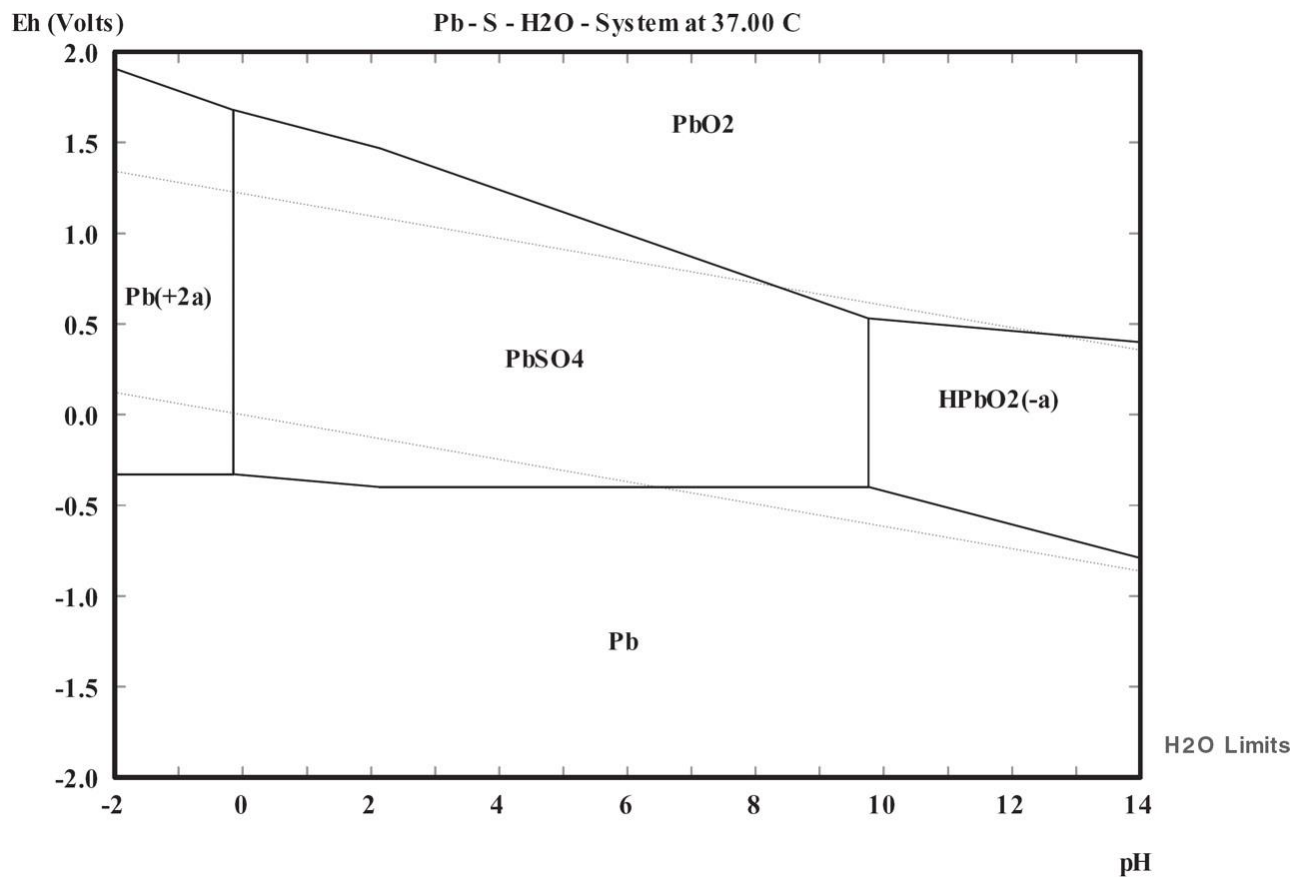
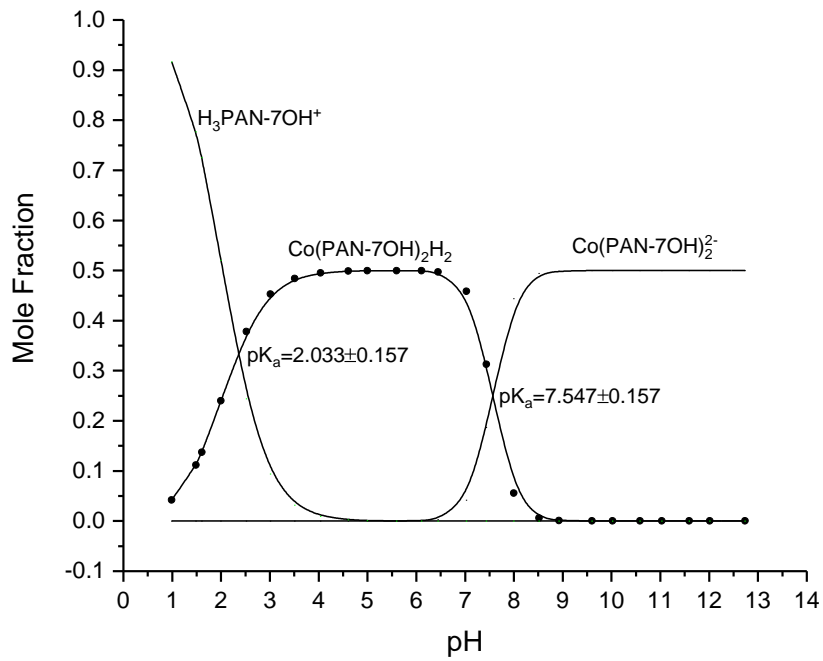
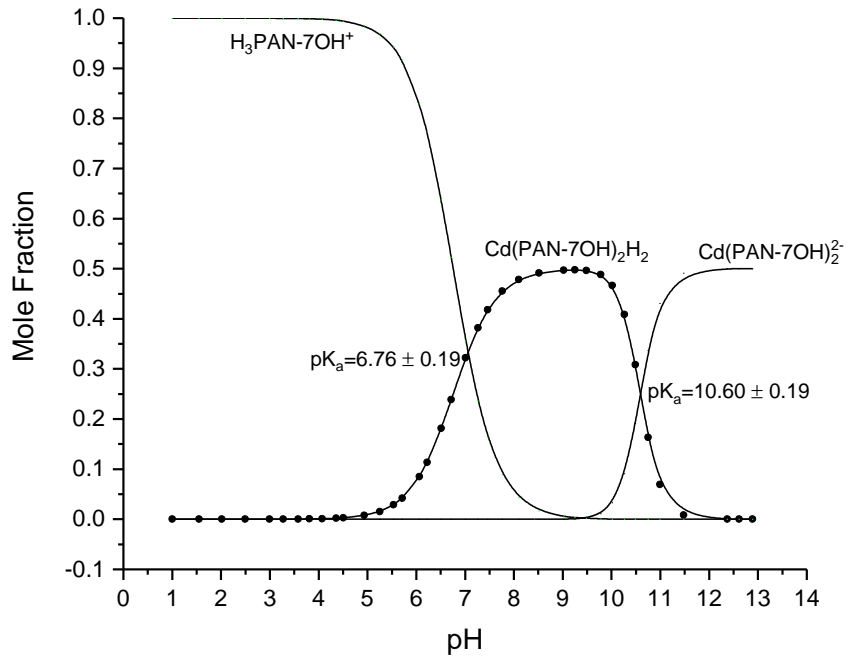
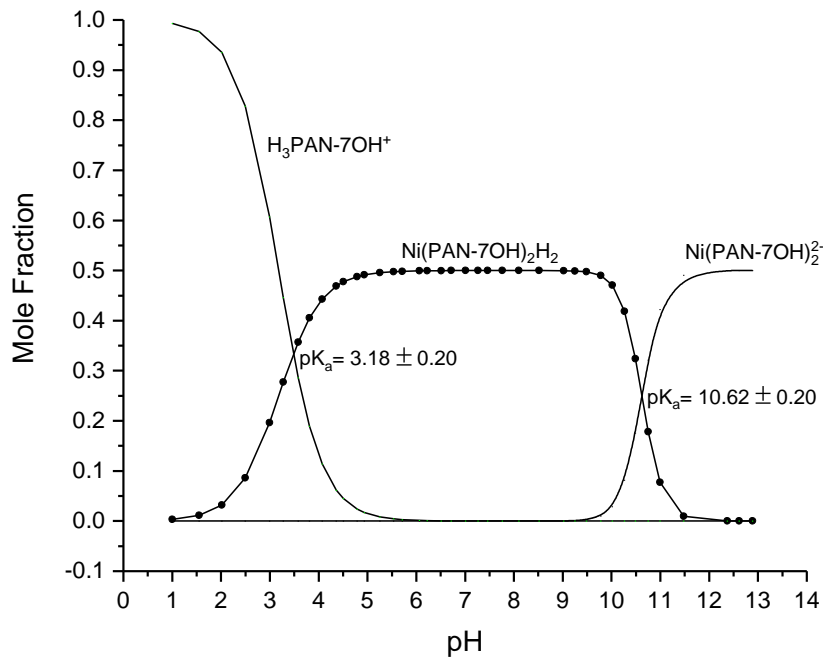
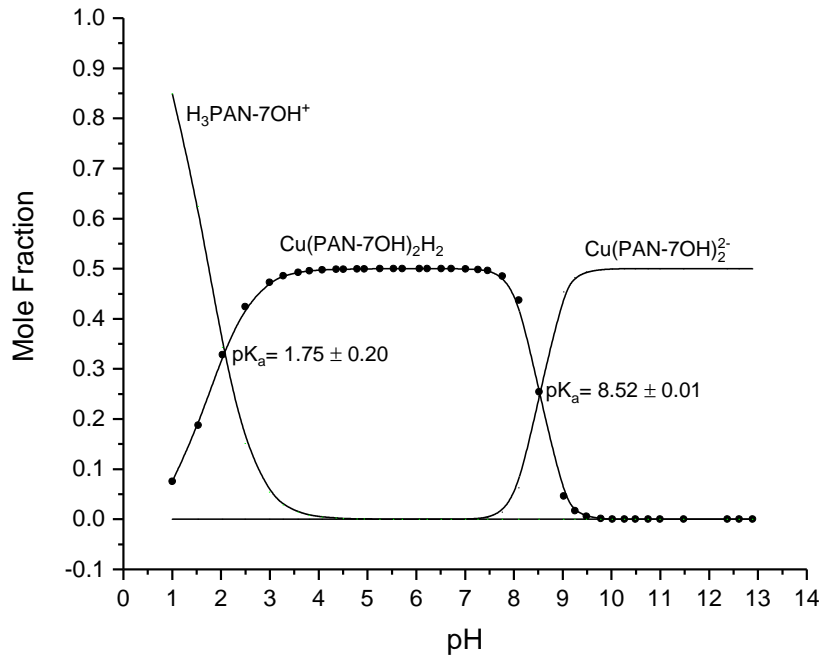


Figure 24: Pourbaix diagram for Pb showing the formation of Pb/O compounds at higher pH values. The formation of metal oxides and metal hydroxides is likely the cause of decomplexation at high pH. There is a competition between forming a complex with the dye and complexing oxygen.





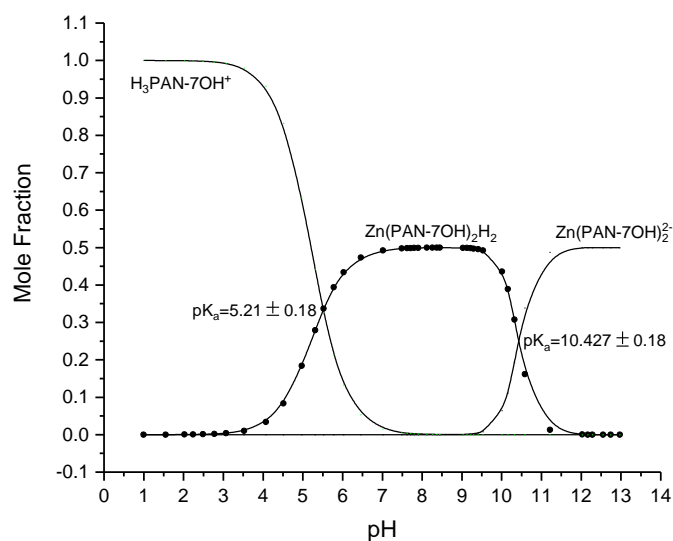
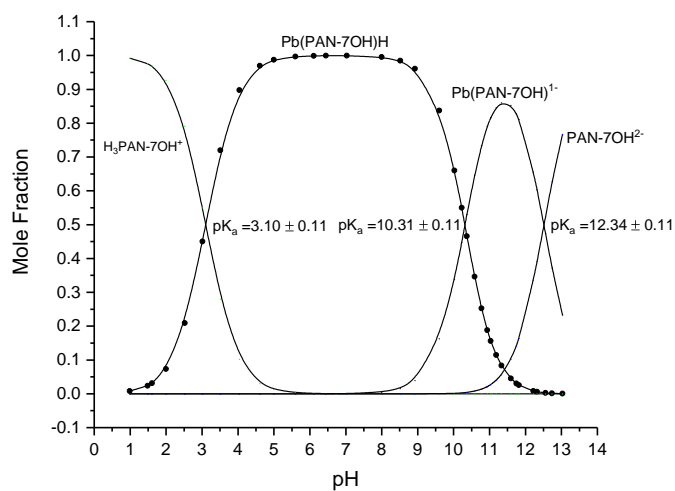


Figure 25: Species distribution of PAN-7OH metal complexes (previous pages). The species distribution of the metal complexes of PAN-7OH are made with computed concentrations of each species from the Reactlab analysis. All complexes were modeled as 1:2 binding except for Pb. The first pK_a values is decomplexation at low pH, the second is deprotonation of the complex, and the third (Pb) is the decomplexation at high pH because metal hydroxide and oxide formation.

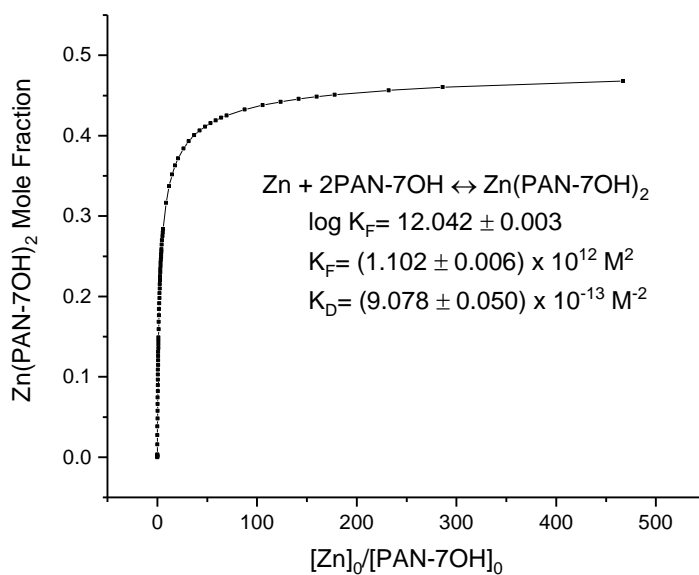
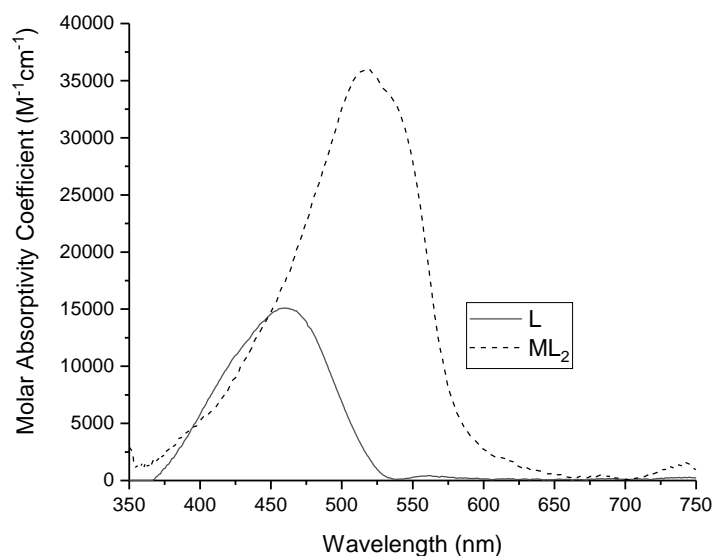


Figure 26: Binding affinity curve of PAN-7OH and Zn (left) and decomposed spectra (right) for PAN-7OH metal complex. The curve shows good hyperbolicity with the $[dye]_0 \approx K_D$. The decomposed spectra show good agreement with the raw data which is one indicator that the model is fitting correct species.

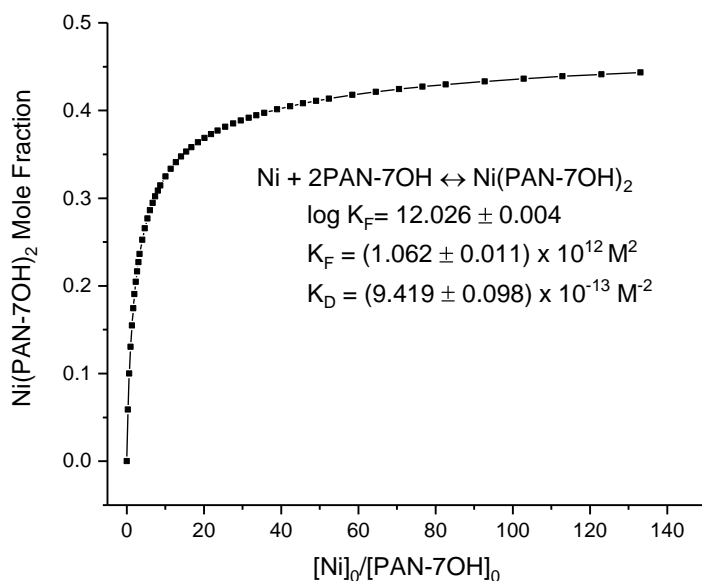
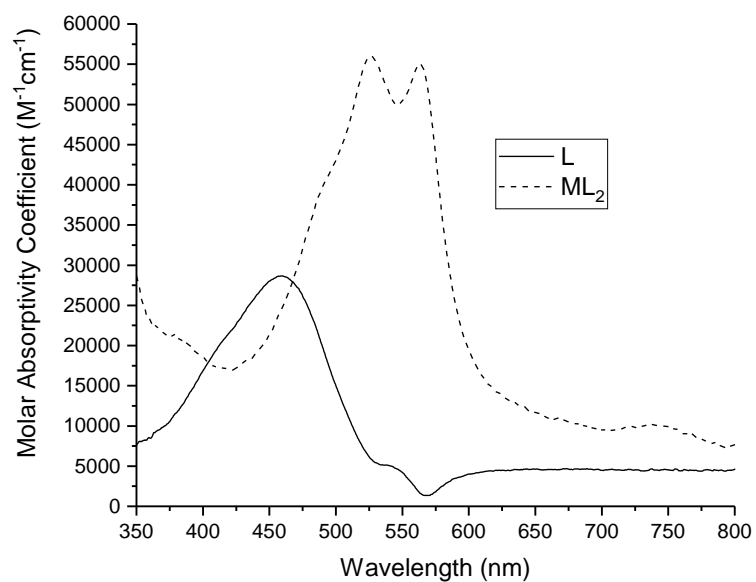


Figure 27: Binding affinity curve of PAN-7OH and Ni (left) and decomposed spectra (right) for PAN-7OH metal complex. The curve shows good hyperbolicity with the $[dye]_0 \approx K_D$. The decomposed spectra show good agreement with the raw data which is one indicator that the model is fitting correct species.

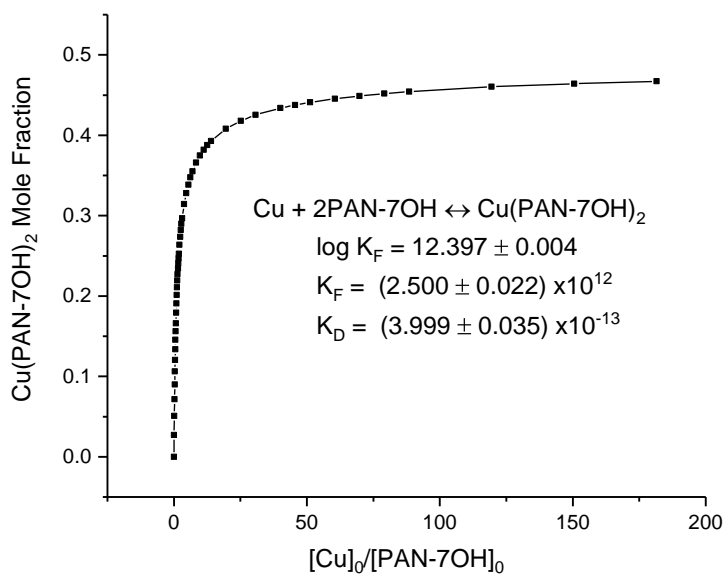
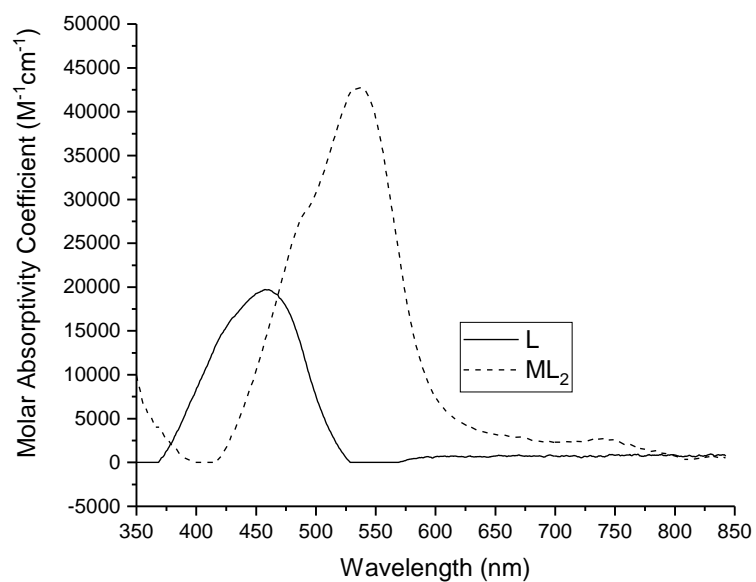


Figure 28: Binding affinity curve of PAN-7OH and Cu (left) and decomposed spectra (right) for PAN-7OH metal complex. The curve shows good hyperbolicity with the $[dye]_0 \approx K_D$. The decomposed spectra show good agreement with the raw data which is one indicator that the model is fitting correct species.

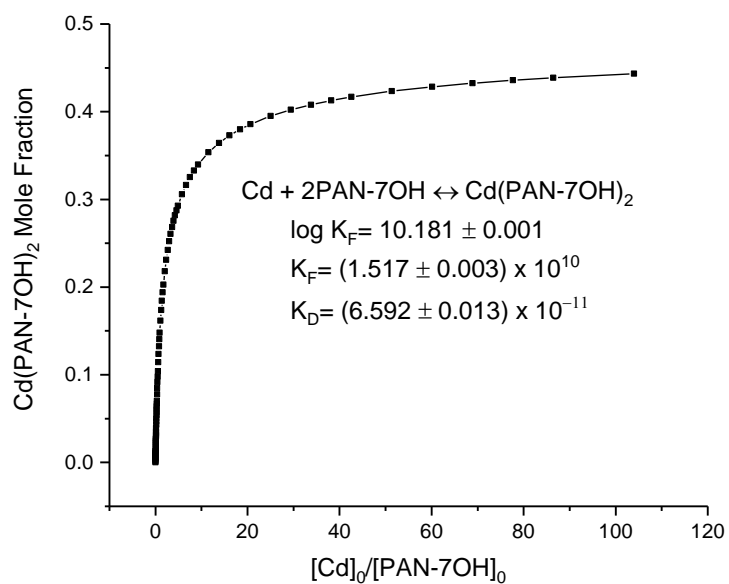
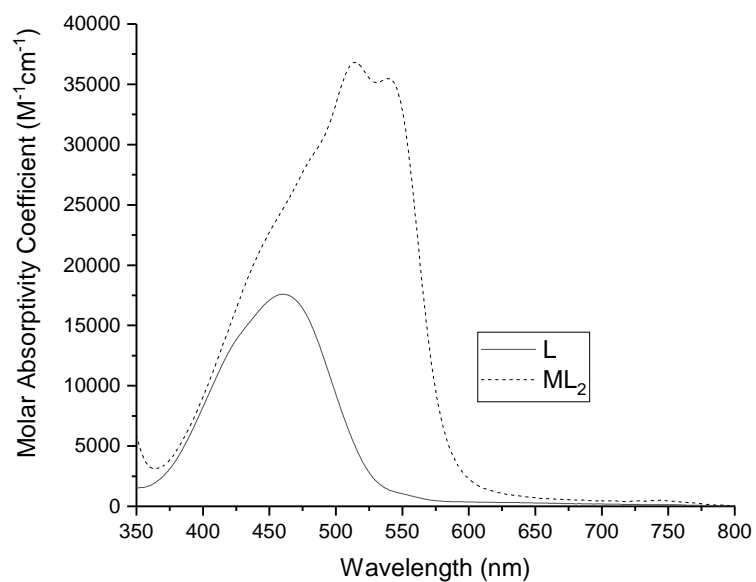


Figure 29: Binding affinity curve of PAN-7OH and Cd (left) and decomposed spectra (right) for PAN-7OH metal complex. The curve shows good hyperbolicity with the $[\text{dye}]_0 \approx K_D$. The decomposed spectra show good agreement with the raw data which is one indicator that the model is fitting correct species.

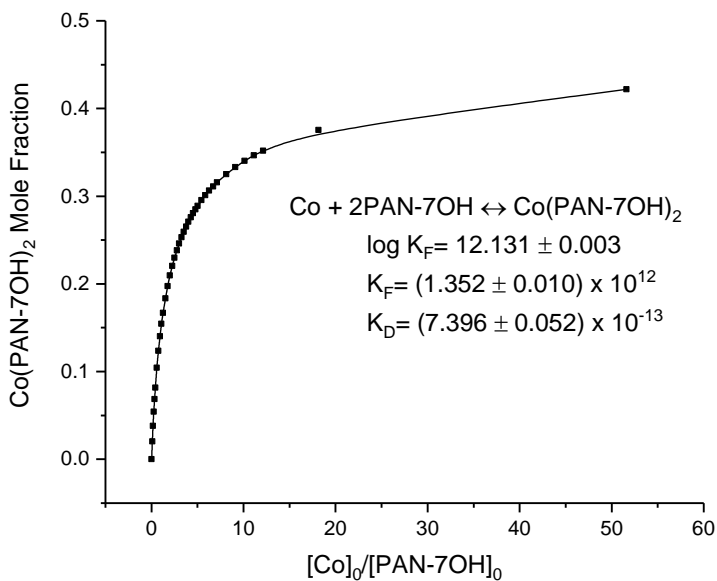
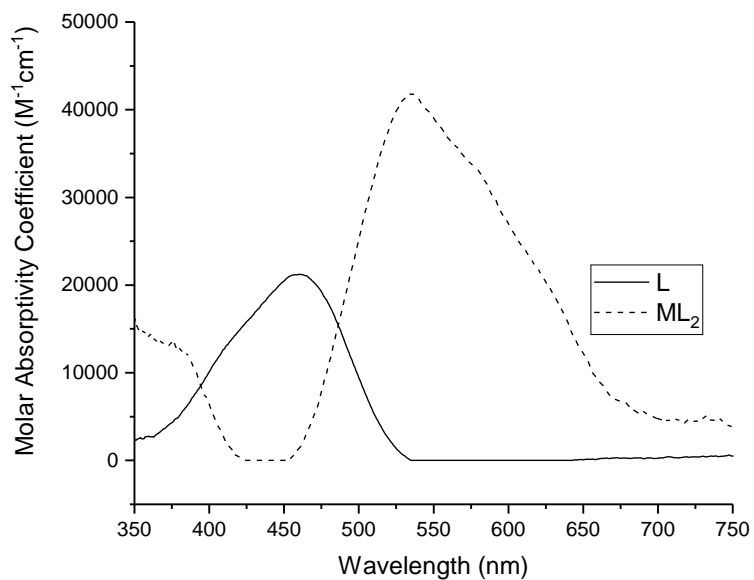


Figure 30: Binding affinity curve of PAN-7OH and Co (left) and decomposed spectra (right) for PAN-7OH metal complex. The curve shows good hyperbolicity with the $[\text{dye}]_0 \approx K_D$. The decomposed spectra show good agreement with the raw data which is one indicator that the model is fitting correct species.

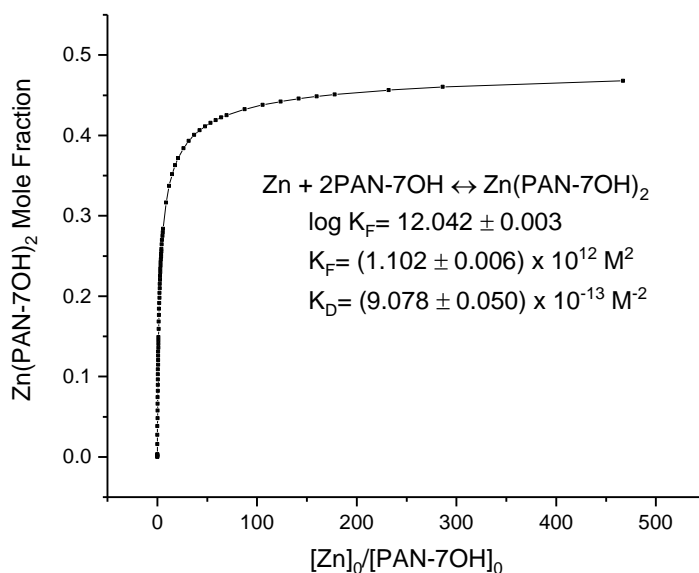
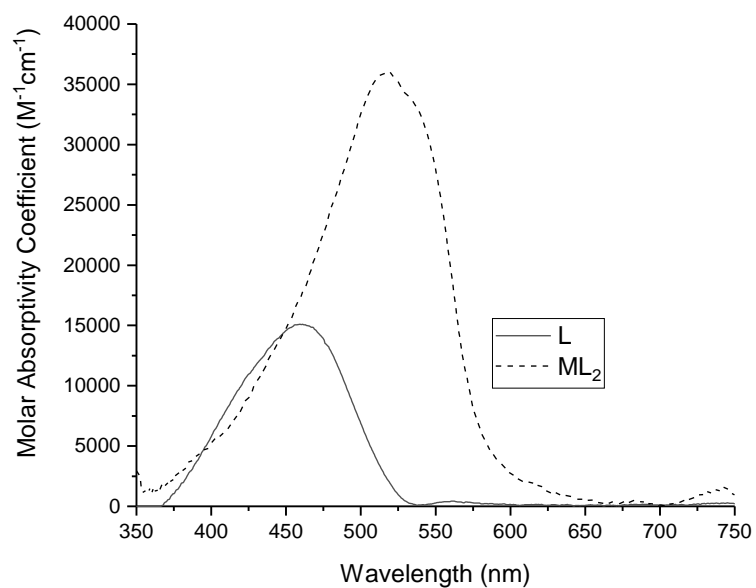


Figure 31: Binding affinity curve of PAN-7OH and Zn (left) and decomposed spectra(right)for PAN-7OH metal complex. The curve shows good hyperbolicity with the $[dye]_0 \approx K_D$. The decomposed spectra show good agreement with the raw data which is one indicator that the model is fitting correct species. Pb was modeled as a 1:1 binding.

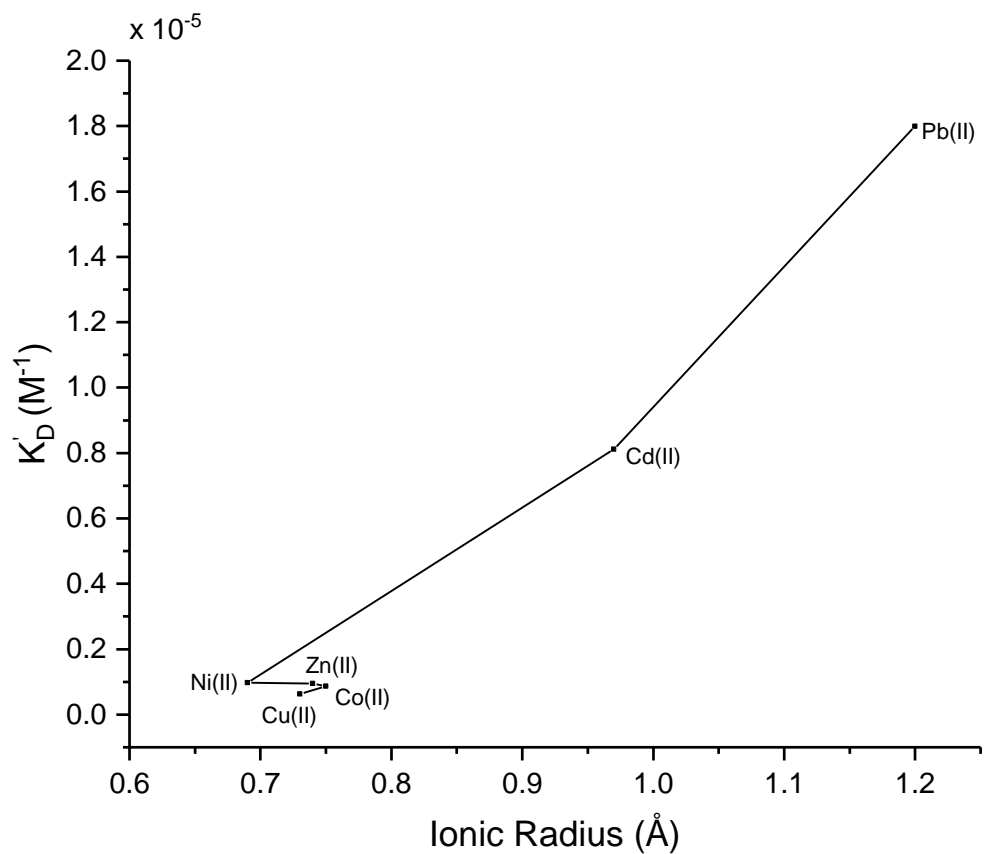


Figure 32: The binding affinity of PAN-7OH increases relative to ionic radius. The smaller ions such as Cu(II), Co(II), Zn(II), and Ni(II) have much smaller K_D values than that of Cd(II) and Pb(II).

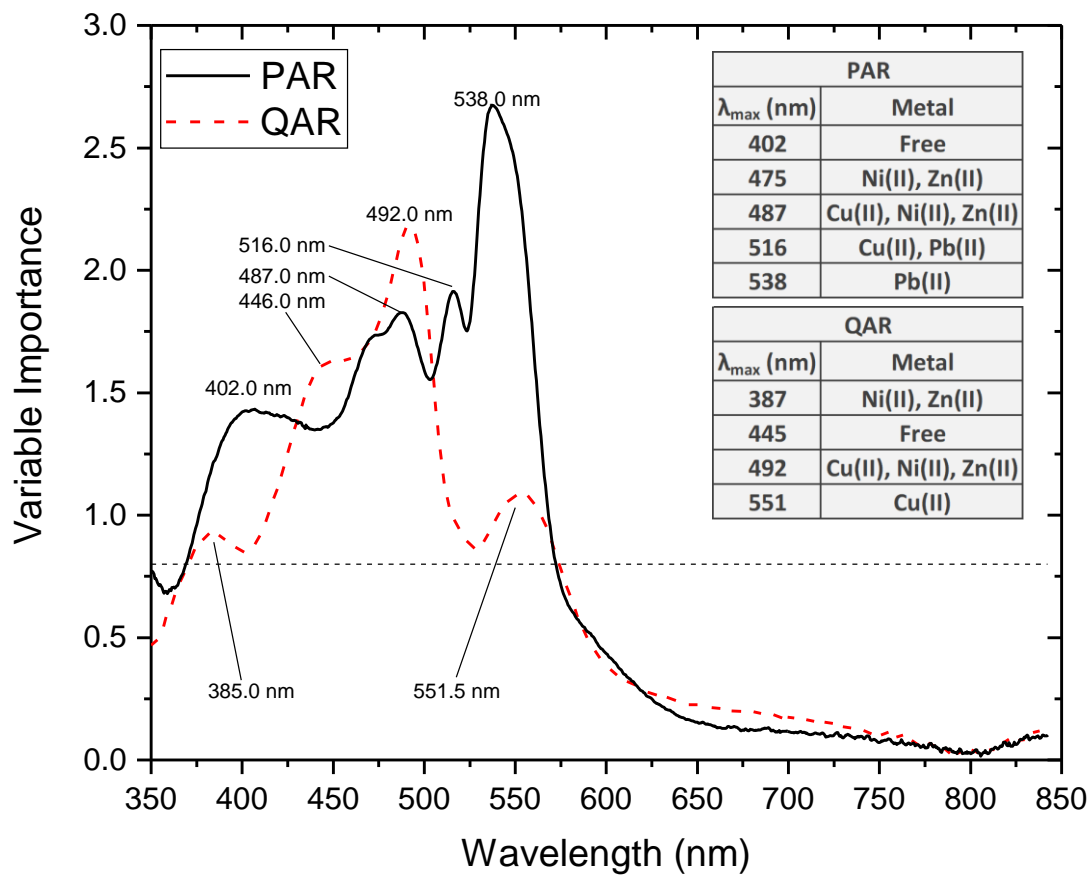


Figure 33: Example Variable Importance Plot (VIP) for PLS analysis. The VIP can give insight into important spectral features that improve the model. The peaks of the plot correspond to free and bound dye peaks. The best interpretation of these peaks is shown in the inset tables.

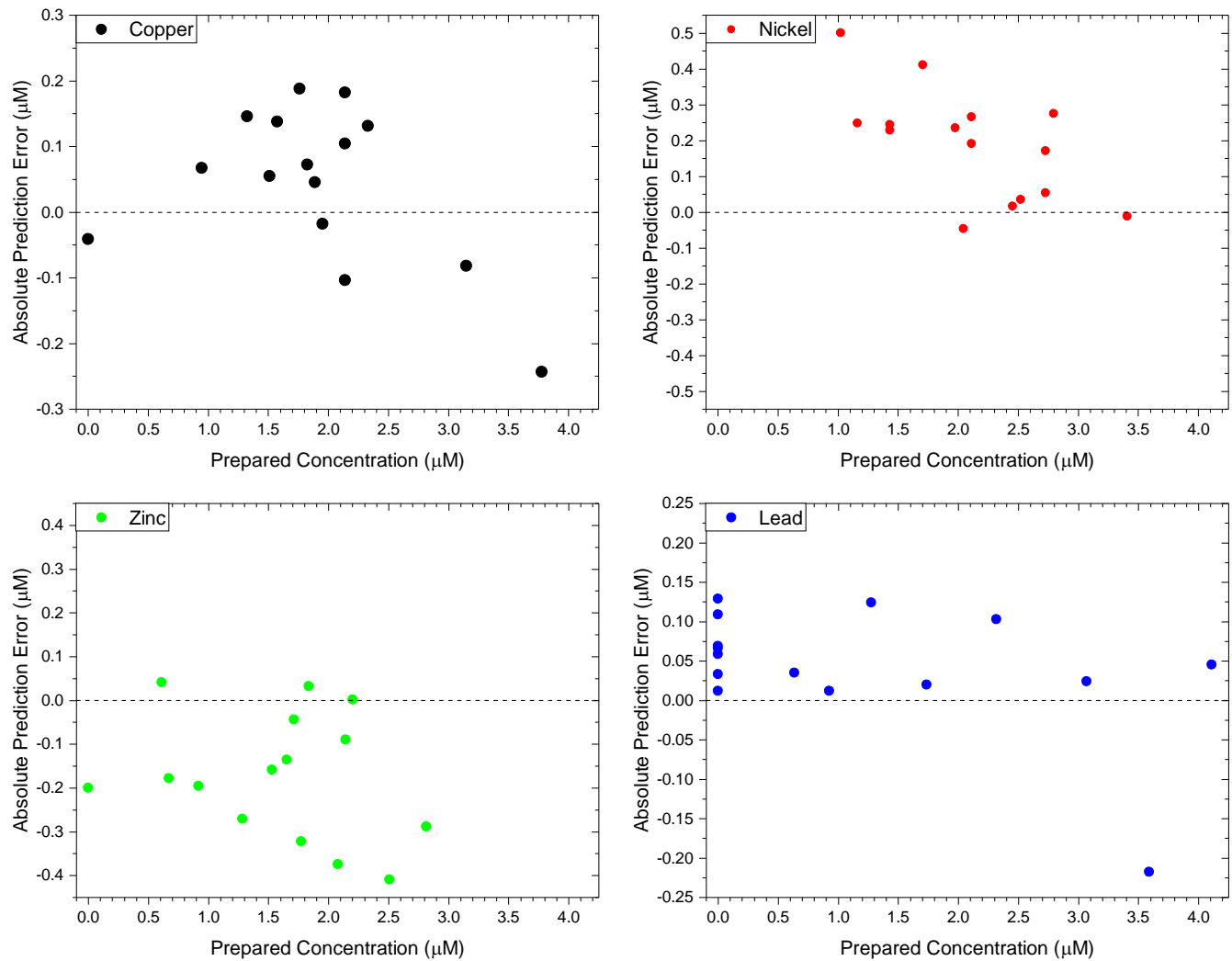


Figure 34: Plots of absolute prediction error of pseudo-unknown samples. The errors are relatively low and do not seem to follow a trend among the four metals.

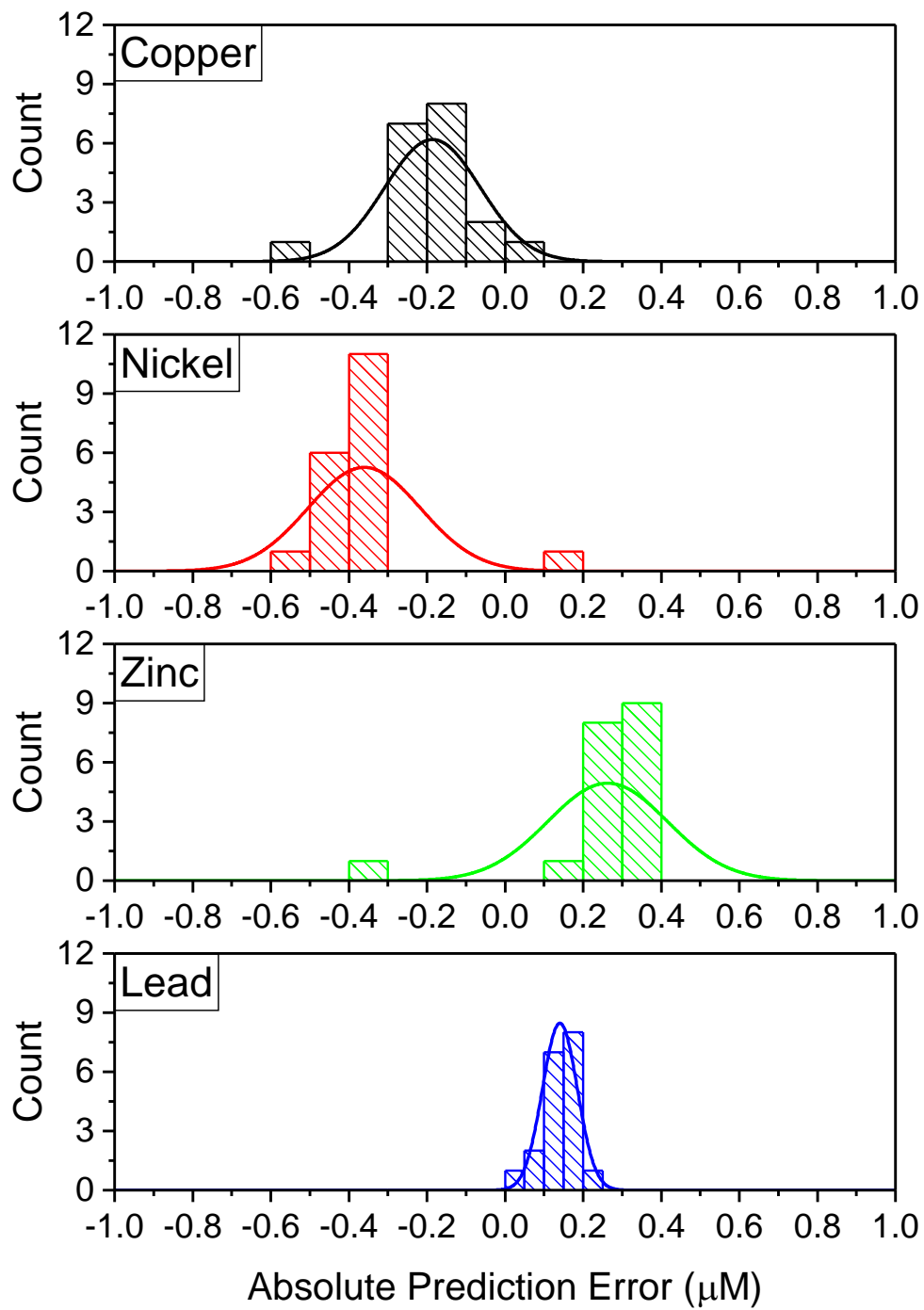


Figure 35: Distribution of absolute prediction errors. The predictor error is generally gaussian in shape and were low in all samples.

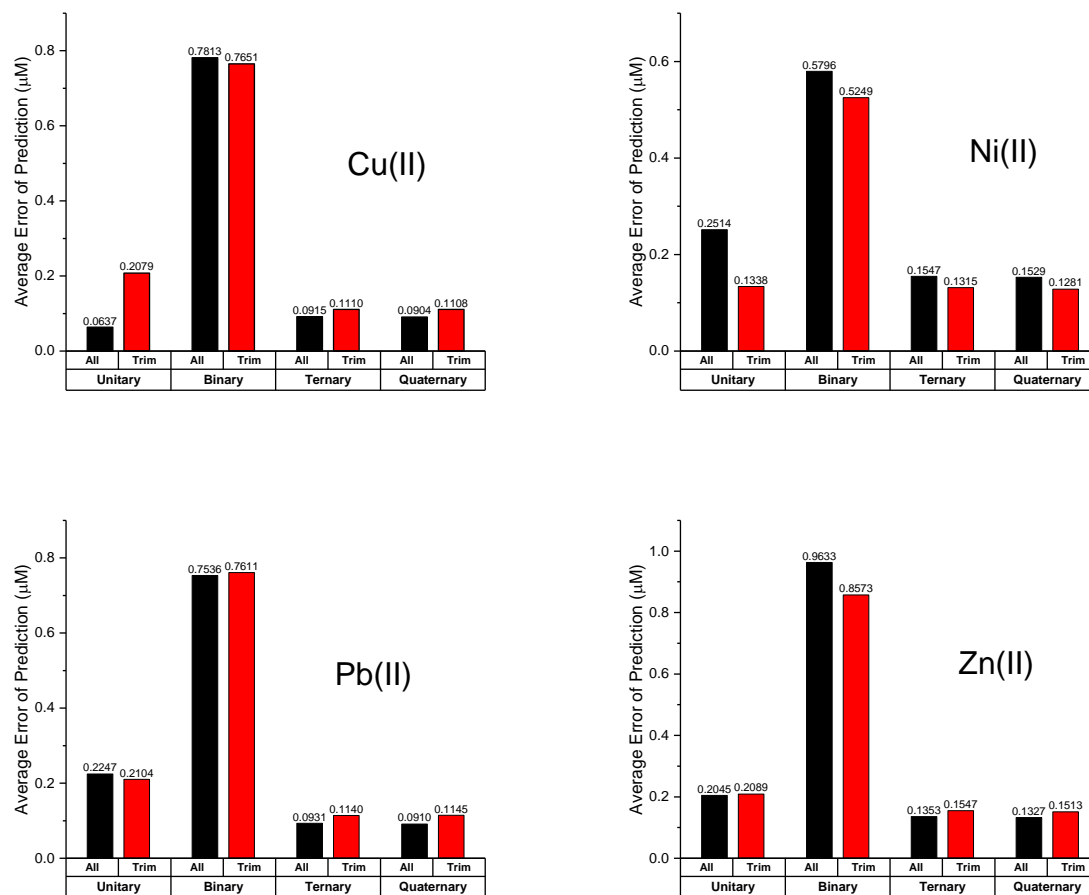
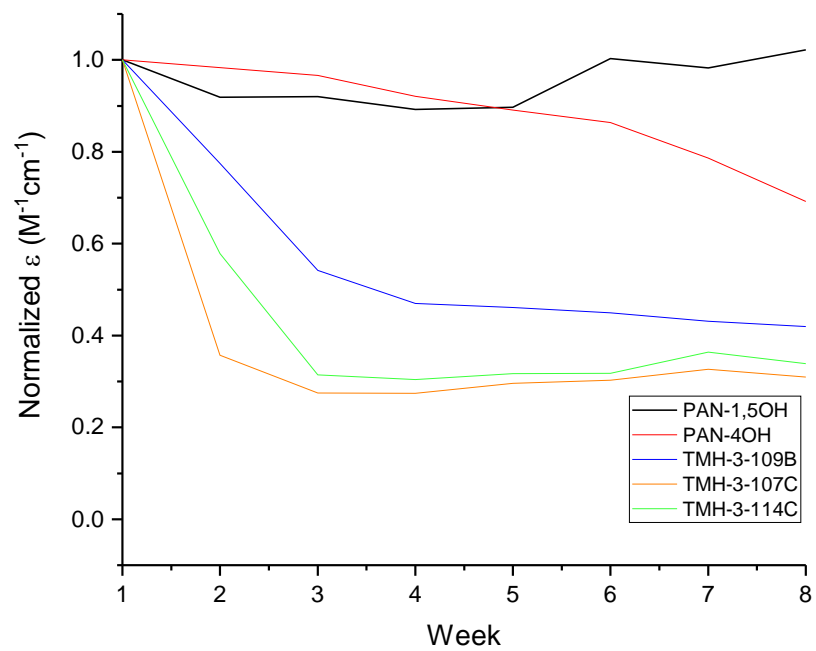
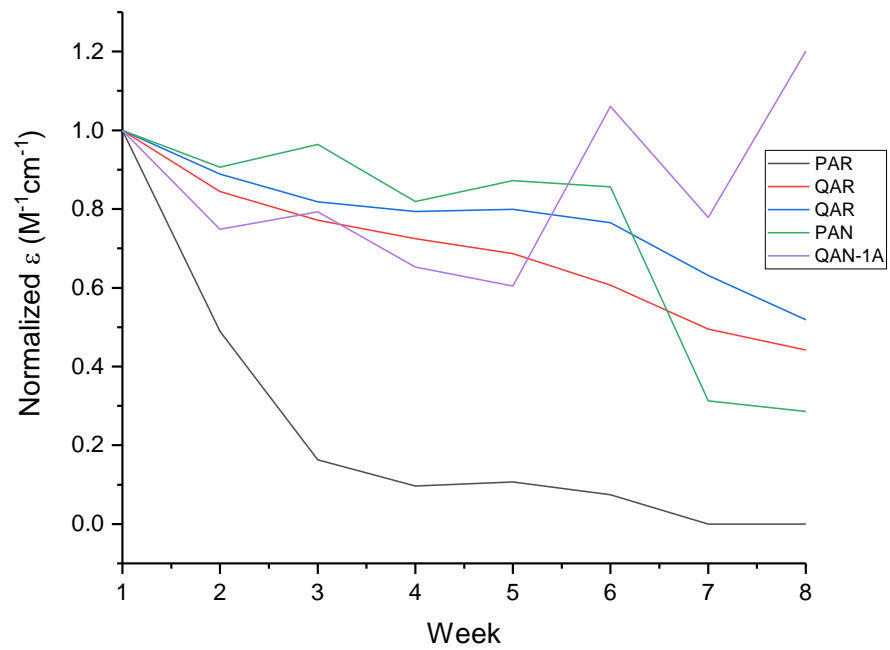


Figure 36: The comparison between types of PLS models show that binary had the highest error in all cases. The complete model (black) and the trimmed (red) model from the VIP data show similar errors in all cases.



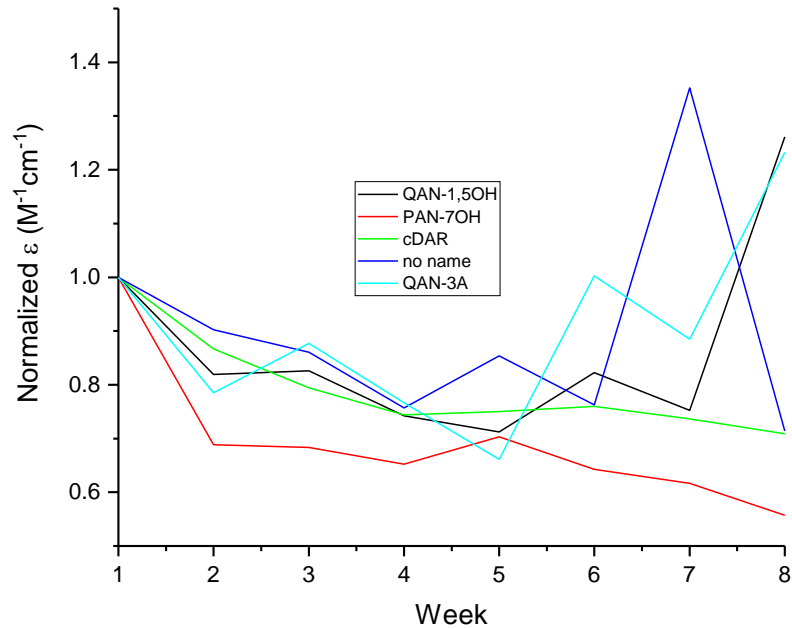
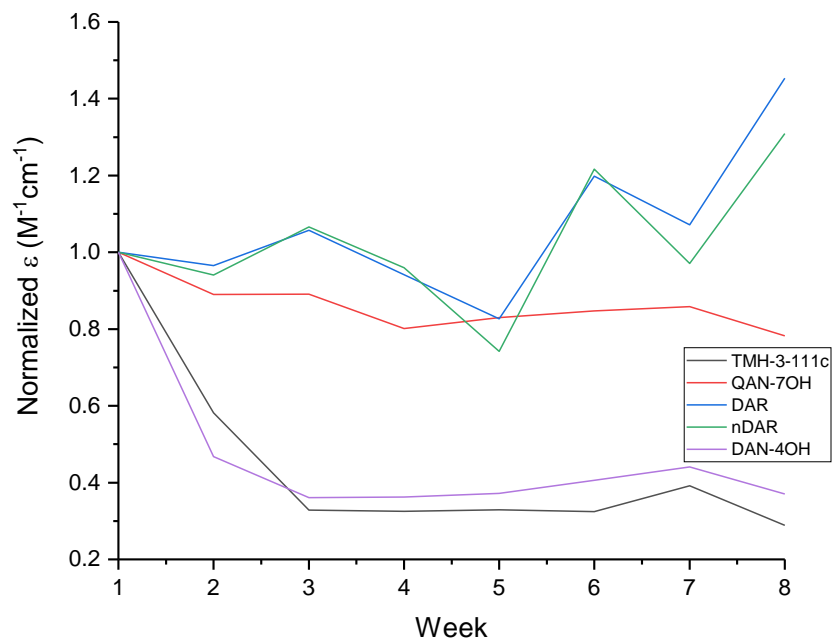


Figure 37: Longevity studies done of several chemosensors. The molar absorptivity coefficient was normalized to the first week of measurements.

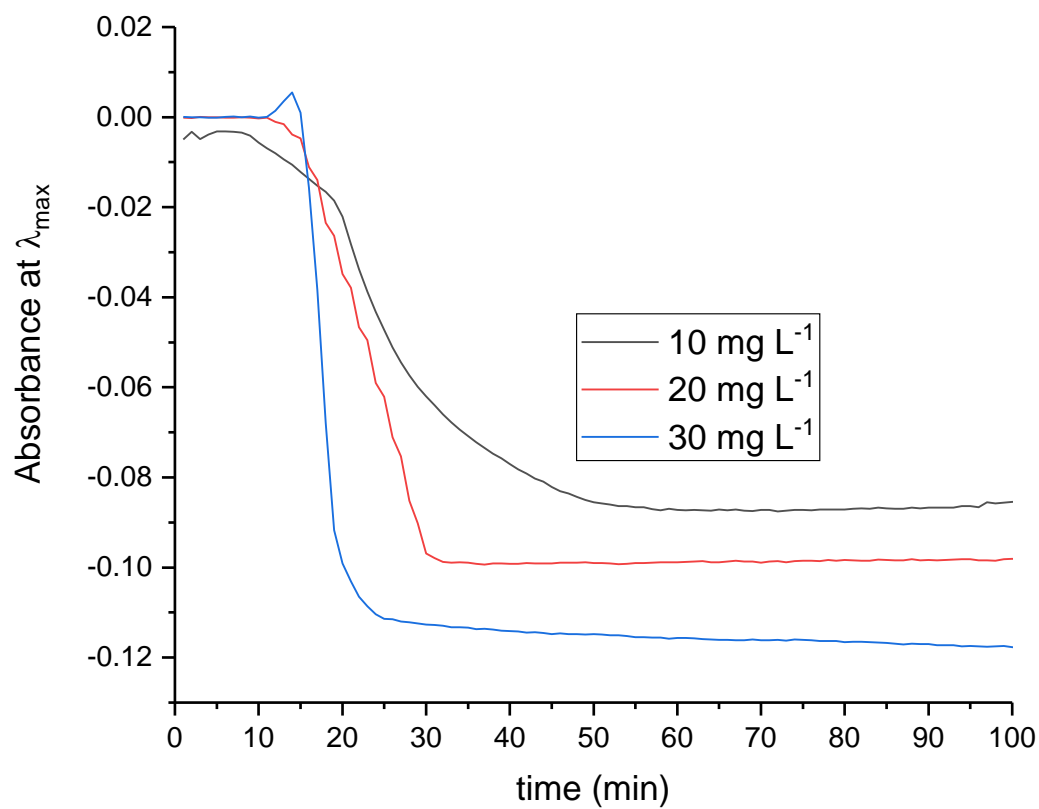


Figure 38: Response of the PAR film to three different Zn concentrations (10 to 30 mg L⁻¹). The negative absorbance appears because the buffer concentration (0.01 M) was too low and the acidic AA standard neutralized the dye.

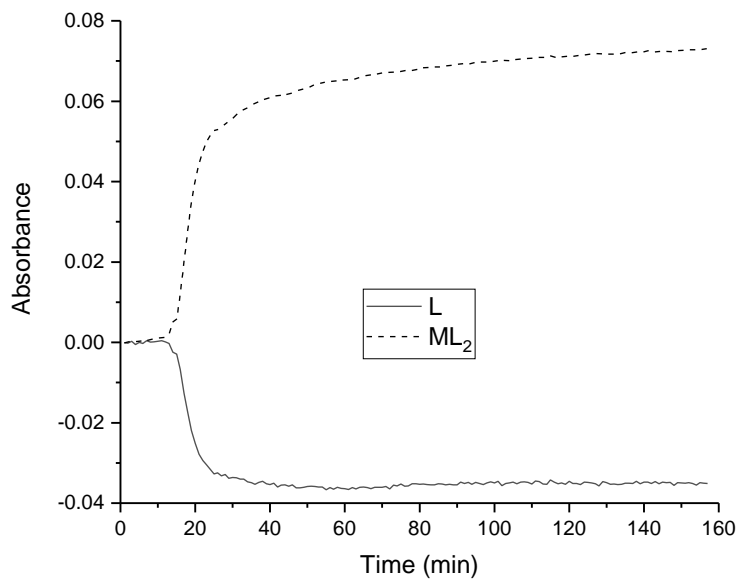
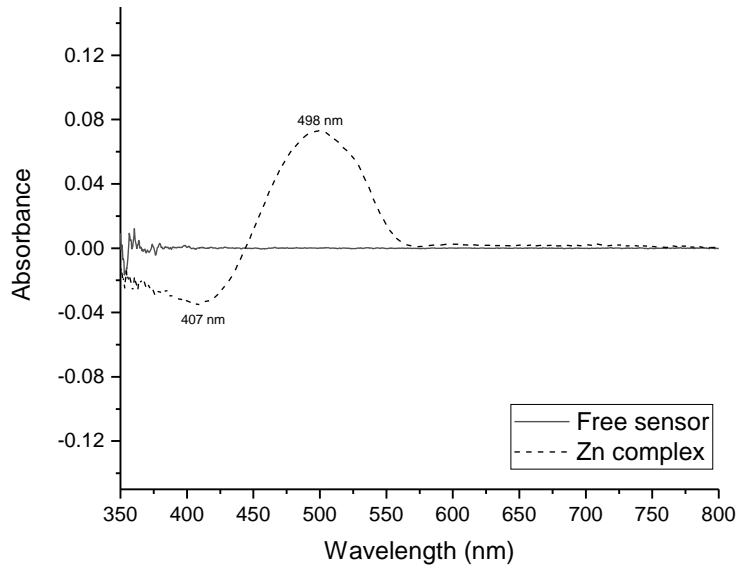


Figure 39: Typical response of films to $5 \text{ mg L}^{-1}\text{Zn}$ when proper MOPS concentration was used. The spectral response (top) shows a negative peak for the free dye and a positive peak for the metal complex. The growth of these peaks can be monitored over time (bottom).

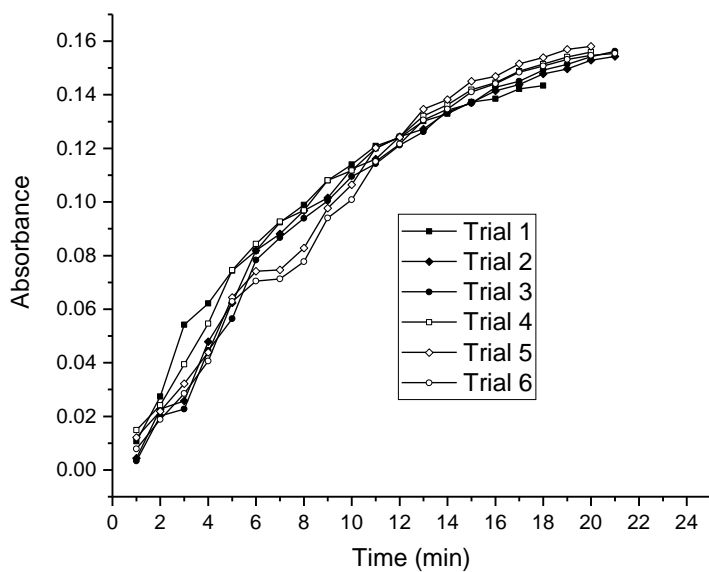
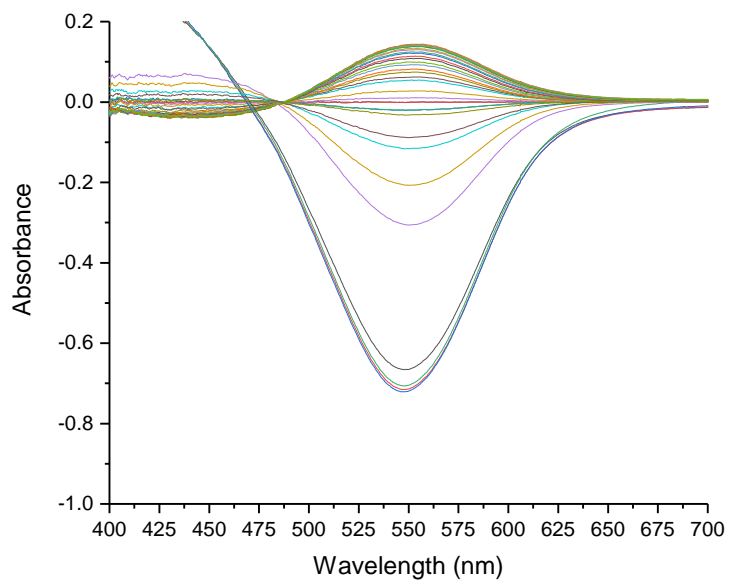


Figure 40: Repeatability of an OAN film to 1 mg L^{-1} Zn. The response (top) is negative when rinsed with acid and then positive when metal is binding. The average RSD for all data points was 1.54% (bottom).

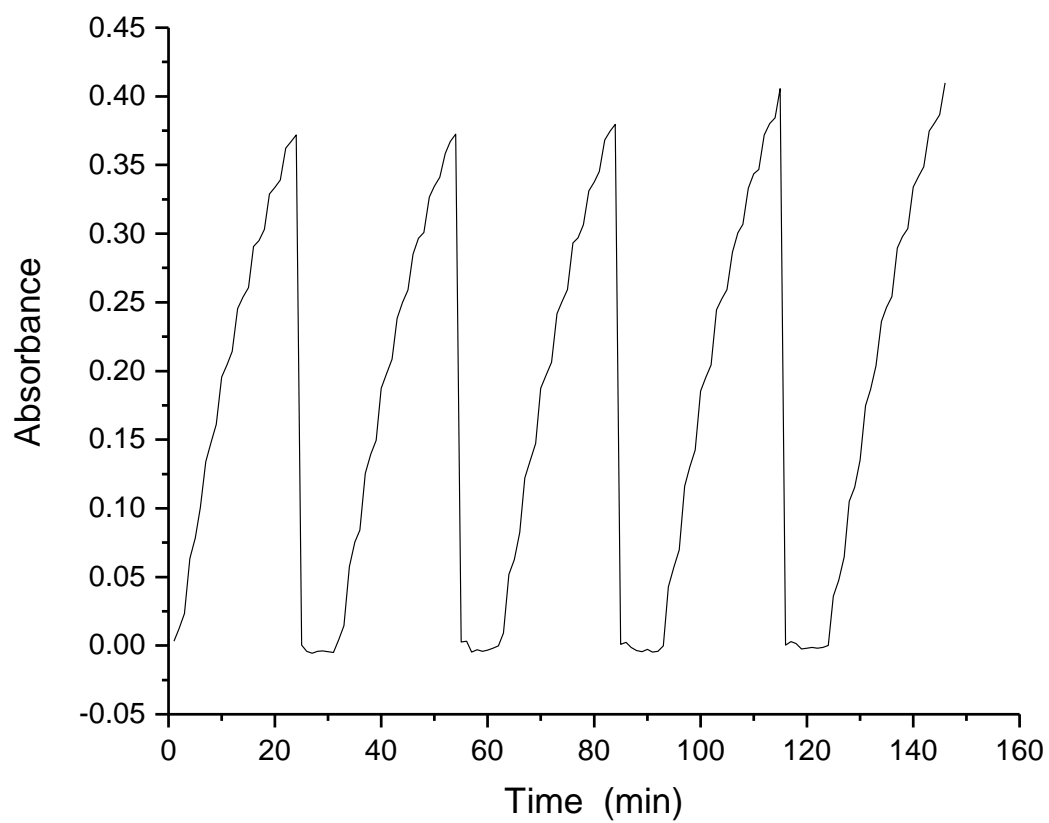


Figure 41: Several trials of the PAR film response to 10.9 mg L⁻¹ Zn are shown as concatenated data. The return to baseline with acid wash is quick (1-2 min).

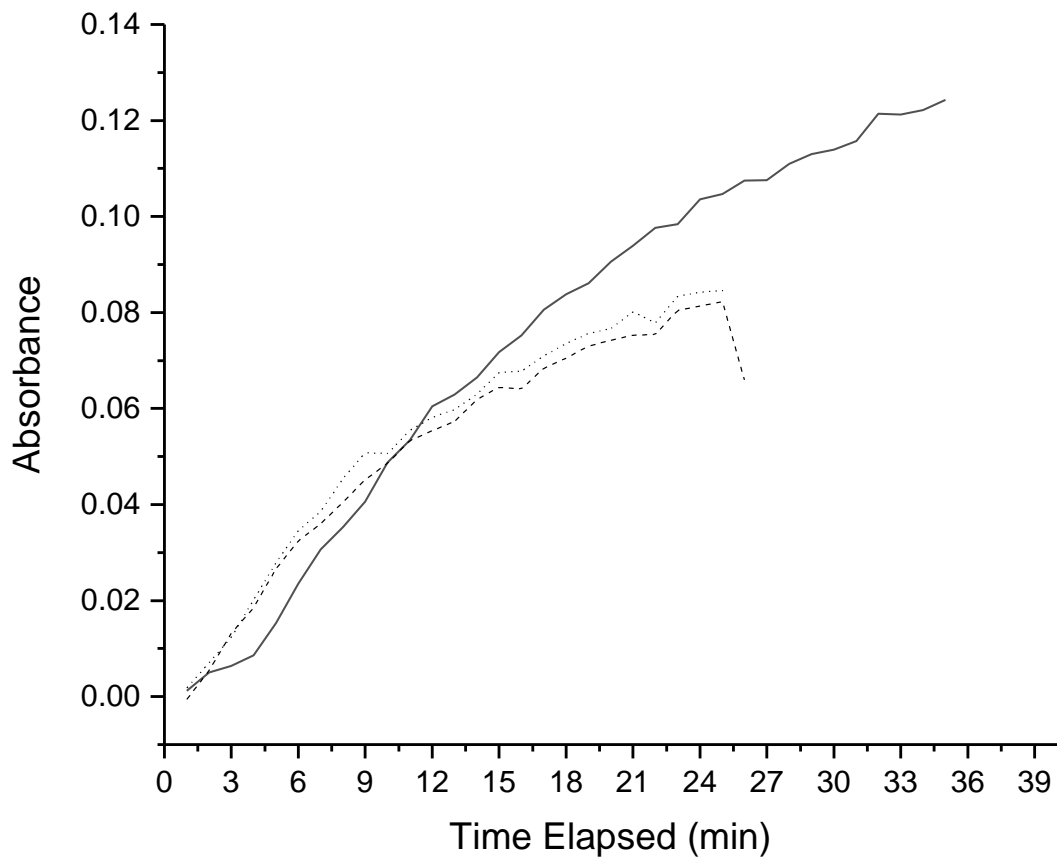


Figure 42: PAR film response to 1 mg L^{-1} Ni. One run (solid line) was done for a longer period to see if saturation could be reached.

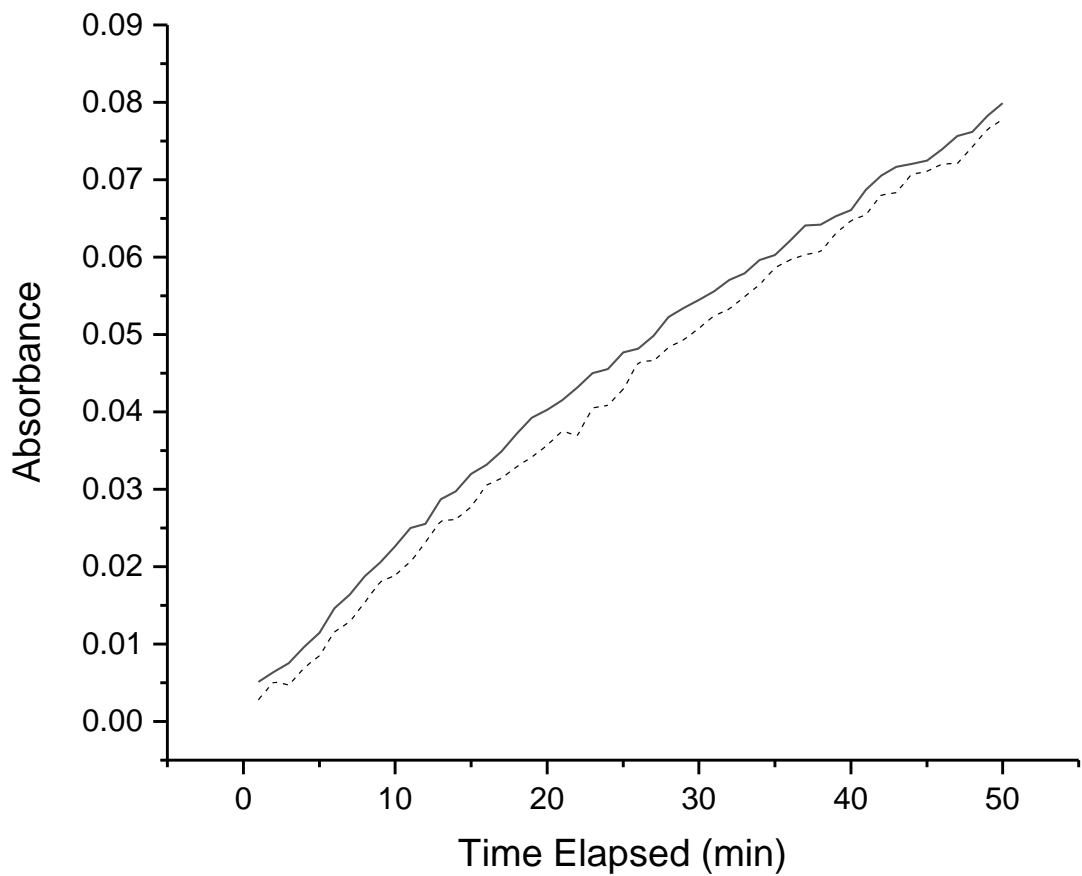


Figure 43: Response of PAR film to 100 mg L⁻¹ Zn. Longer runs were done to see if saturation could be reached.

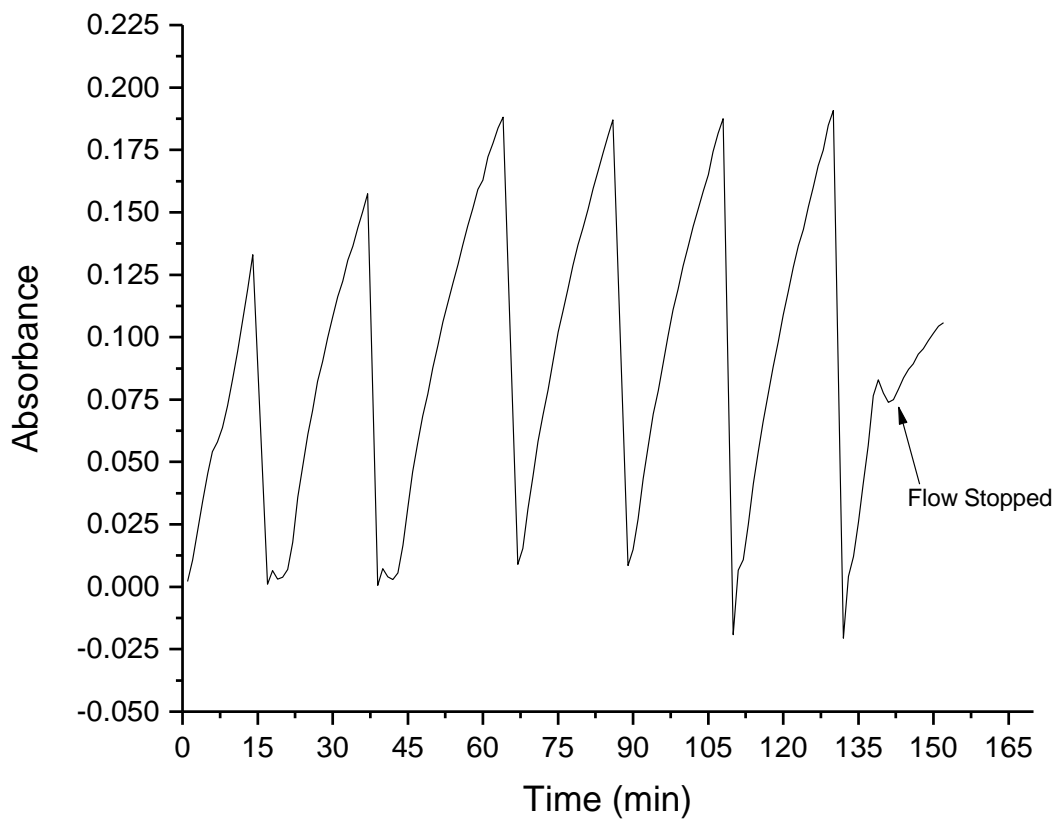


Figure 44: Response of PAR film (519 nm) to 1 mg L⁻¹ Zn at varying flow rates. The first two trials were at 4.72 mL min⁻¹ and the final five at 10.6 mL min⁻¹. The last trial was stopped to examine stopped flow conditions.

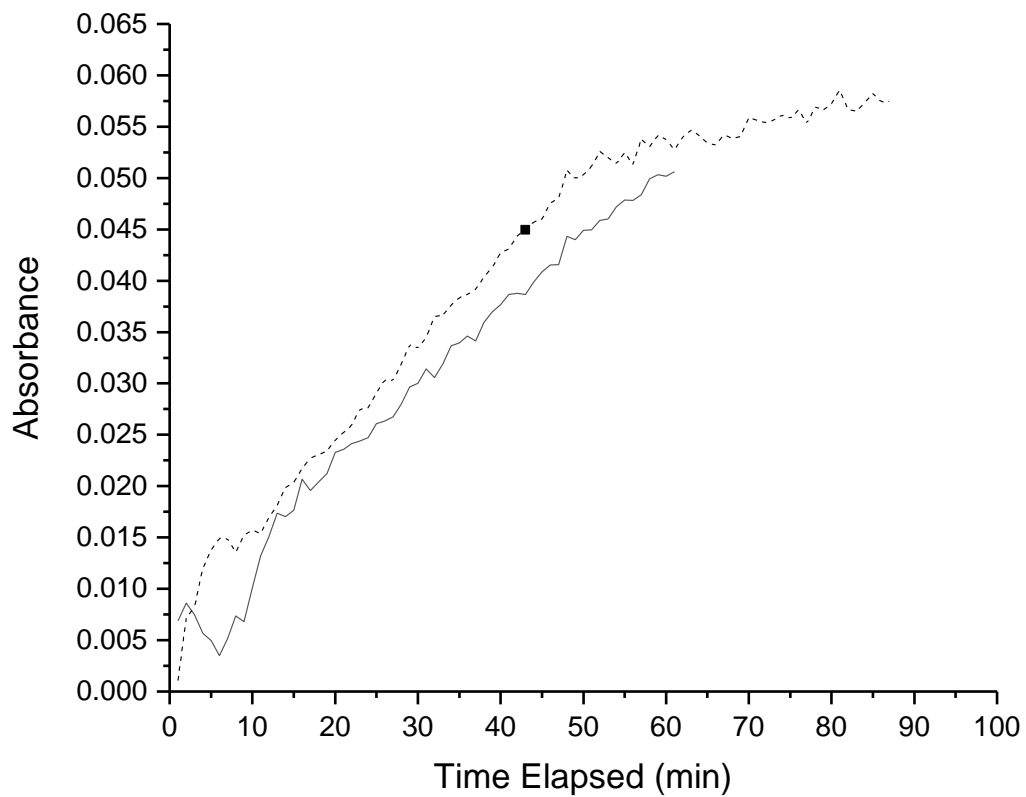


Figure 45: Stopped flow response (516 nm) of a PAR film to $100 \mu\text{g L}^{-1}$ Zn. The solid line is continuous flow and the dashed line has flow stopped at the point marked.

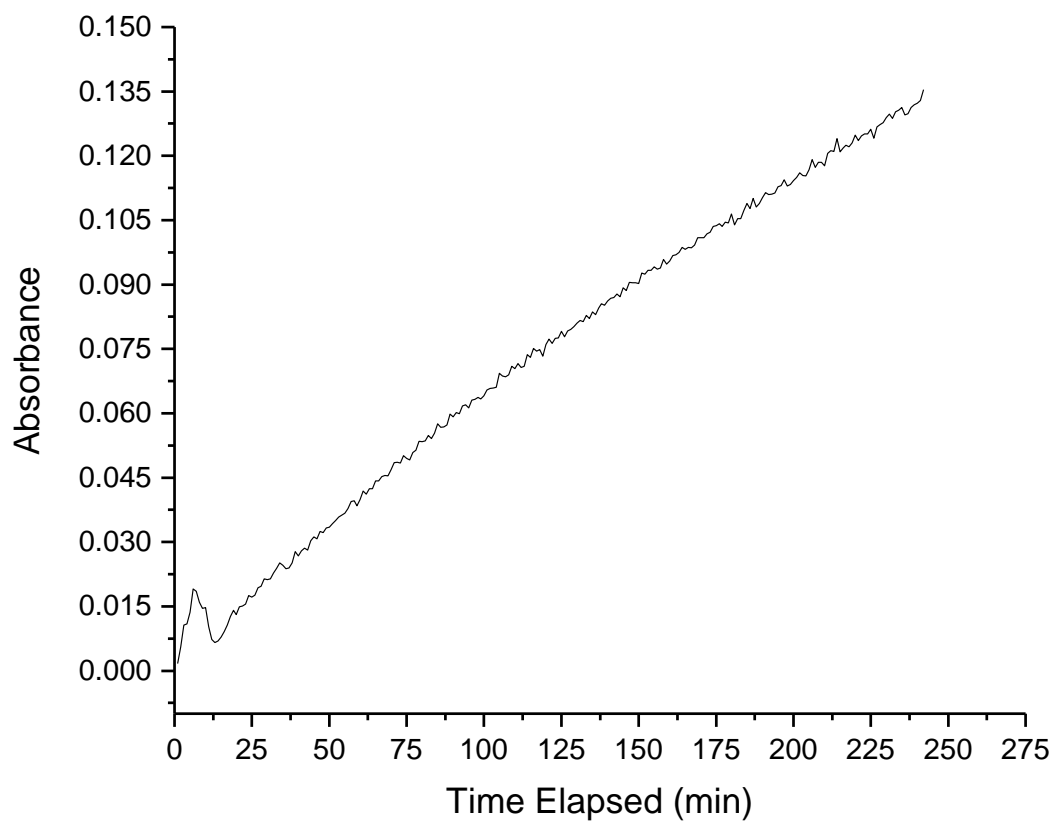


Figure 46: Attempting to reach saturation for a cationic PAR film (516 nm) with $100 \mu\text{g L}^{-1}$ Zn. Saturation was not reached, even after 250 minutes.

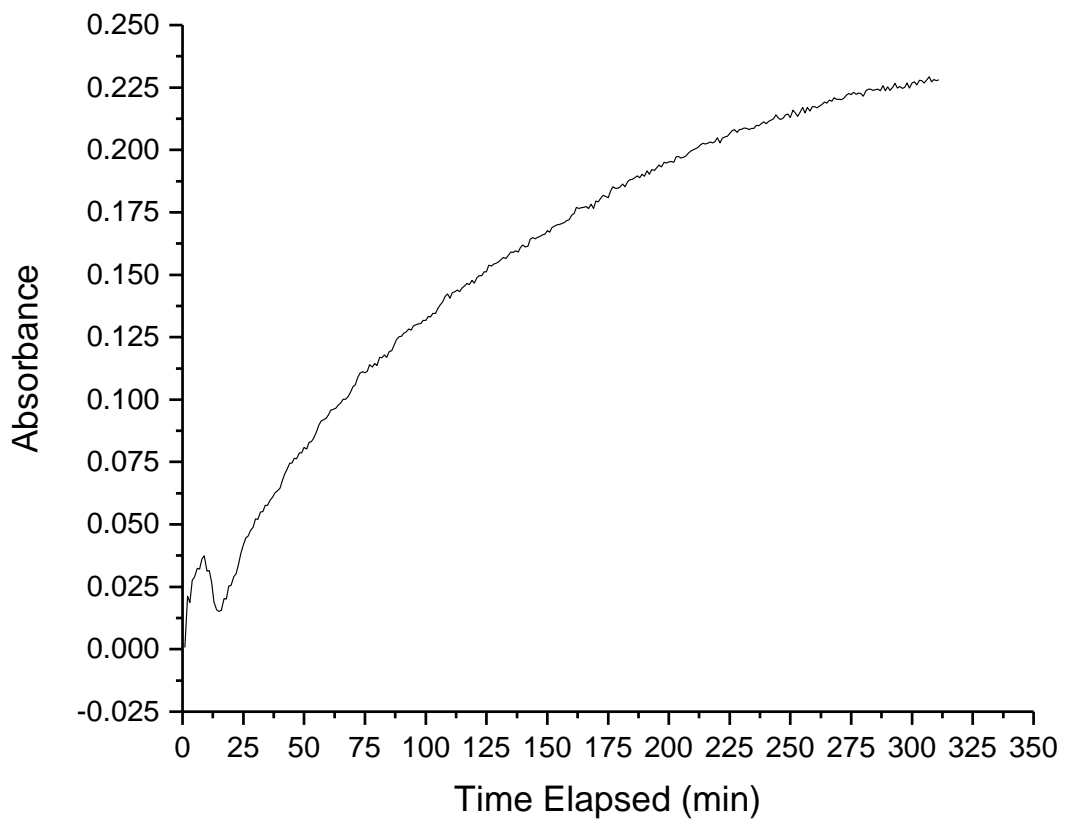


Figure 47: Response of a PAR film to 1 mg L⁻¹ Cu. The response (512 nm) was monitored over time.

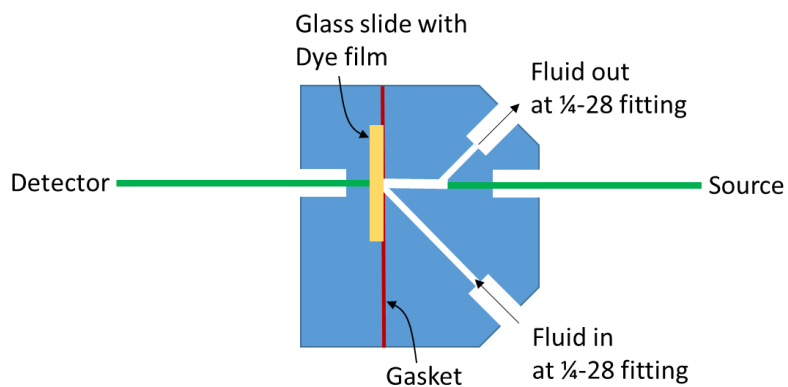
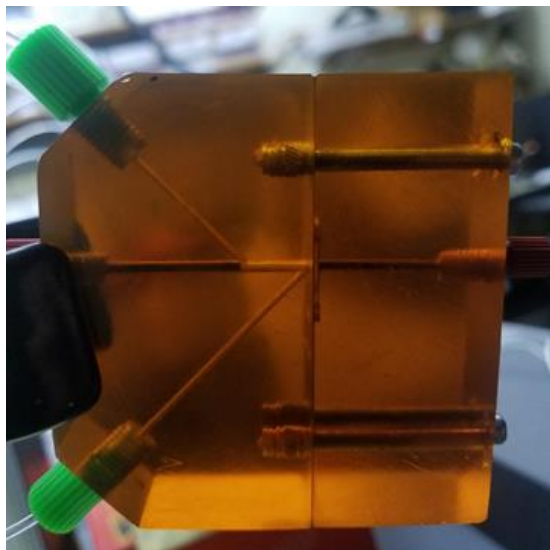


Figure 48: Photograph of the SIA flow cell design. The flow cell is a Z-design but has a cutout that allows a slide with the chemosensor to be inserted (courtesy of G. Marshall).

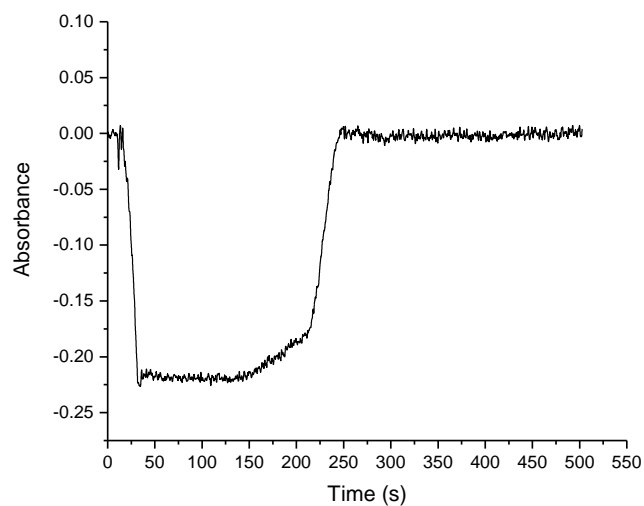


Figure 49: Initial response (500 nm) to the acid wash cycle (0.1 M HCl) when using large volumes of acid and buffer to wash and equilibrate the film, the Absorbance is initially negative when being washed by acid and then returns to zero when equilibrated with buffer.

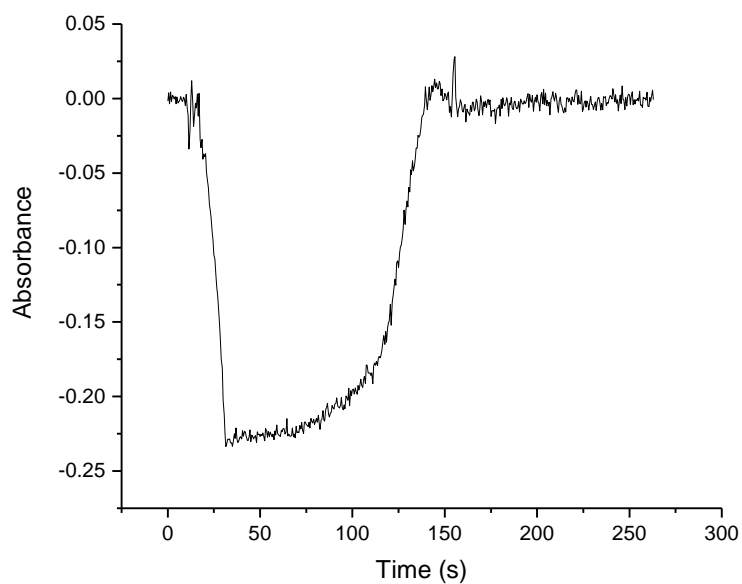


Figure 50: The adjusted response (500 nm) when using appropriate volumes of acid (0.1 M HCl) and buffer (0.1M MOPS) to wash and equilibrate the film.

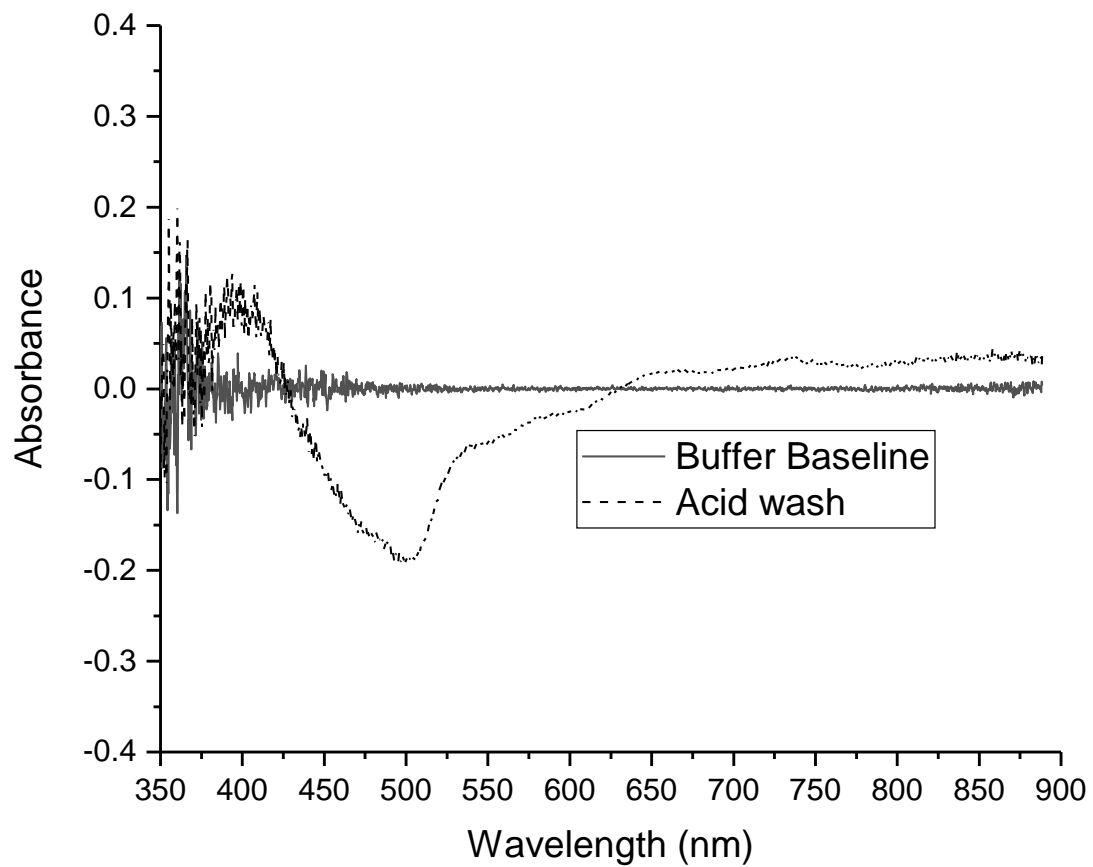


Figure 51: Typical response for a QAR film to $100 \text{ mg L}^{-1} \text{ Zn}$. The negative peak occurs when the buffer is neutralized by acid.

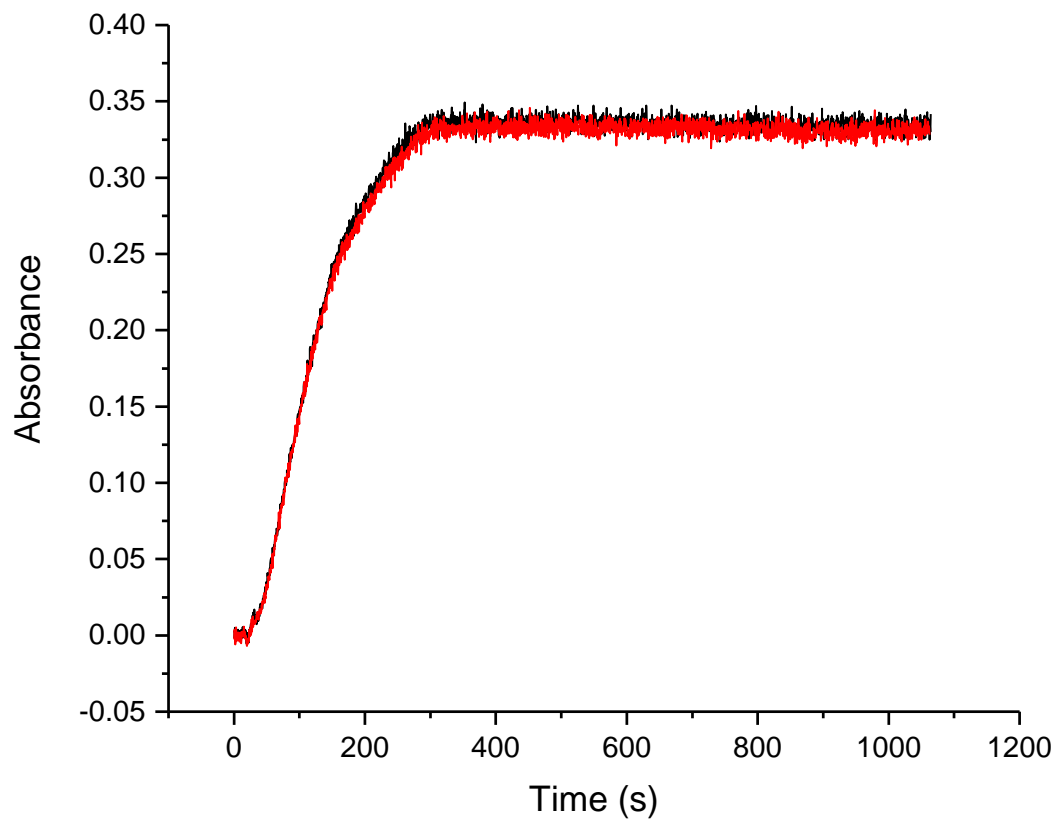


Figure 52: Repeatability of PAR film for two trials of $3.3 \text{ mg L}^{-1} \text{ Zn}$ with an RSD of 2.07%.

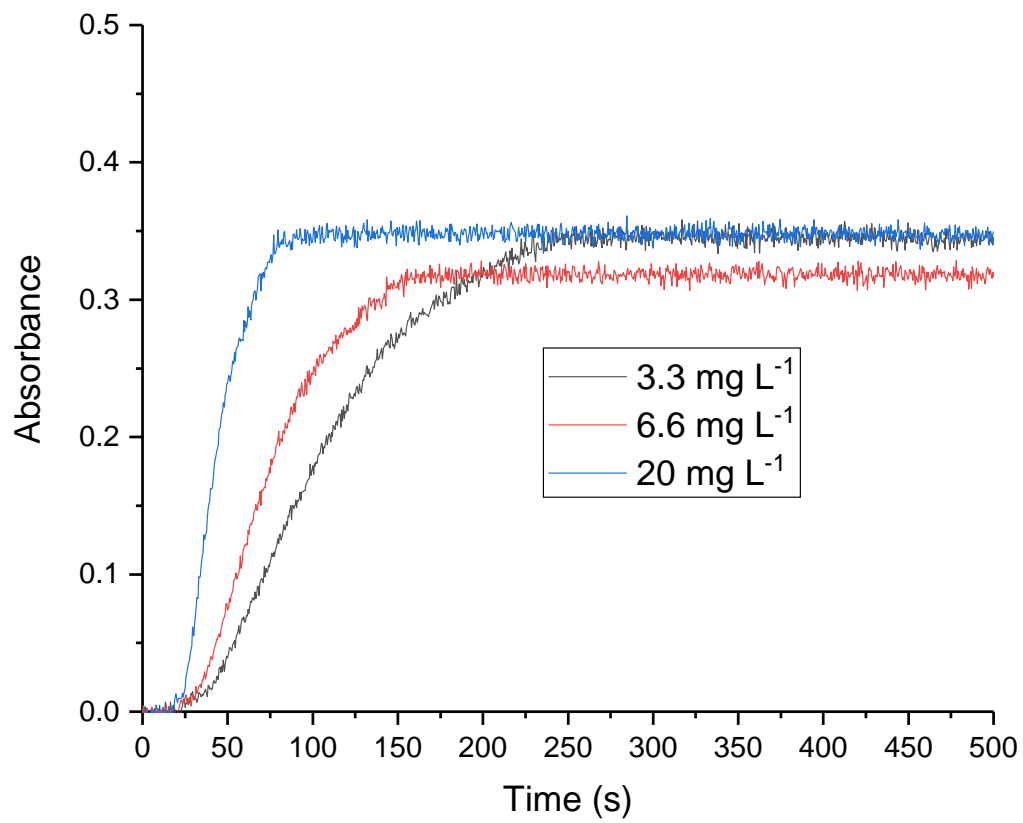


Figure 53: Response of PAR to increasing Zn concentrations. Saturation is reached in all cases.

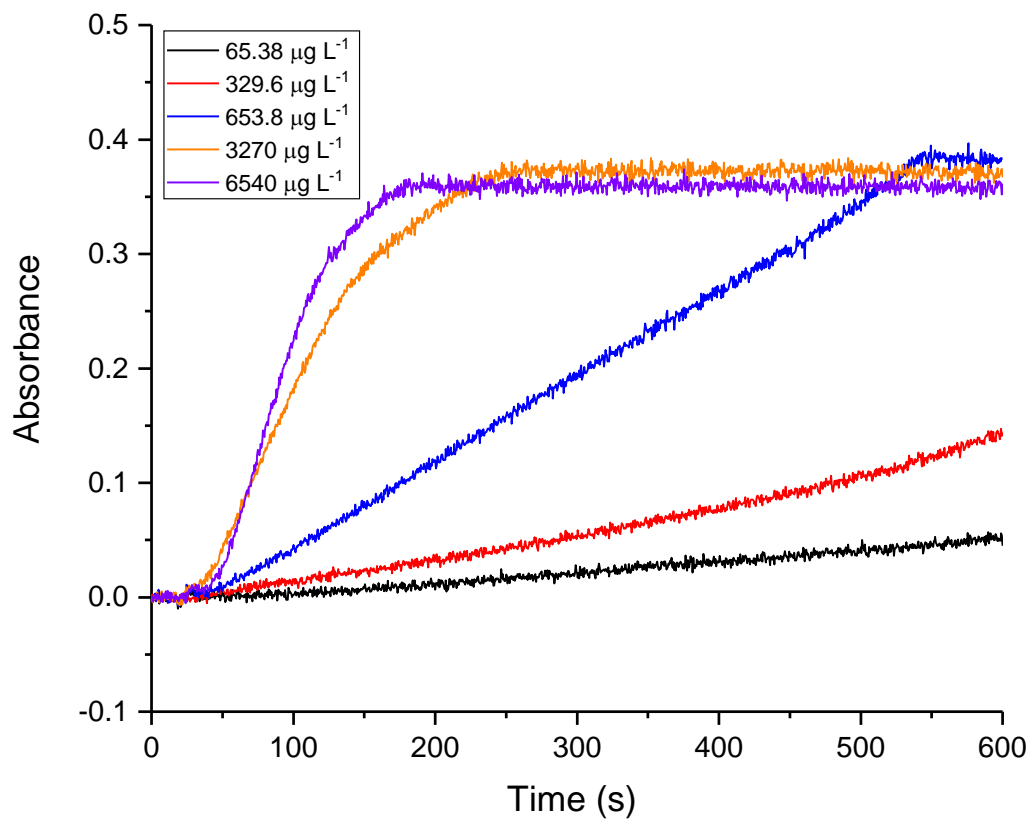


Figure 54: Response (525 nm) of a PAR film to increasing Zn concentrations. At 100 μM , saturation is reached within ~ 150 s.

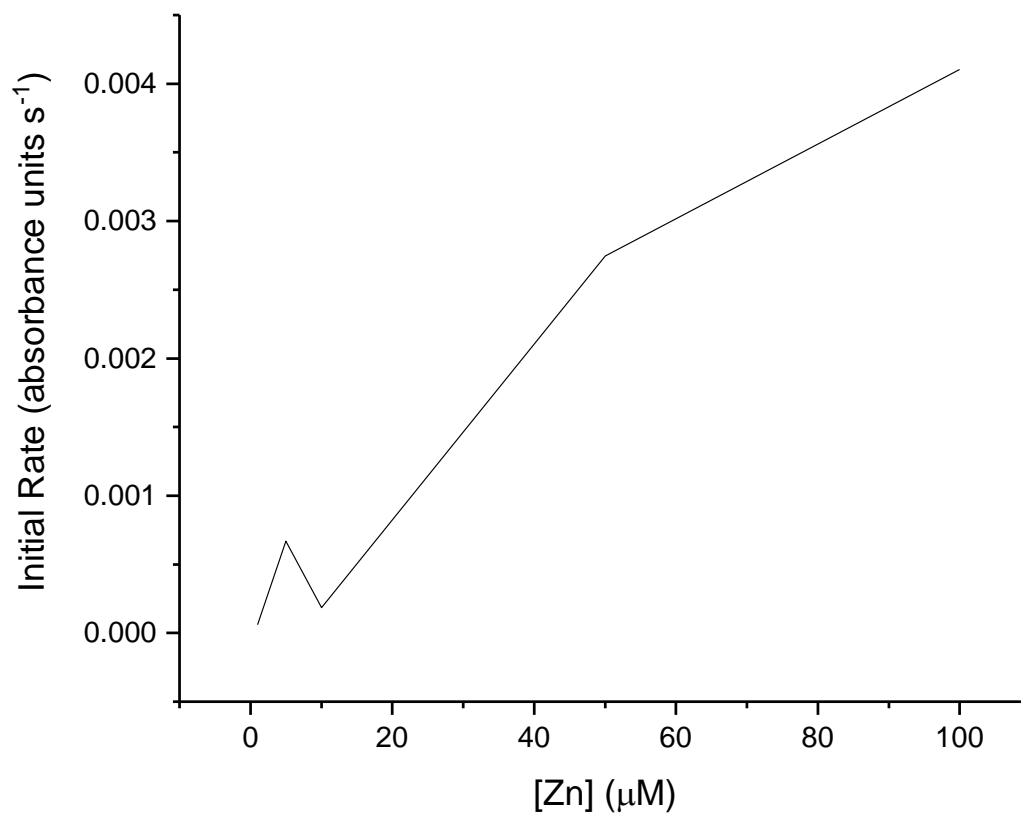
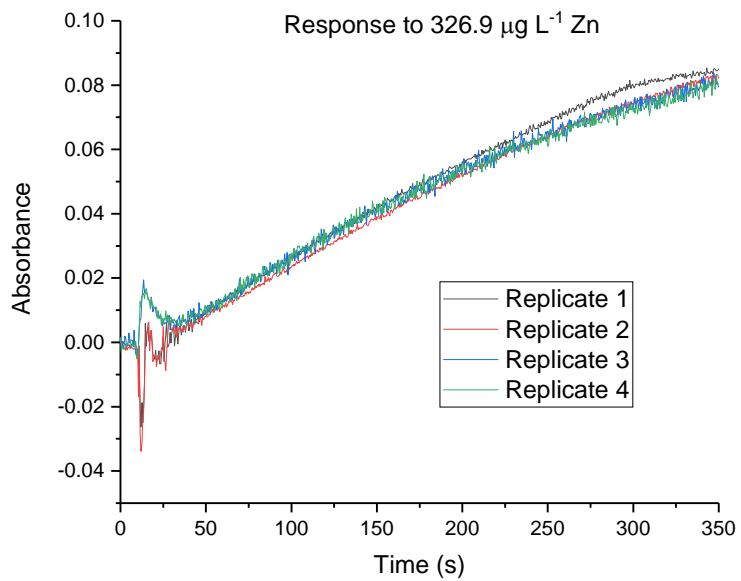
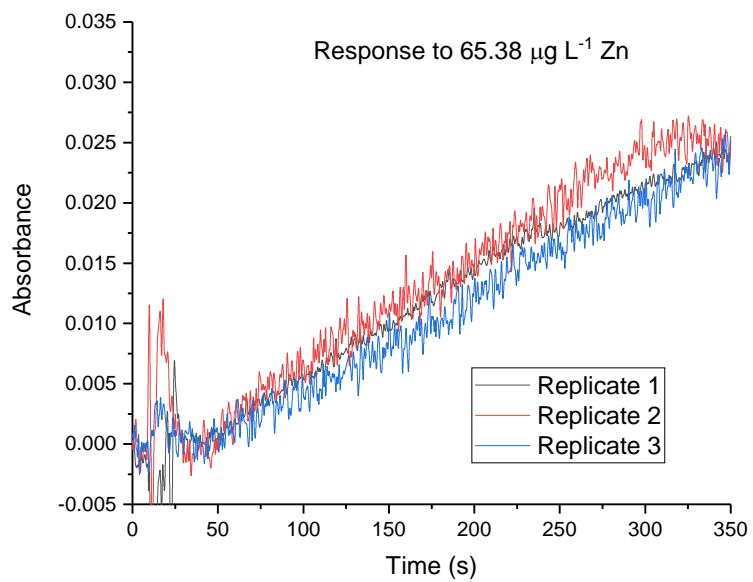
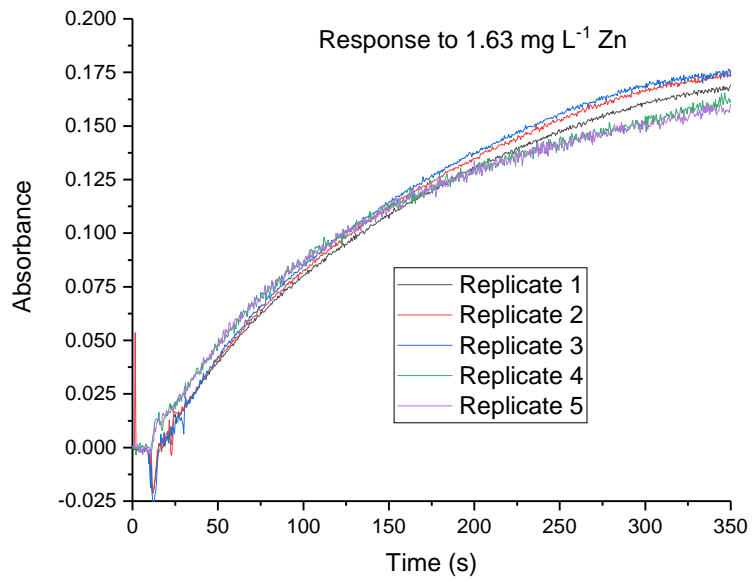
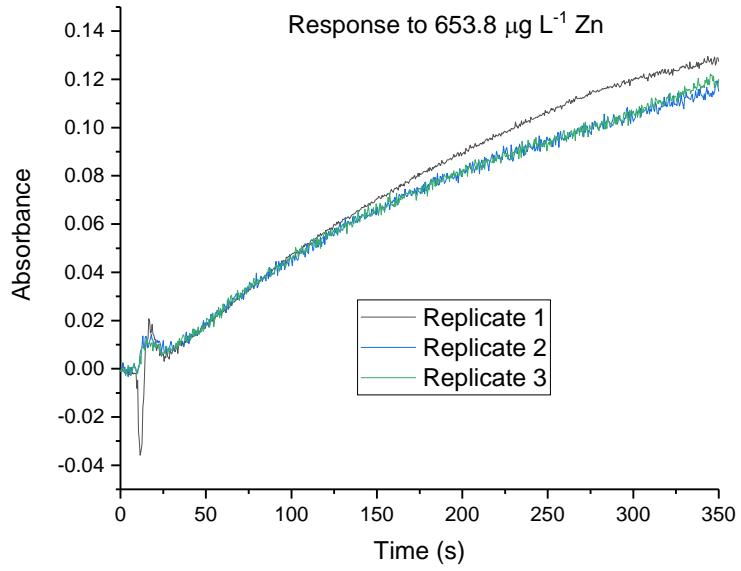
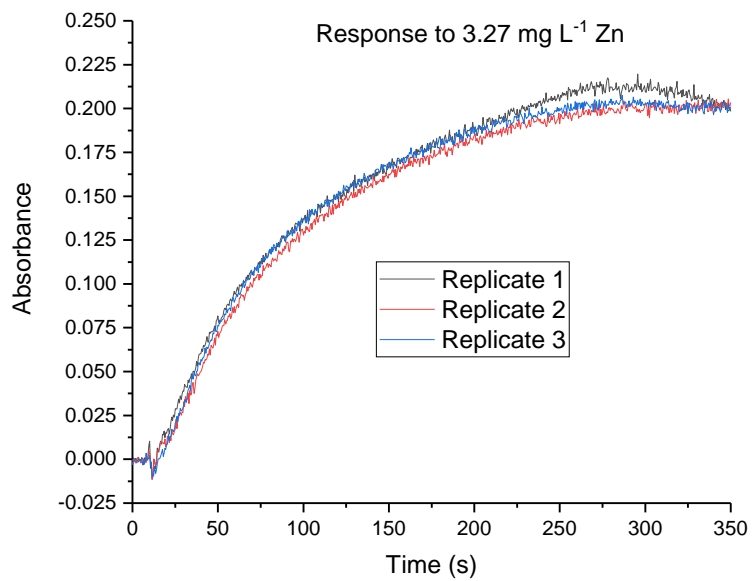
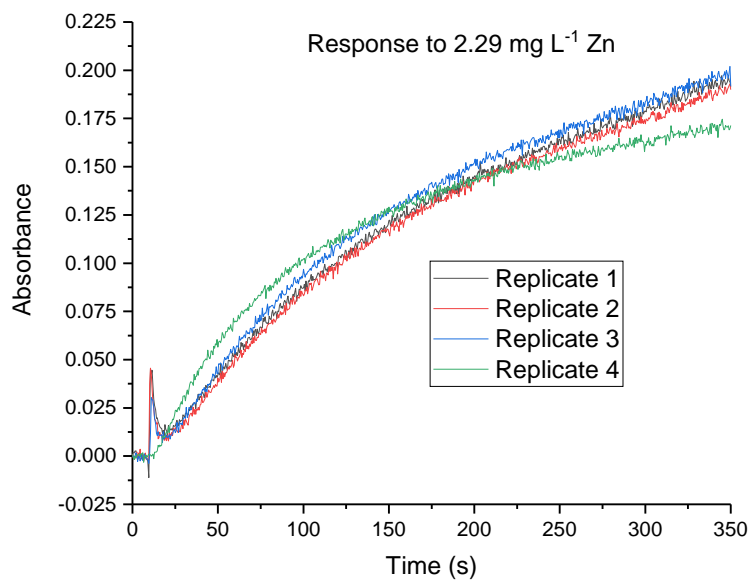


Figure 55: Comparison of the initial rate of accumulation of Zn on a PAR film. The slope from 60-100 seconds (while the metal was accumulating) was used as a measure of the rate.







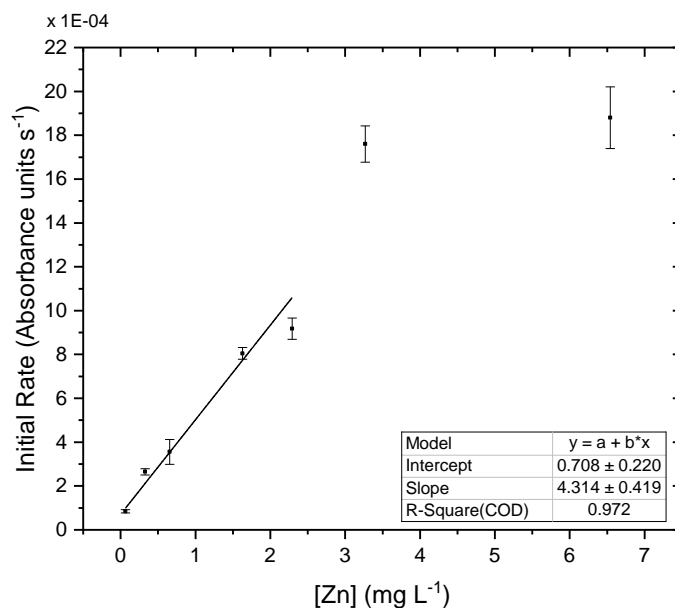
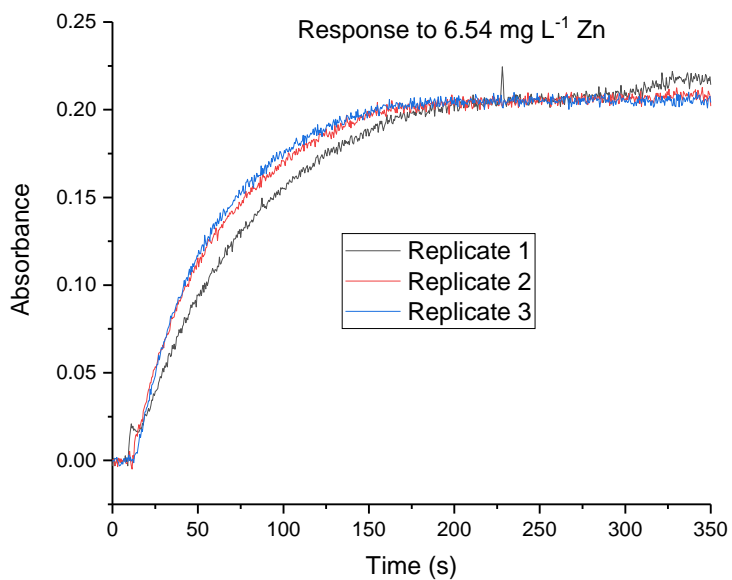
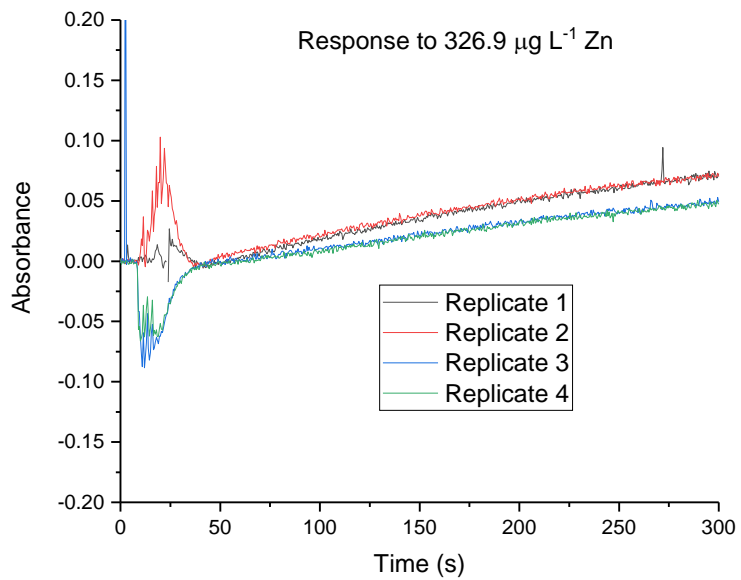
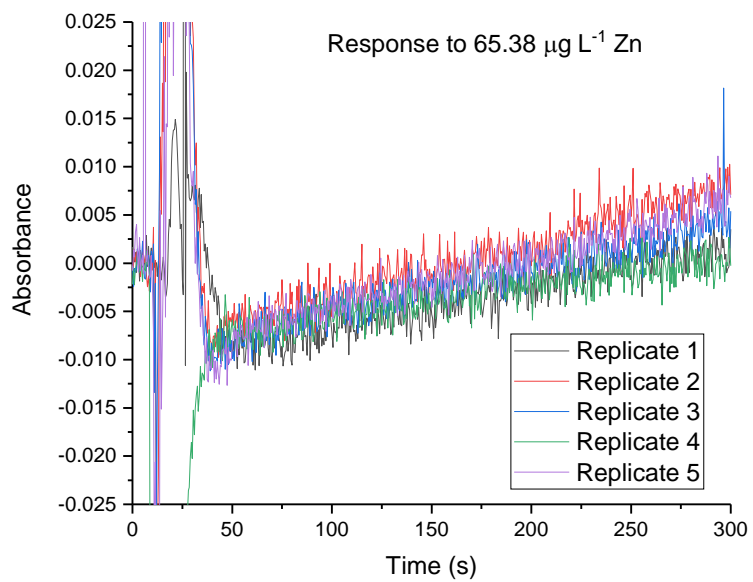


Figure 56: Response (525 nm) of a PAR film to increasing Zn concentrations at pH 7.0. The 95% confidence interval was used for error bars. The response of this film is linear at lower [Zn] (<3 mg L⁻¹) with a R² of 0.97 for a linear fit. At higher concentrations (>3 mg L⁻¹) the R² increases to 0.94.



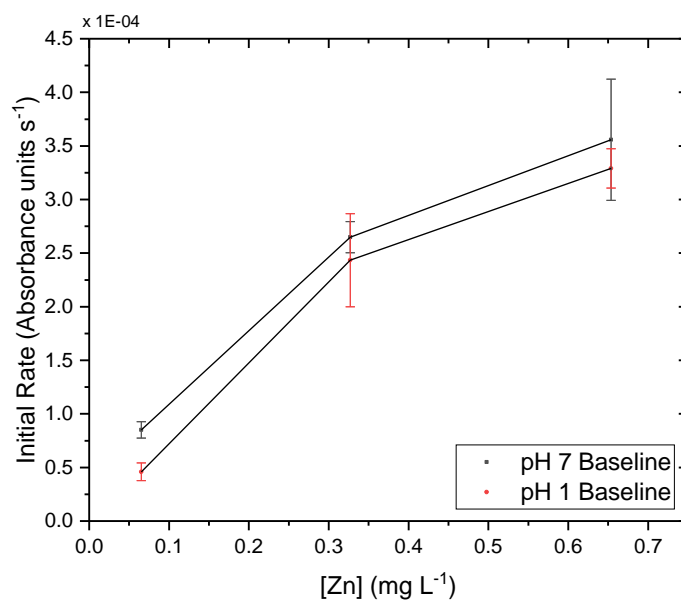
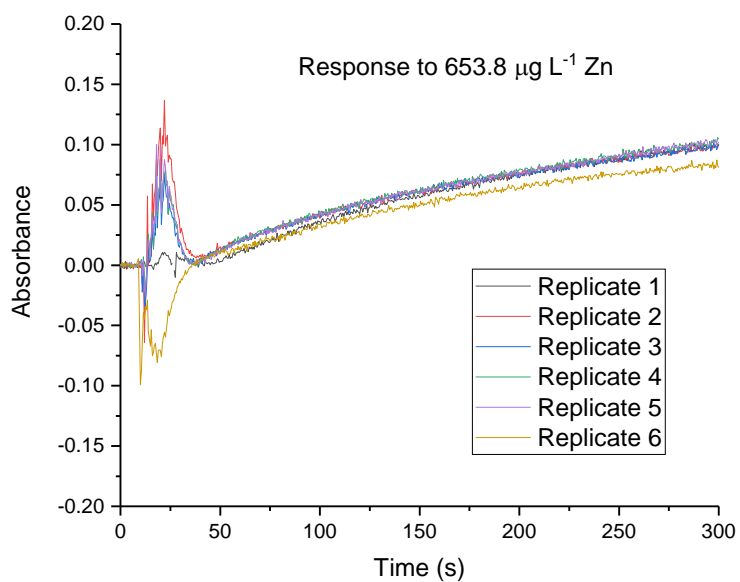


Figure 57: Response (525 nm) of PAR film to a baseline obtained using acid (0.1 M HCl) then buffered (pH 7.0). The baseline was taken in acidic and buffered (pH 7.0) conditions.

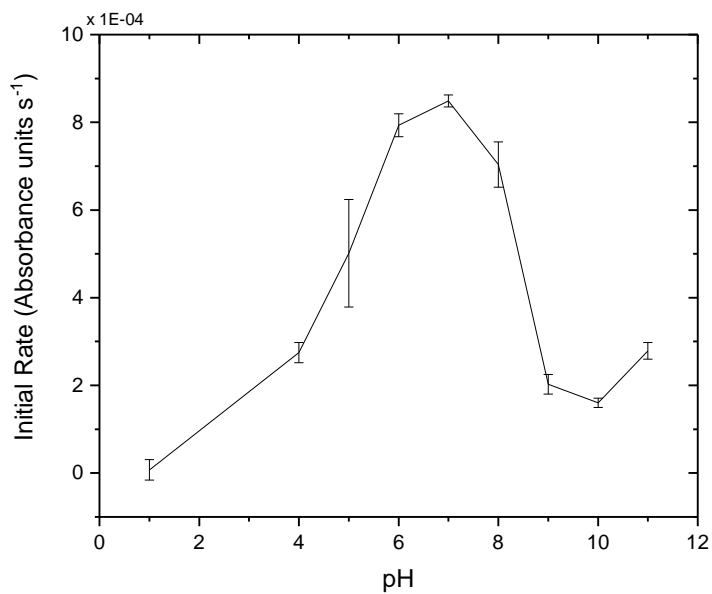
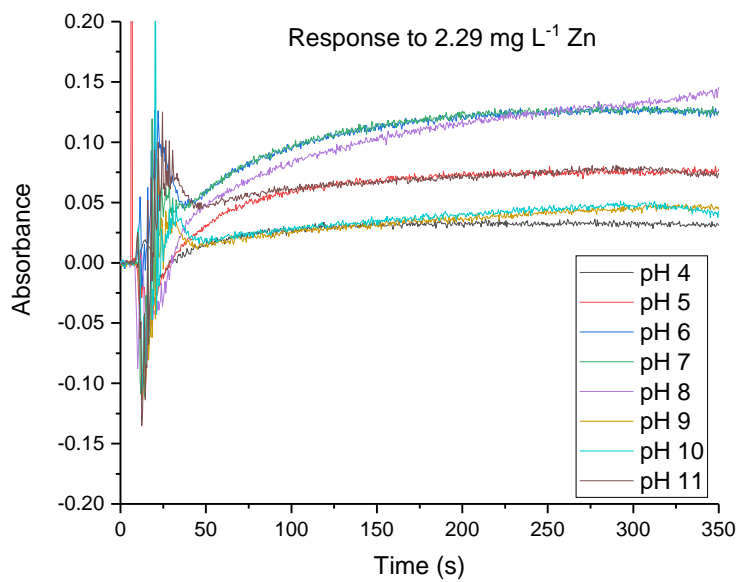


Figure 58: Effect of pH on binding rate. The best binding occurs near neutral pH because there is little competition.

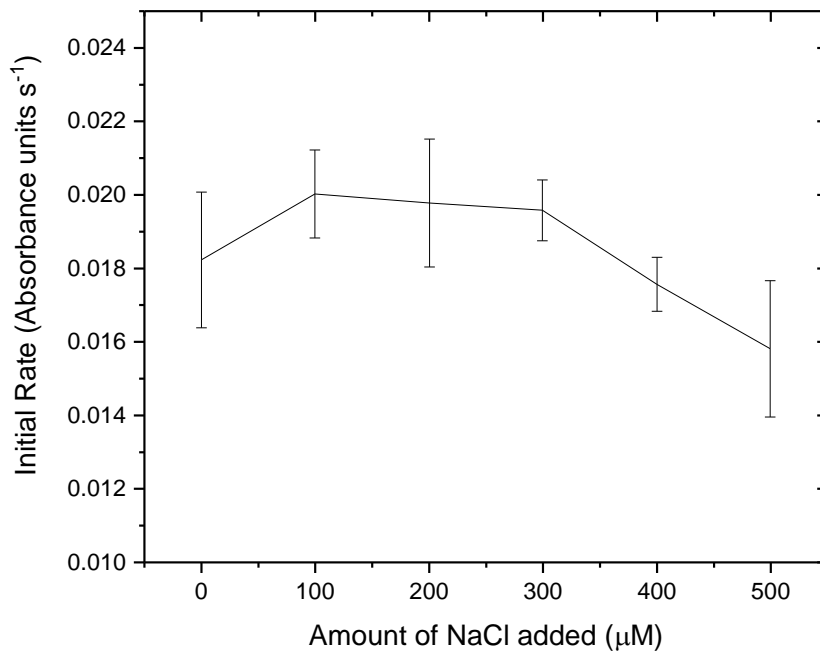
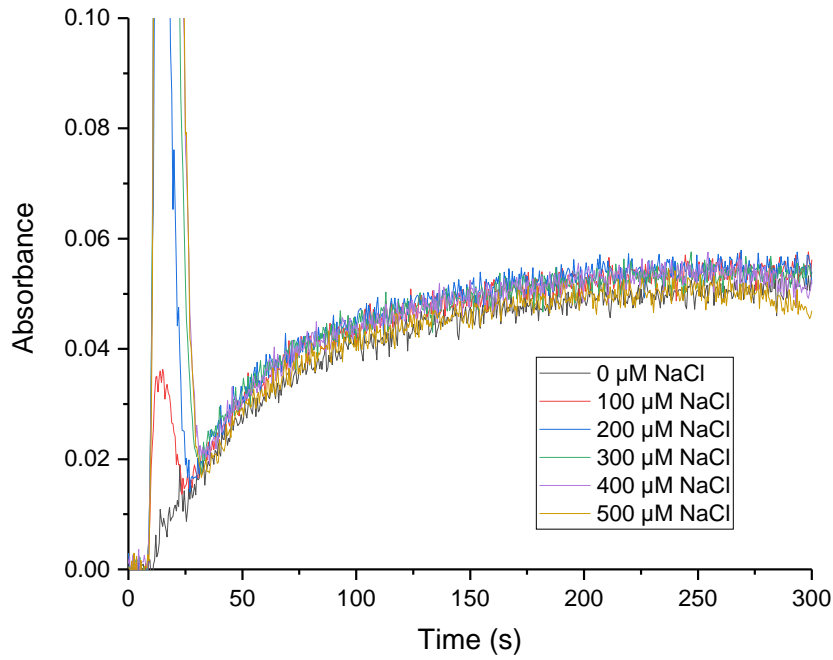
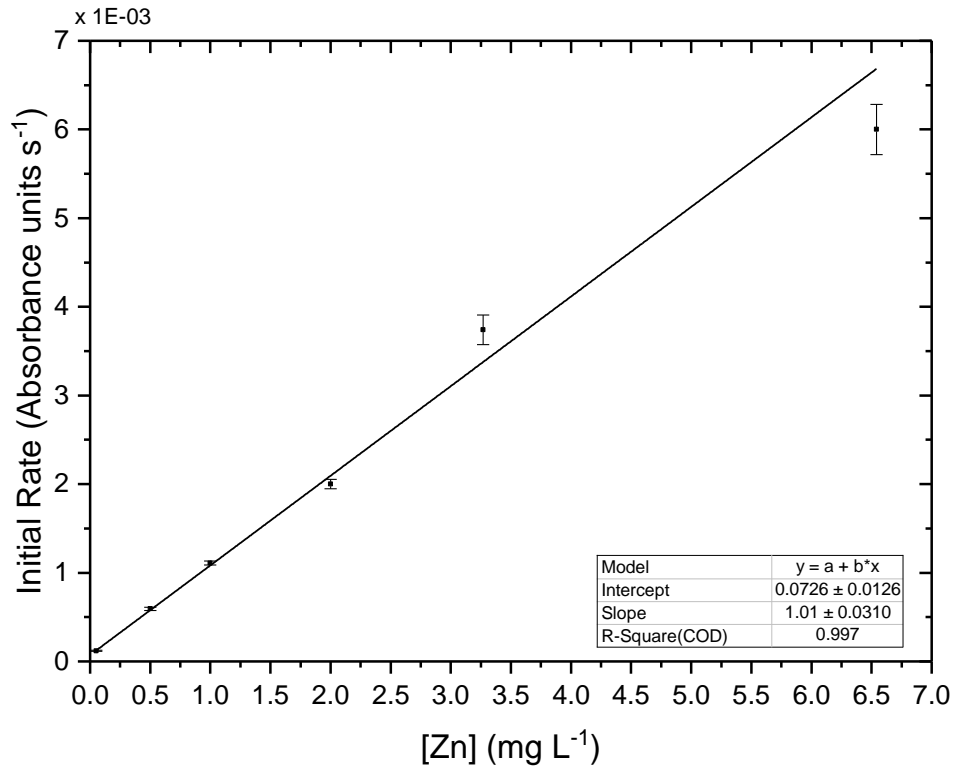
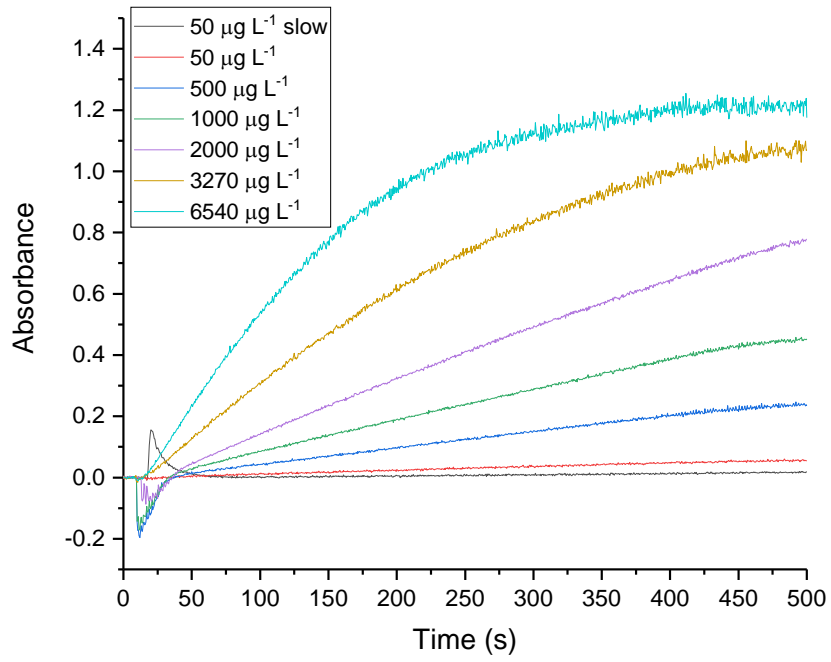


Figure 59: Effect of ionic strength on binding rate ($2.29 \text{ mg L}^{-1} \text{ Zn}$). The ionic strength of the metal sample was varied by adding NaCl ($n=4$).



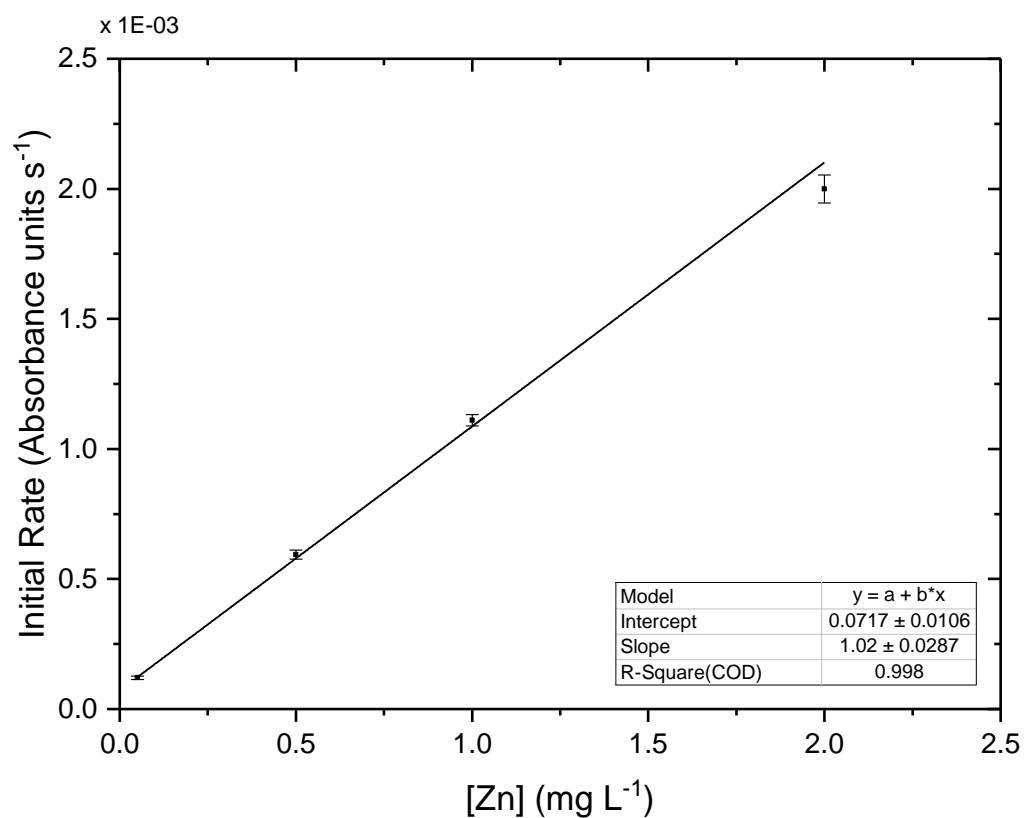


Figure 60: Effect of metal concentration of binding rate. The response rate (525 nm) increases with increasing [Zn]. The initial slope was calculated to find the response rates. The linear behavior is shown in the full and cropped concentration range with an R^2 of 0.997 and 0.998 respectively.

Chapter 4: Conclusion

This work brings attention to the need for continuous, real-time heavy metal quantitation. Heavy metals are dangerous to humans and the environment and heavily regulated. Some heavy metals are essentially to the human body in small quantities (e.g., Zn) while some can be toxic (e.g., Pb). There is a lack of an affordable, real-time method for reliably measuring heavy metal concentrations in process streams. Some very accurate, portable AAS and ICP-MS devices exist but they are far too expensive and complex for most applications. The need for a better approach becomes apparent when considering the alternative of daily overtreatment to ensure that regulatory limits were not exceeded. The cost of wasted time and resources can be recuperated if a better method is developed.

A spectrophotometric method for monitoring heavy metals in water can be a simpler, more cost-effective solution to this problem. Complete characterization of the chemosensors is crucial in understanding how the quantitation method will be applied. In this work, it was shown that an azo dye can be characterized via titrimetric methods using multivariate modelling to compute acid dissociation constants and binding affinities. Error propagation can be used to give a good estimate of the error on these values. A library of dyes was tested for metal response to 16 analytes and a table was made for comparisons. This can be useful in determining possible complimentary dyes for quantifying multiple analytes. When choosing a dye, it is important to not only consider the metal analyte but also what interferences might be encountered. Several dyes were identified as solvatochromic and QAN-1,5OH was tested and found to exhibit both positive and negative solvatochromism. Positive solvatochromism is seen with less polar solvents toluene ($\lambda_{\max}=492$) and chloroform ($\lambda_{\max}=476$) compared to more polar solvents acetonitrile ($\lambda_{\max}=563$) and DMF ($\lambda_{\max}=579.5$) but negative solvatochromism is seen with isopropanol ($\lambda_{\max}=520$) compared to

triethylamine ($\lambda_{\max}=495$). MOPS was a good buffer choice for most metals, but it did form complexes and aggregate with a few causing the scattering of light. It was found that several other buffers could be used such as phosphate, tris, or EPPS if scattering is seen in the samples. The three pK_a values of an azo dye (PAN-7OH) were determined to be 2.70, 9.07, and 12.14 ± 0.24 using spectrophotometric titrations and the modeling software REACTLAB. These pK_a values are useful in identifying what species will be present at the pH of interest. The low and high pH values tend to cripple the dyes ability to bind metals with competing processes occurring. The middle pK_a disappears upon dye attachment to a film resulting in a singular dominant species between pH 2.70 and 12.14. This species is capable to binding the metal readily as the azo nitrogen is deprotonated. The pK_a values for all metal complexes (Cu, Ni, Zn, Pb, Cd, Co) were determined in a similar titrimetric and modelling method. These values showed the usable region of the chemosensor to be between pH ~5-10 depending on the metal analyte. At low pH the protonated form is favored and at high pH, metal hydroxides readily form rather than the complex. The binding ratios and affinities were found for each metal in the order $Cu < Co < Zn < Ni < Cd < Pb$ with the 1:1 complex favored for Pb due to the large size. The K_D values ranged from 632 nM to 18 μ M. Cd and Pb bind one and two orders of magnitude weaker respectively than other metals tested. The PLS approach used to quantify multiple metals in solution with two chemosensors was successfully in accurately predicting Cu, Ni, Zn, and Pb simultaneously in pseudo unknown samples with errors under 0.5 μ M in most cases. Additionally, mean prediction errors of less than 0.4 μ M and standard deviation of less than 0.14 were seen in replicate measurements. Analysis of the composition of the model showed that some correlation may have been unintentionally included when making the samples. The model handled the data quite well and even cutting out extraneous information such as the flat baseline did not dramatically improve the results. Overall, the number of samples in the training

set is an important consideration when building the model. It is possible that with more/different chemosensor, the model could be built with a smaller set of training data.

Using these chemosensors in a process application requires the dyes to be incorporated into a solid support. The dyes were covalently attached to a glass slide via a hydrogel polymer attachment. The glass slides were then glued into a cartridge to be put into the flow cell. These films were tested in several different flow system setups that fell under the categories of conventional and microscale (SIA). The conventional (large-scale) system was tested for metal response, repeatability, and flow rate. The intensity and speed of the response of the films used in this system were dependent on metal concentration and were very repeatable with RSD values below 5%. The flow rate was also an important consideration. Faster flow lead to more effective diffusion and a faster response while stopping the flow slowed the response as analyte was depleted from the flow cell. Typical responses were around $0.009 \text{ abs min}^{-1}$ for 1 ppm Zn. Cu and Ni also showed good responses to the PAR films tested but had near identical responses to Zn which highlights the need for intuitive modelling or selective dyes. A flow cell was designed to work with the microscale SIA system so that the film could be incorporated. The flow cell was a z-path cell that contained a depression on one side where the film could be secured in the flow and light path. Methods were developed for testing film response to any metal in a high-throughput setup. The SIA flow system was used to test repeatability, baseline concerns, pH effects, ionic strength, and metal concentration. The repeatability of the SIA system was excellent with a RSD below 5%. It was explored whether a baseline on acid was plausible to use in a process monitor to avoid the use of expensive buffers. The acidic baseline was effective but did have a slower response due the films need to equilibrate near neutral pH for metal to bind (i.e., deprotonation of azo nitrogen). This could be explored if cost of buffer became a concern and the response was quick enough that

slowing it down would not harm the utility of the device. The pH was found to affect the binding rate with near neutral (pH 6-8) giving the best response and low and high pH giving little to no response. Any process application would need to find a way around this issue. Most simply, the solution could be brought to neutral pH before measurement. The pH may also be included in modeling to help with accuracy. The ionic strength was another factor thought to be a concern when testing but adding 0-500 μM NaCl showed no effective change in rate of response. The metal concentration effect was tested and for one film, it held linear until 3 ppm ($r^2=0.97$) while another held linear until 7 ppm ($r^2=1.0$) and possibly beyond. The SIA system was exceptional at extensive studies on films and helped determine rate dependencies accurately and precisely (RSD<5%). The conventional system was built as a more robust industrial setup that could withstand a harsh environment and be used as a first prototype for the sensing platform. Overall, the response took longer for the conventional system (min) than the SIA (s). The saturation occurred quicker with the SIA and more periodic acid washing was needed.

Future work on this topic should focus on the two main areas of this work: free dye characterization and flow studies. Further characterization of chemosensors should be performed in order to completely understand which are complimentary. Expanding the number of metals and dyes is the next logical step. With the library of dyes provided, it will be possible to develop a sensor array capable of monitoring multiple metal simultaneously in real-time by studying the important characteristics such as pK_a and binding affinities. Feedback on these values can help in the design of future chemosensors with varied binding affinities and useable pH ranges. It would be advantageous to explore the binding affinity of some of the sensors that bind through more than three atoms. These might bind too strongly and require stronger acids or methods to remove the metal, but they will also be more selective towards certain metals and have lower LODs in a

process monitor. A more thorough investigation of the model and its utility should also be explored. Using more dyes and more metals, testing the exact strength and boundaries of the model could be useful. Further understanding of the film responses will also be crucial in development of a process monitor. Thus far, the film synthesis has gone through several stages with improvements being made on the consistency of films. Testing future film iterations will be a trivial but important task with the methods developed on the SIA device. Determining proper film composition for the process monitor will be determined in part by the design. If using the conventional system, longer response times are favored with fewer acid washes. This would favor films that are slower to respond. The SIA system has faster response times and more frequent, smaller volume acid washes. Field testing will also be an important as the performance of the sensors and flow systems will differ when not in the controlled lab setting. In the field, there are many concerns such as temperature, pH, interferences, matrix composition, etc. Filtering will be a concern as many industrial samples will have particulates that will interfere with the film or even clog the flow system. Perpendicular and tangential filters should be explored to see their effect on the measurement. It is also important to further develop the modeling relative to flow studies. The PLS model has been used effectively in solution but has not extensively been studied in flowing systems. Simple experiments could be done with the SIA to determine what exactly the effects of filtering are and how modeling will be performed. It will also be best suited for testing interferences. The methods that have been developed for metal concentration can be slightly altered and solutions with multiple metals could be introduced. Interferences will vary based on application but could include other metal ions, dissolved solids, phosphates, and dissolved gases. Additionally, there needs to be a way to correlate the results from the SIA to the conventional system if it will be used for prototype testing. Currently, the trends are observable on the SIA but

they are not a direct comparison for the conventional system due to multiple factors in the design of each. A multiplicative or other factor needs to be developed for this comparison if the SIA will be used for extensive testing on films and their response to analytes. Expanding this topic further, there are many other design considerations that could be made. The traditional lamp could be replaced by one or more inexpensive light-emitting diodes (LEDs) and the sensors could be used in an array. This array could contain x number of sensors that respond to y number of metals. The sensors could be multiplexed in a way that while one flow cell is being used for analysis, the others are being acid washed and prepped for their own analysis. It is also feasible that the detector could be replaced by a simple camera that is able to pick up on the pixel differences when analyte is present. Multiple dyes could also be incorporated into the same film assuming that their spectral profiles do not overlap significantly. The application of this work can also be expanded to other analytes such as phosphates and nitrates. A chemosensor for other analytes could be incorporated into a film or solid support much like in this work. These films could then be used in process streams or even environmental applications such as rivers and lakes. The applications of this technology are vast and with the use of robust modeling techniques, instrumentation, and methods there exists a broad market that could be serviced. The SIA system can adapt to whichever application is chosen and is an important analytical tool for method development.

Appendix I. Error Propagation for ReactLab Experiments

- 1) The equation relating pH and pK_a is the Henderson-Hasselbalch equation.

$$pH = pK_a + \log\left(\frac{[B]}{[A]}\right)$$

Where A and B are the acidic and basic (protonated and deprotonated) form of the species

- 2) Rewrite the equation to solve for pK_a and simplify by using $R = \frac{[B]}{[A]}$

$$pK_a = pH - \log(R)$$

- 3) The absorbance at any point in the titration can be written as a sum of the absorbance contribution of each species present. The absorbance of each species is governed by the beer-lambert law

$$Abs_T = Abs_A + Abs_B$$

$$Abs_A = \epsilon_A L[A] \text{ and } Abs_B = \epsilon_B L[B]$$

- 4) Plugging in the individual absorbance equations yields an equation relating the concentration of each species to the total absorbance.

$$Abs_T = \epsilon_A L[A] + \epsilon_B L[B]$$

$$[A] = \frac{Abs_T - \epsilon_B L[B]}{\epsilon_A L}$$

Similarly:

$$[B] = \frac{Abs_T - \epsilon_A L[A]}{\epsilon_B L}$$

- 5) Uncertainty (variance) in the pK_a value can be estimated by typical error propagation calculations

$$\sigma_{pKa} = \sqrt{\left(\frac{\partial pKa}{\partial pH}\right)^2 * \sigma_{pH}^2 + \left(\frac{\partial pKa}{\partial R}\right)^2 * \sigma_R^2 + \sigma_{Reg}^2}$$

$$\frac{\partial pKa}{\partial pH} = 1 \text{ and } \frac{\partial pKa}{\partial R} = \frac{1}{R * \ln 10}$$

$$\therefore \sigma_{pKa} = (1)^2 * \sigma_{pH}^2 + \left(\frac{1}{R * \ln 10}\right)^2 * \sigma_R^2 + \sigma_{Reg}^2$$

- 6) The uncertainty in pH is found by including all error in the probe and meter used when taking pH measurements. This includes temperature error for pK_a values of the buffer components and error in the calibration standards specified by the manufacturer.

$$\sigma_{pH} = \sqrt{\sigma_{probe}^2 + \sigma_{meter}^2}$$

- 7) The uncertainty in R includes sample preparation (i.e. glassware errors) because the computed values are a direct result of the initial concentration of analyte present. The uncertainty in R also includes error in the computed values, [A] and [B] from the regression. R is a ratio and the variance can be written in the general error propagation format

$$\sigma_R = R * \sqrt{\left(\frac{\sigma_{[L]_0}}{L_0}\right)^2 + \left(\frac{\sigma_{[A]}}{[A]}\right)^2 + \left(\frac{\sigma_{[B]}}{[B]}\right)^2 - 2\sigma_{A,B}\left(\frac{\sigma_{[A]}}{[A]}\right)\left(\frac{\sigma_{[B]}}{[B]}\right)}$$

- 8) Uncertainty in the computed concentrations, [A] and [B], can be found by accounting for absorbance and pathlength errors.

$$[A] = \frac{Abs_T - \epsilon_B L [B]}{\epsilon_A L}$$

$$\sigma_{[A]} = \sqrt{\left(\frac{\partial [A]}{\partial Abs_T}\right)^2 * \sigma_{Abs_T}^2 + \left(\frac{\partial [A]}{\partial L}\right)^2 * \sigma_L^2}$$

$$\left(\frac{\partial[A]}{\partial Abs_T}\right) = \frac{1}{\epsilon_A L}$$

$$\left(\frac{\partial[A]}{\partial L}\right) = \frac{\partial}{\partial L}\left(\frac{Abs_T}{\epsilon_A L}\right) - \frac{\partial}{\partial L}\left(\frac{\epsilon_B L[B]}{\epsilon_A L}\right) = -\frac{Abs_T}{\epsilon_A L^2} - 0 = -\frac{Abs_T}{\epsilon_A L^2}$$

Similarly:

$$[B] = \frac{Abs_T - \epsilon_A L[A]}{\epsilon_B L}$$

$$\sigma_{[B]} = \sqrt{\left(\frac{\partial[B]}{\partial Abs_T}\right)^2 * \sigma_{Abs_T}^2 + \left(\frac{\partial[B]}{\partial L}\right)^2 * \sigma_L^2}$$

$$\left(\frac{\partial[B]}{\partial Abs_T}\right) = \frac{1}{\epsilon_B L}$$

$$\left(\frac{\partial[B]}{\partial L}\right) = \frac{\partial}{\partial L}\left(\frac{Abs_T}{\epsilon_B L}\right) - \frac{\partial}{\partial L}\left(\frac{\epsilon_A L[A]}{\epsilon_B L}\right) = -\frac{Abs_T}{\epsilon_B L^2} - 0 = -\frac{Abs_T}{\epsilon_B L^2}$$

- 9) Plugging these solutions into the equation from step 7, allows for uncertainty approximations for the R value. The proceeding R value from equation 7 will conveniently cancel with the R in equation 2 of step 5. Additionally, a -1.000 is entered as the correlation value as provided by the regression

σ_R

= R

$$* \sqrt{\left\{\left(\frac{\sigma_{[A]_0}}{L_0}\right)^2 + \left(\frac{1}{\epsilon_A L}\right)^2 * \sigma_{Abs_T}^2 + \left[-\frac{Abs_T}{\epsilon_A L^2}\right]^2 * \sigma_L^2 + \left(\frac{1}{\epsilon_B L}\right)^2 * \sigma_{Abs_T}^2 + \left[-\frac{Abs_T}{\epsilon_B L^2}\right]^2 * \sigma_L^2\right\} - 2(-1.000) \sqrt{\left(\frac{1}{\epsilon_A L}\right)^2 * \sigma_{Abs_T}^2 + \left(-\frac{Abs_T}{\epsilon_A L^2}\right)^2 * \sigma_L^2} * \sqrt{\left(\frac{1}{\epsilon_B L}\right)^2 * \sigma_{Abs_T}^2 + \left(-\frac{Abs_T}{\epsilon_B L^2}\right)^2 * \sigma_L^2}}$$

Note: The first term will simply be the total error in the preparation of the sample (glassware and pipetting errors). The highest values will be used for the absorbance the epsilon value (these occur at λ_{max}). Additionally, since there is a lack of a weighting scheme, the number of

wavelength data points (D) will be multiplied by the absorbance error and the number of samples (N) will be multiplied by the uncertainty in $[L]_0$ which is the initial dye concentration

σ_R

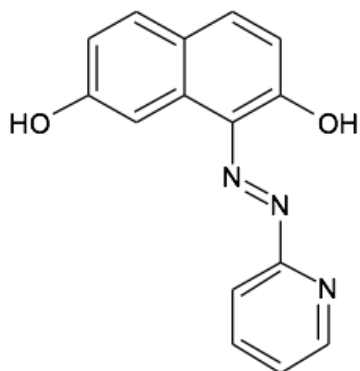
= R

$$* \sqrt{\left\{ \left[N * \left(\frac{\sigma_{[L]_0}}{L_0} \right)^2 \right] + \left[\left(\frac{D}{\epsilon_A L} \right)^2 * \sigma_{Abs_T}^2 \right] + \left[\left(-\frac{Abs_T}{\epsilon_A L^2} \right)^2 * \sigma_L^2 \right] + \left[\left(\frac{D}{\epsilon_B L} \right)^2 * \sigma_{Abs_T}^2 \right] + \left[\left(-\frac{Abs_T}{\epsilon_B L^2} \right)^2 * \sigma_L^2 \right] \right\} - 2(-1.000) \sqrt{\left(\frac{D}{\epsilon_A L} \right)^2 * \sigma_{Abs_T}^2 + \left(-\frac{Abs_T}{\epsilon_A L^2} \right)^2 * \sigma_L^2} * \sqrt{\left(\frac{D}{\epsilon_B L} \right)^2 * \sigma_{Abs_T}^2 + \left(-\frac{Abs_T}{\epsilon_B L^2} \right)^2 * \sigma_L^2}}$$

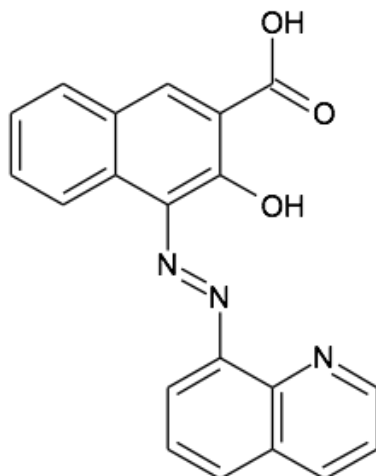
10) Finally, substituting into the equation from step 5

$$\begin{aligned} \sigma_{pKa} = & (1)^2 * \sigma_{pH}^2 + \left(\frac{1}{R * \ln 10} \right)^2 * R^2 * \left\{ \left[N * \left(\frac{\sigma_{[L]_0}}{L_0} \right)^2 \right] + \left[\left(\frac{D}{\epsilon_A L} \right)^2 * \sigma_{Abs_T}^2 \right] + \left[\left(-\frac{Abs_T}{\epsilon_A L^2} \right)^2 * \sigma_L^2 \right] + \left[\left(\frac{D}{\epsilon_B L} \right)^2 * \sigma_{Abs_T}^2 \right] + \left[\left(-\frac{Abs_T}{\epsilon_B L^2} \right)^2 * \sigma_L^2 \right] \right\} \\ & - 2(-1.000) \sqrt{\left(\frac{D}{\epsilon_A L} \right)^2 * \sigma_{Abs_T}^2 + \left(-\frac{Abs_T}{\epsilon_A L^2} \right)^2 * \sigma_L^2} * \sqrt{\left(\frac{D}{\epsilon_B L} \right)^2 * \sigma_{Abs_T}^2 + \left(-\frac{Abs_T}{\epsilon_B L^2} \right)^2 * \sigma_L^2} \\ & + \sigma_{Reg}^2 \end{aligned}$$

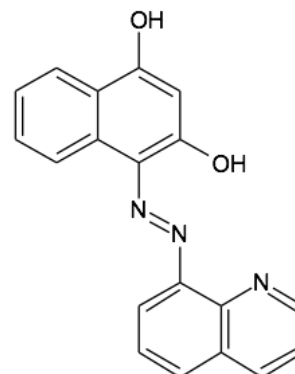
Appendix 2: Dye Structures



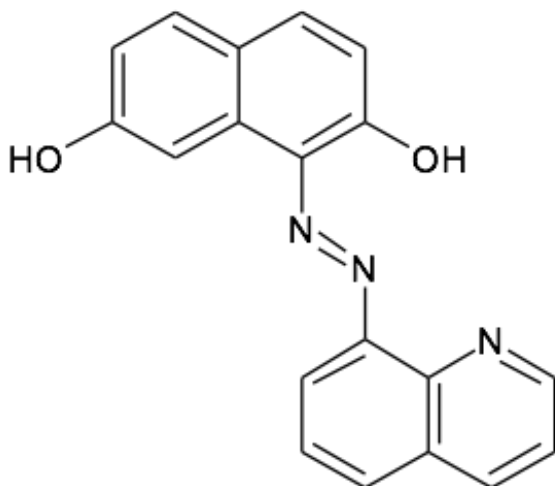
TMH-3-042
PAN-7OH
(E)-1-(pyridin-2-yl)diazenyl)naphthalene-2,7-diol



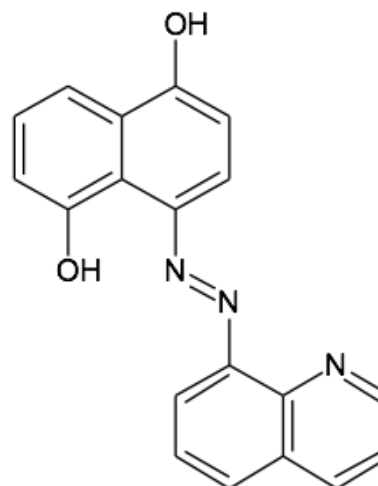
TMH-3-065
QAN-3A
(E)-3-hydroxy-4-(quinolin-8-yl)diazenyl)-2-naphthoic acid



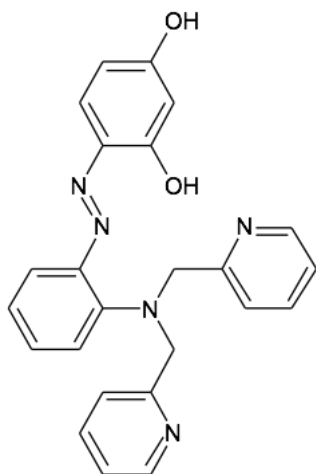
TMH-3-068B
QAN-4OH
(E)-4-(quinolin-8-yl)diazenyl)naphthalene-1,3-diol



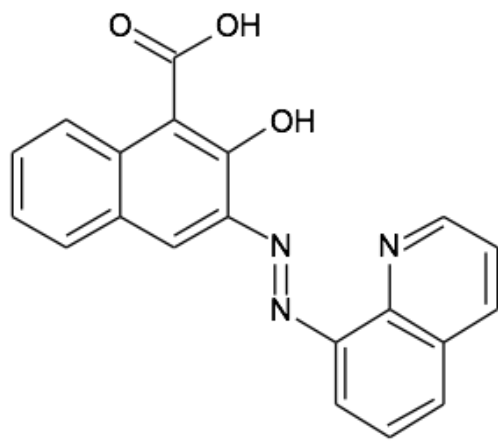
TMH-3-068A
QAN-7OH
(E)-1-(quinolin-8-yl)diazenyl)naphthalene-2,7-diol



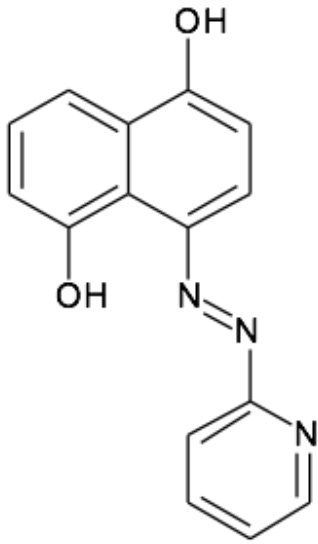
TMH-3-080
QAN-1,5OH
(E)-4-(quinolin-8-yl)diazenyl)naphthalene-1,5-diol



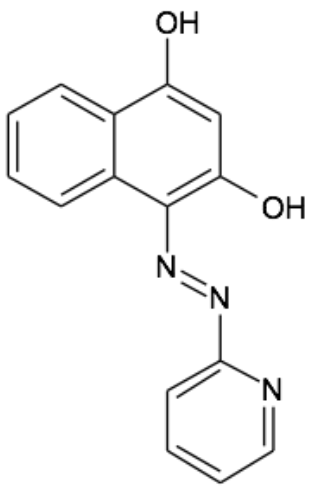
TMH-3-085
 DAR
 (E)-4-((2-(benzyl(pyridin-2-ylmethyl)amino)phenyl)diazenyl)benzene-1,2-diol



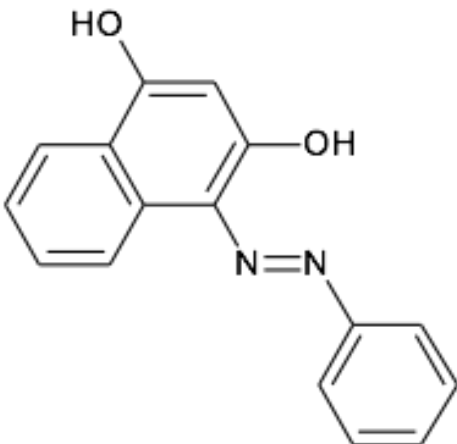
TMH-3-065B
 QAN-1A
 (E)-2-hydroxy-3-(quinolin-8-ylidiazenyl)-1-naphthoic acid



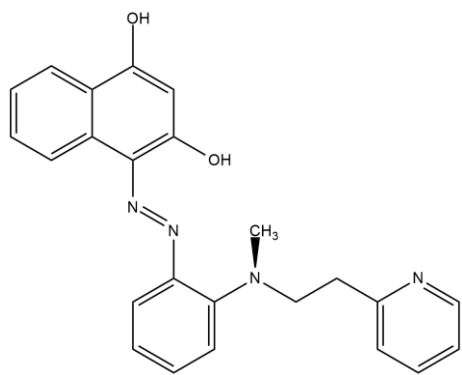
TMH-3-087C
 PAN-1,5OH
 (E)-4-(pyridin-2-ylidiazenyl)naphthalene-1,5-diol



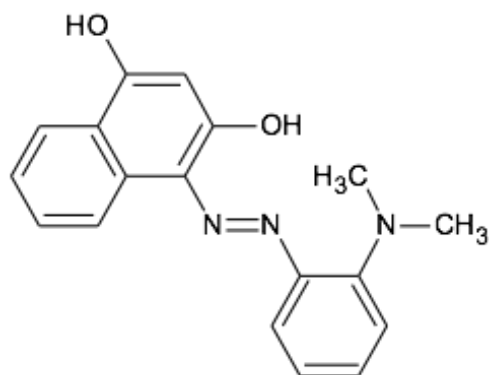
TMH-3-087
 PAN-4OH
 (E)-4-(pyridin-2-ylidiazenyl)naphthalene-1,3-diol



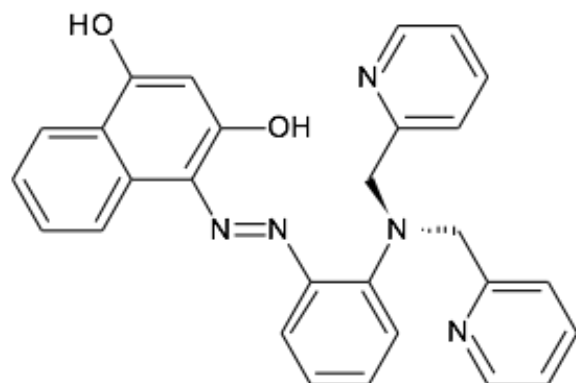
TMH-3-114C
 4-((E)-[2-(morpholin-4-yl)phenyl]diazenyl)naphthalene-1,3-diol



TMH-3-111C
 (E)-4-((2-(methyl(3-phenylpropyl)amino)phenyl)diazenyl)naphthalene-1,3-diol

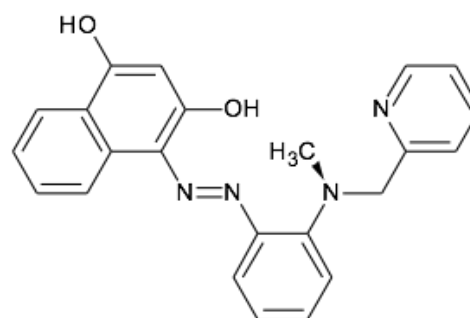


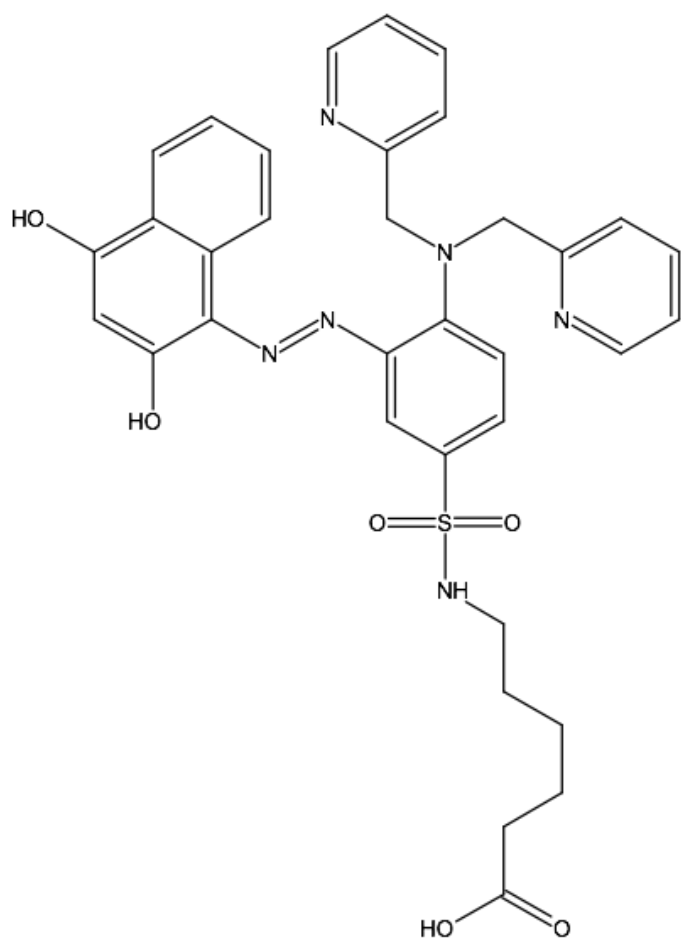
TMH-3-109B
 4-{(E)-[2-(dimethylamino)phenyl]diazenyl}naphthalene-1,3-diol



TMH-3-102c'
 DAN-4OH
 (E)-4-((2-(bis(pyridin-2-yl)methyl)amino)phenyl)diazenyl)naphthalene-1,3-diol

TMH-3-107C
 4-[(E)-2-(2-{methyl[(pyridin-2-yl)methyl]amino}phenyl)diazenyl]naphthalene-1,3-diol

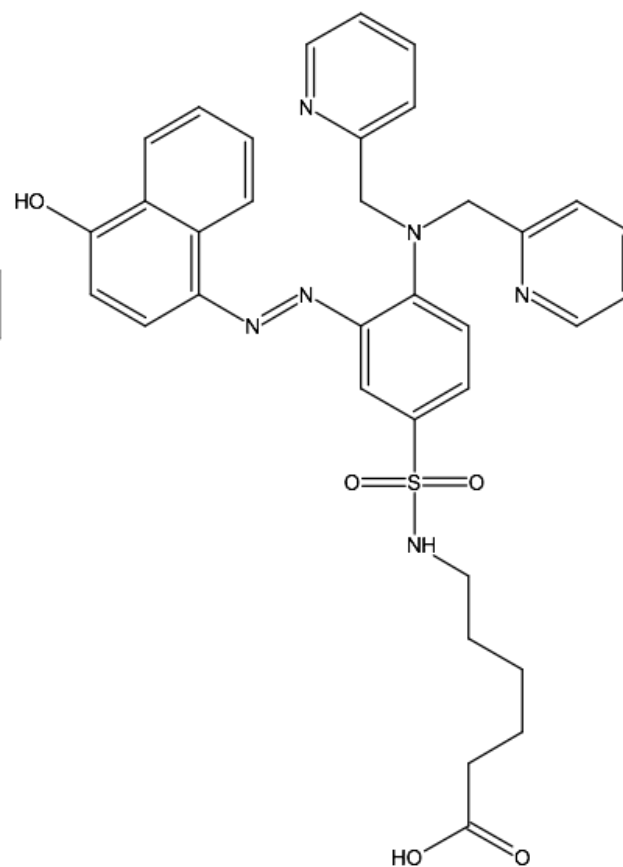




TMH-3-149B

OAN-4OH-SA-DPA

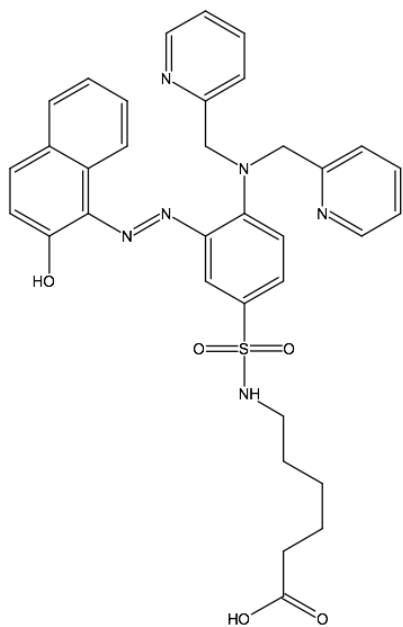
(E)-6-(4-(bis(pyridin-2-ylmethyl)amino)-3-((2,4-dihydroxynaphthalen-1-yl)diazenyl)phenylsulfonamido)hexanoic acid



TMH-3-151C

OAN-4-SA-DPA

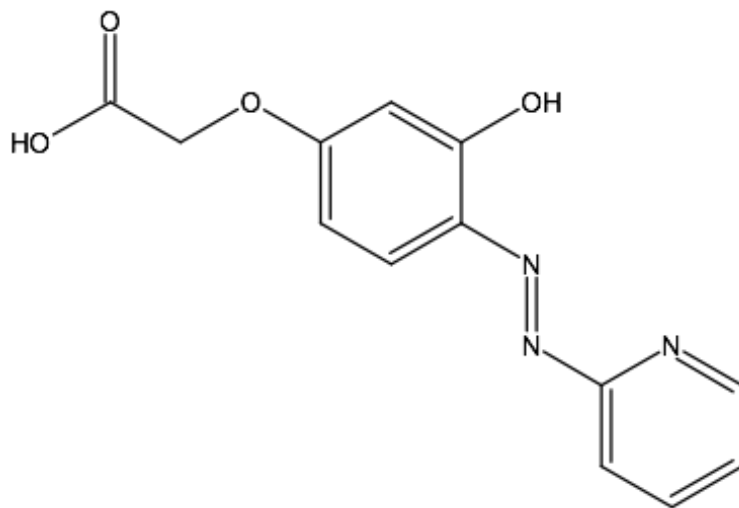
(E)-6-(4-(bis(pyridin-2-ylmethyl)amino)-3-((4-hydroxynaphthalen-1-yl)diazenyl)phenylsulfonamido)hexanoic acid



TMH-???

OAN-2-SA-DPA

(E)-2-(3-hydroxy-4-(pyridin-2-ylidiazenyl)phenoxy)acetic acid

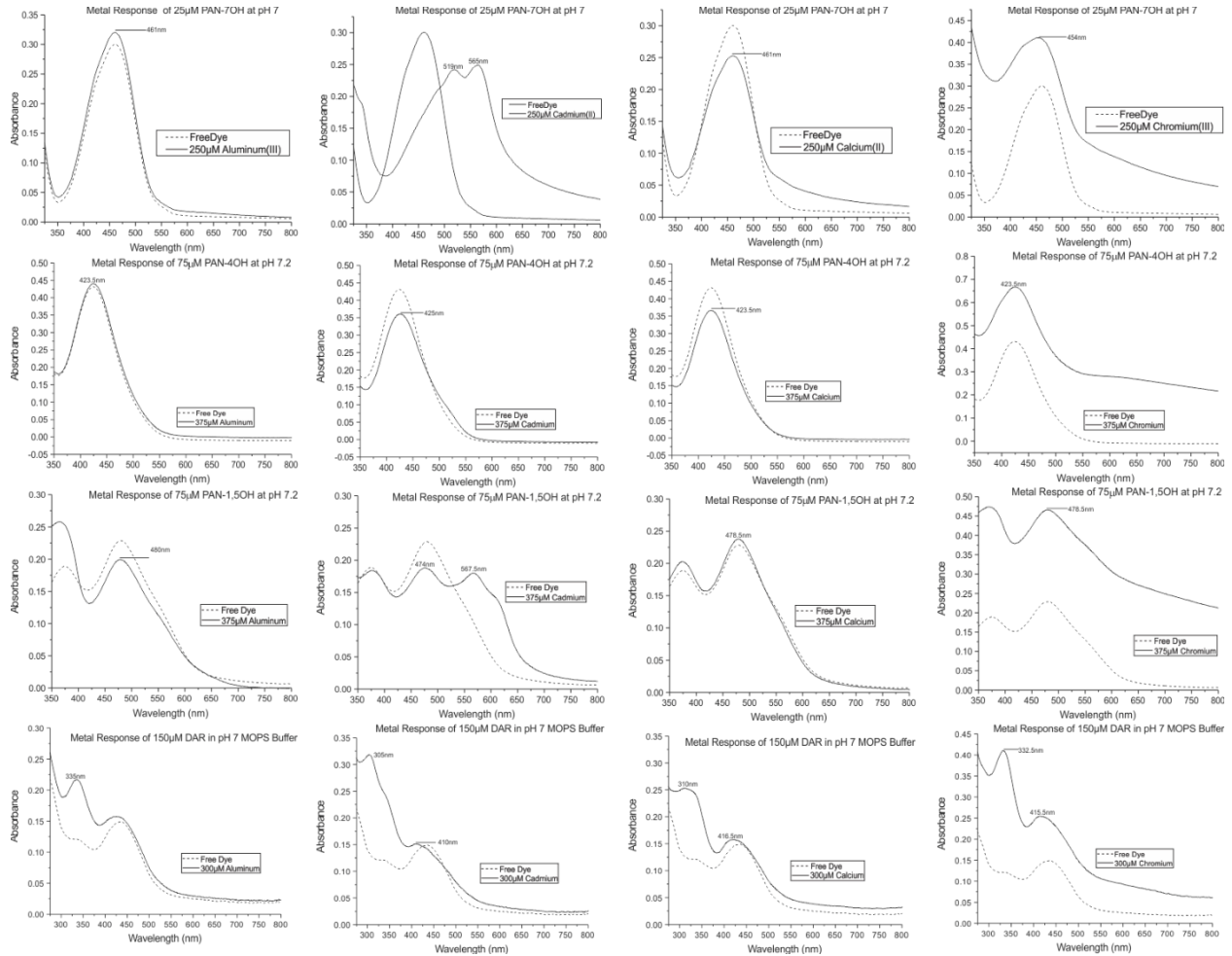


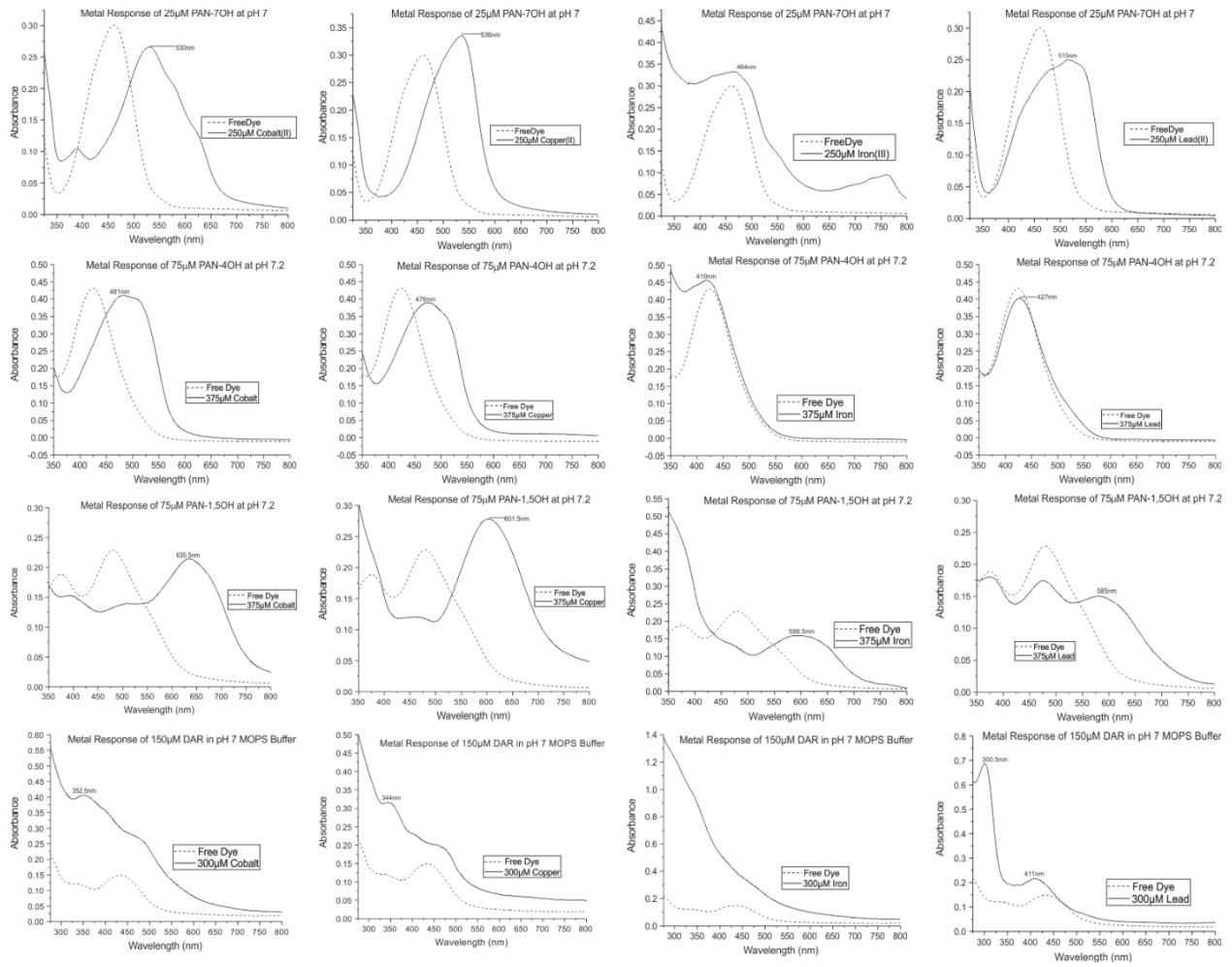
TMH-3-151B

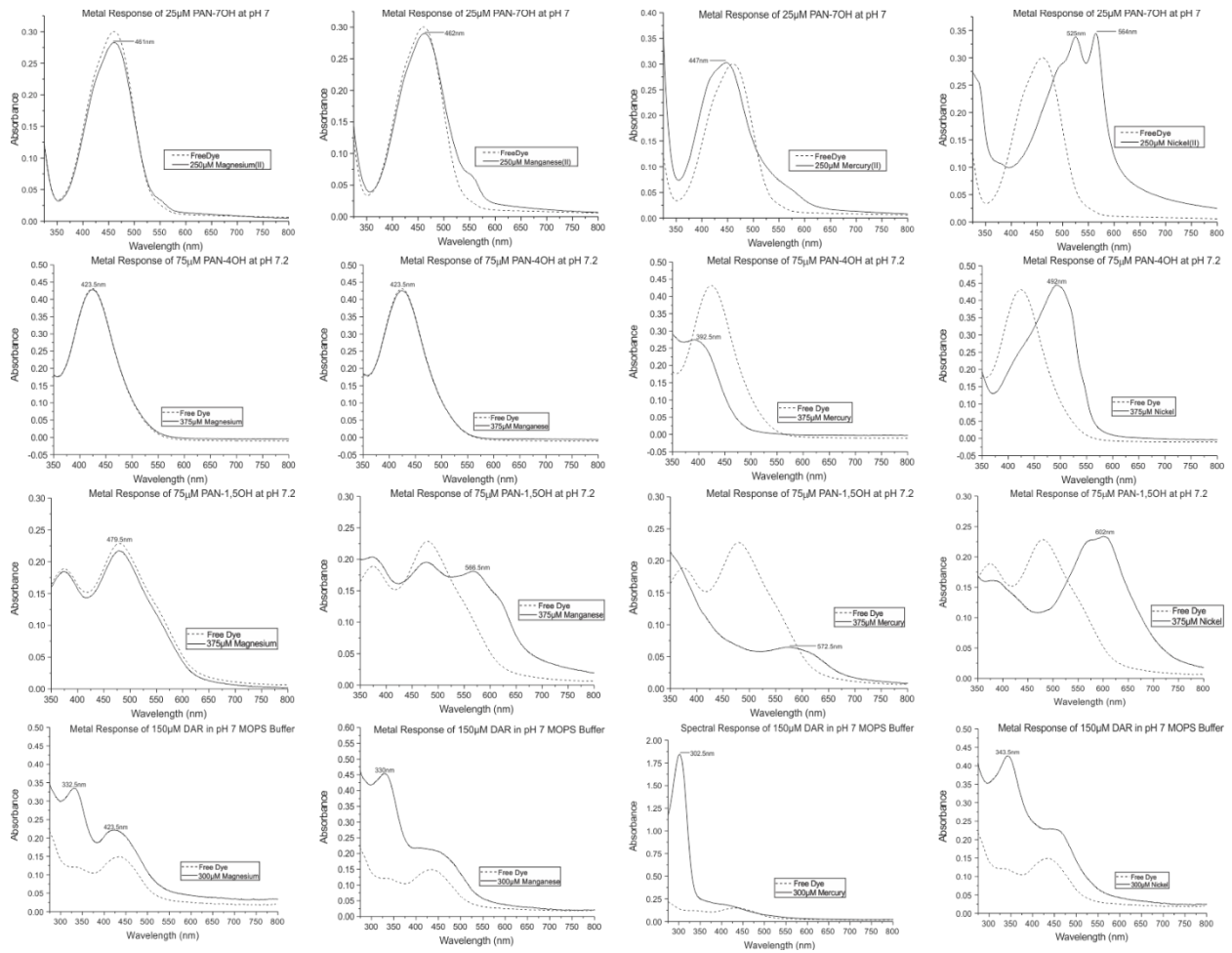
OAN-2-5A-DPA

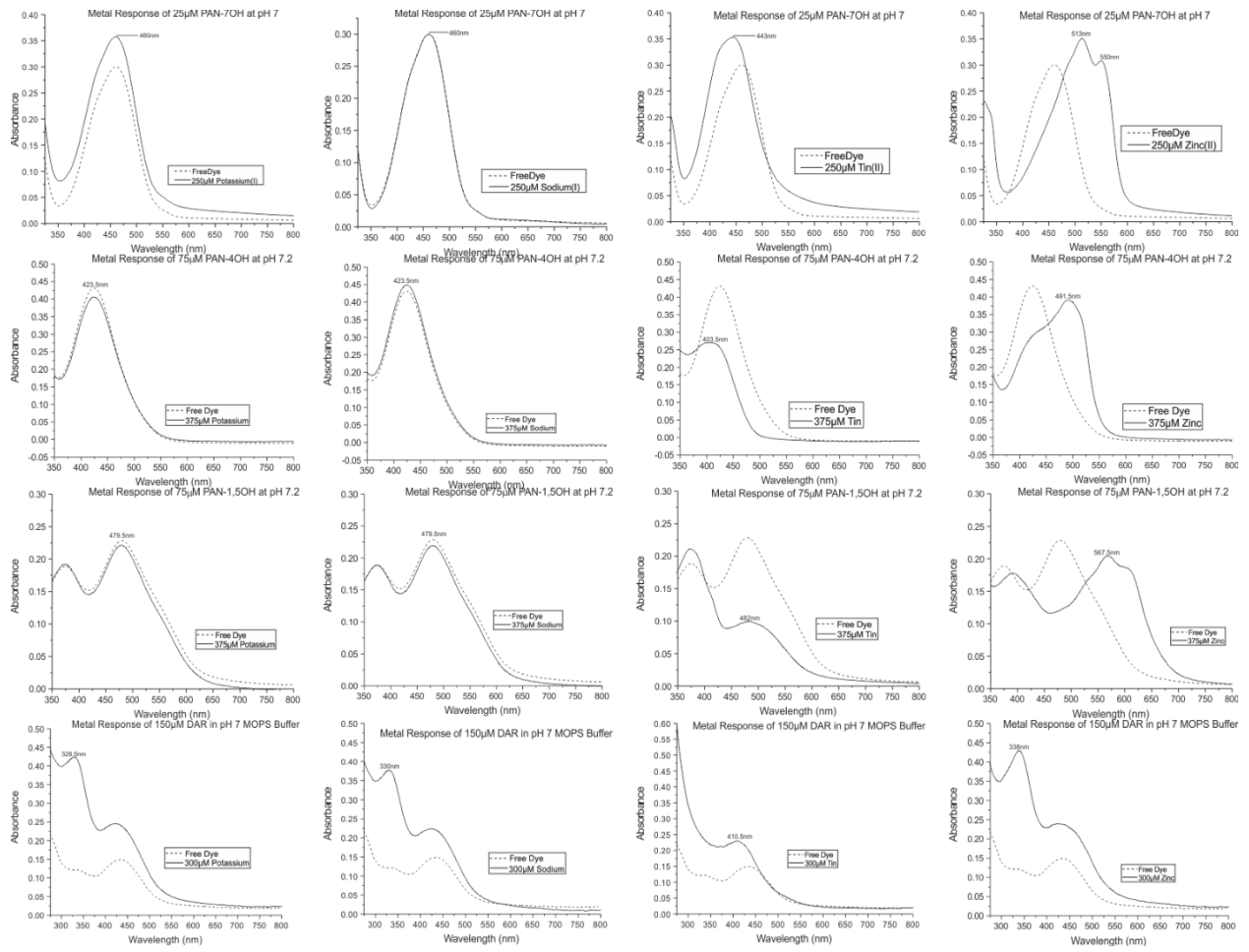
(E)-6-(4-(bis(pyridin-2-ylmethyl)amino)-3-((2-hydroxynaphthalen-1-yl)diazenyl)phenyl)sulfonamido)hexanoic acid

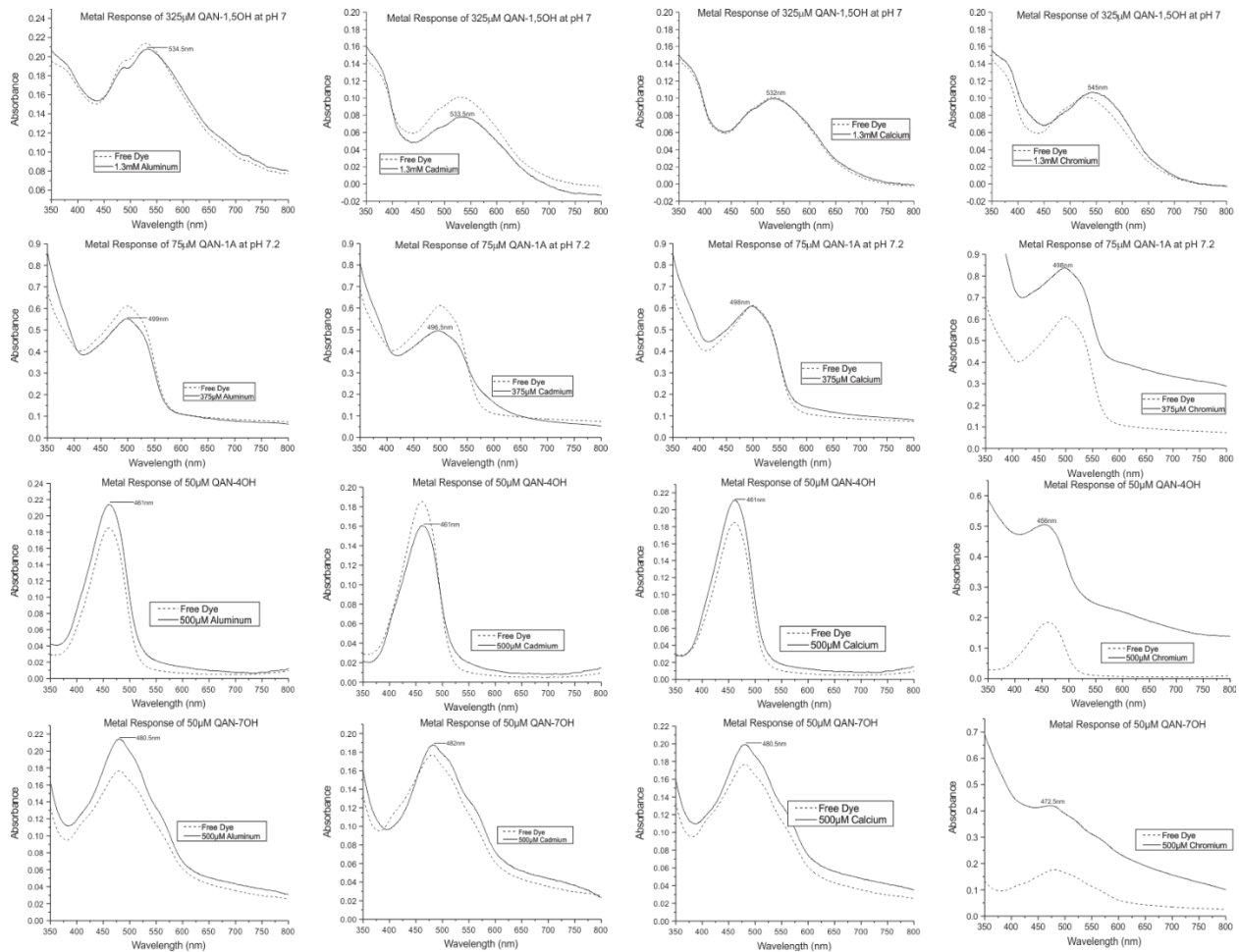
Appendix 3: Metal Responses

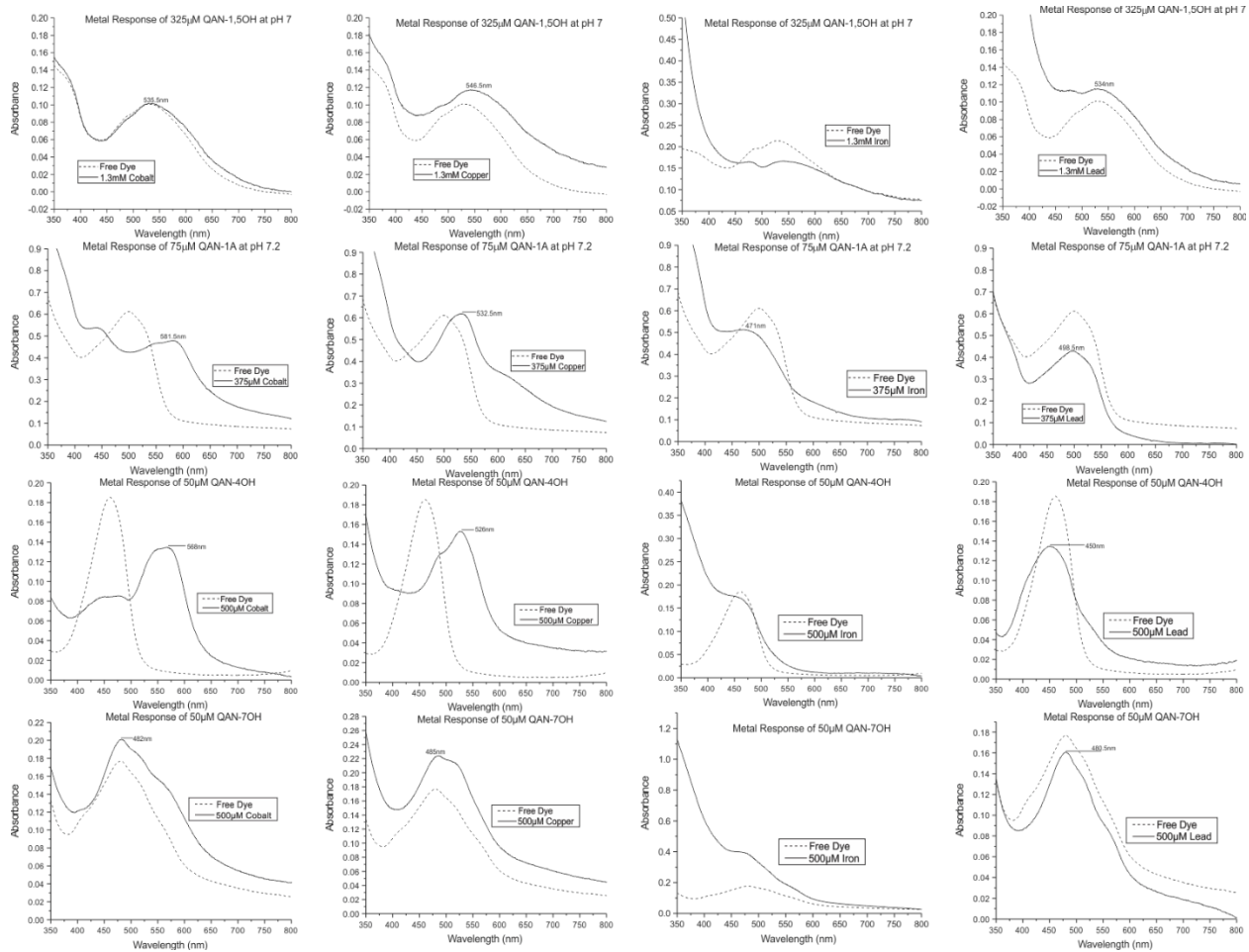


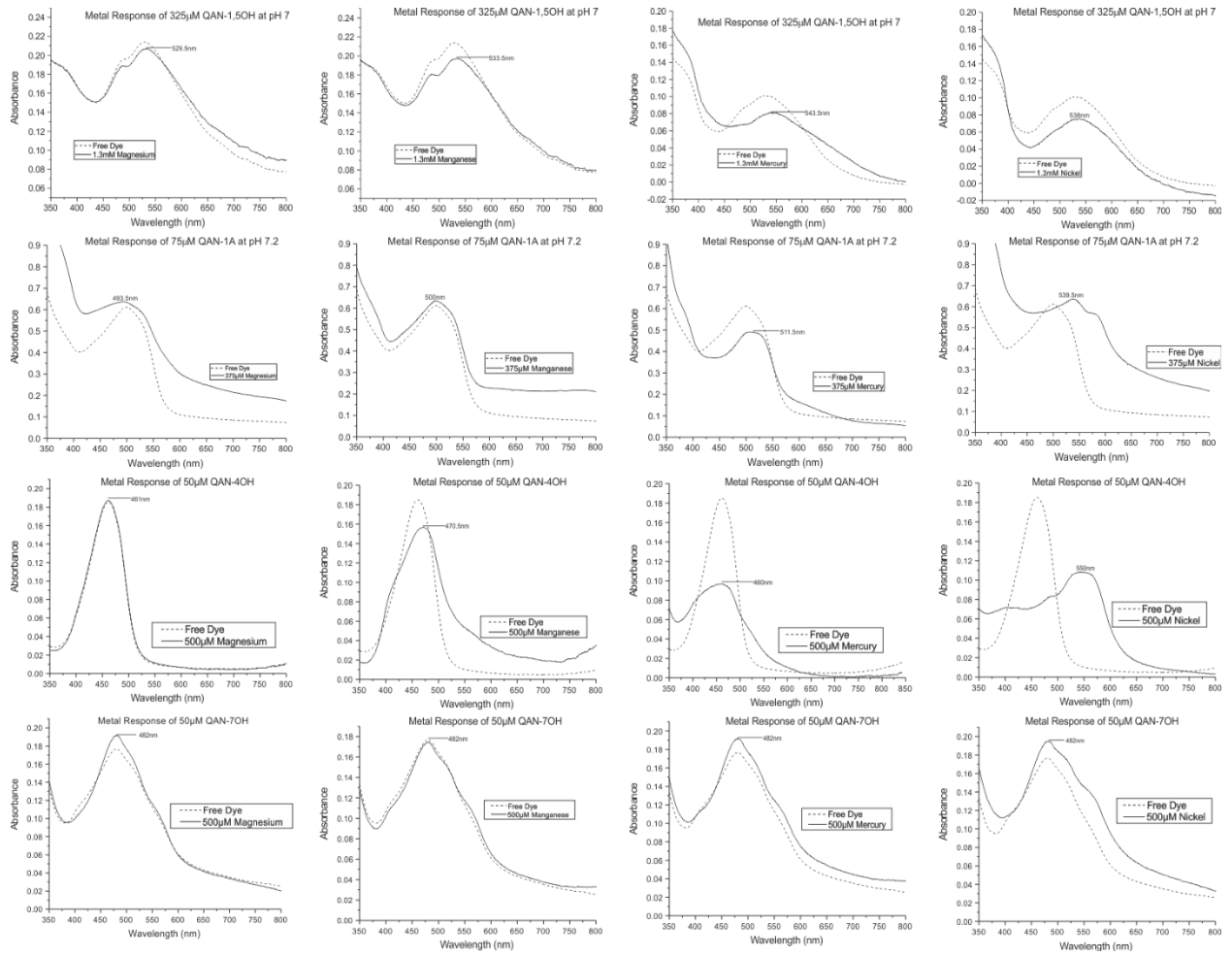












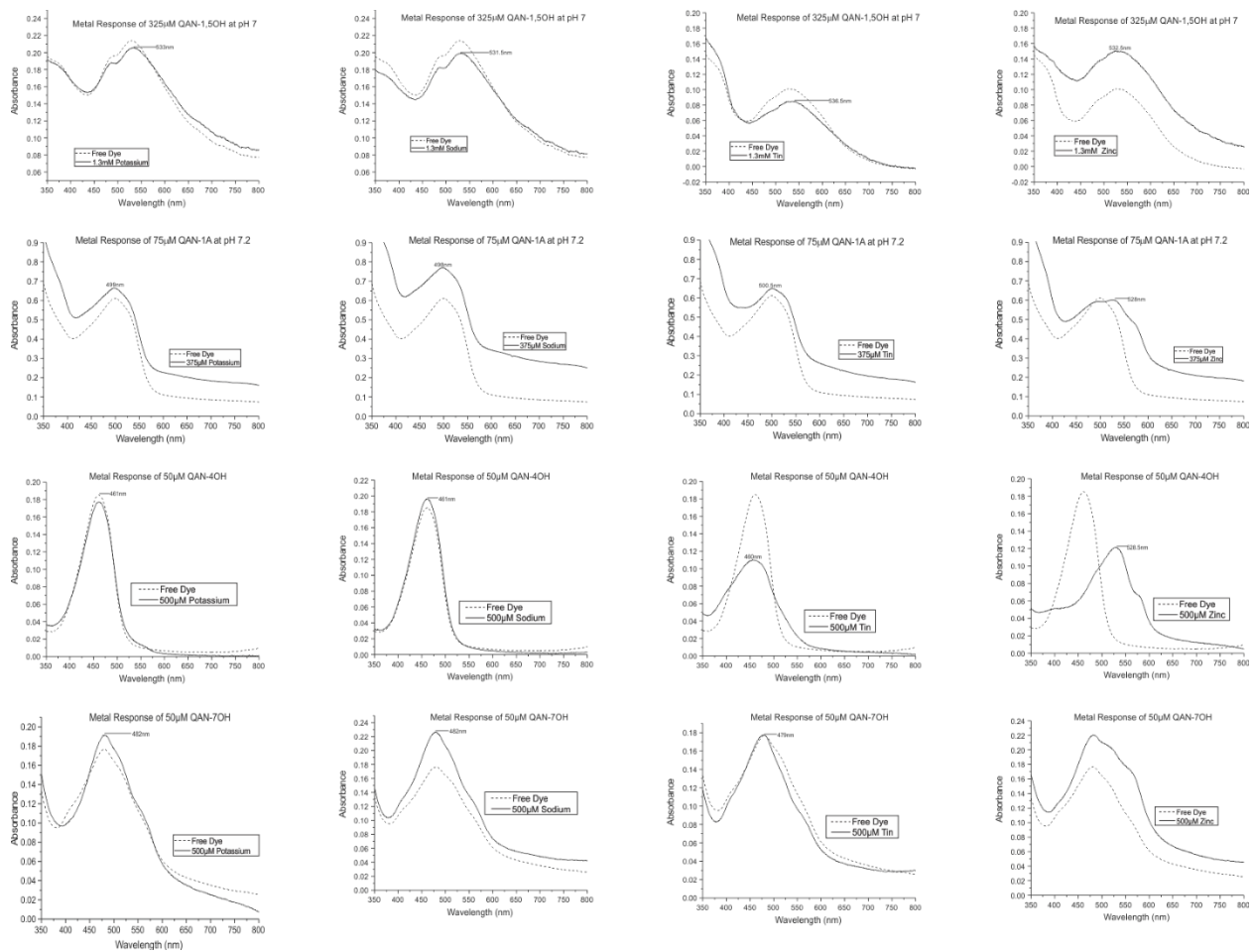


Figure 61: Spectral response of 8 novel azo dyes to 16 different heavy metals. Spectral responses can be useful in creating a spectral selectivity in an array of metal sensors. The unique or even similar response can give the information needed to distinguish multiple metals in solution.

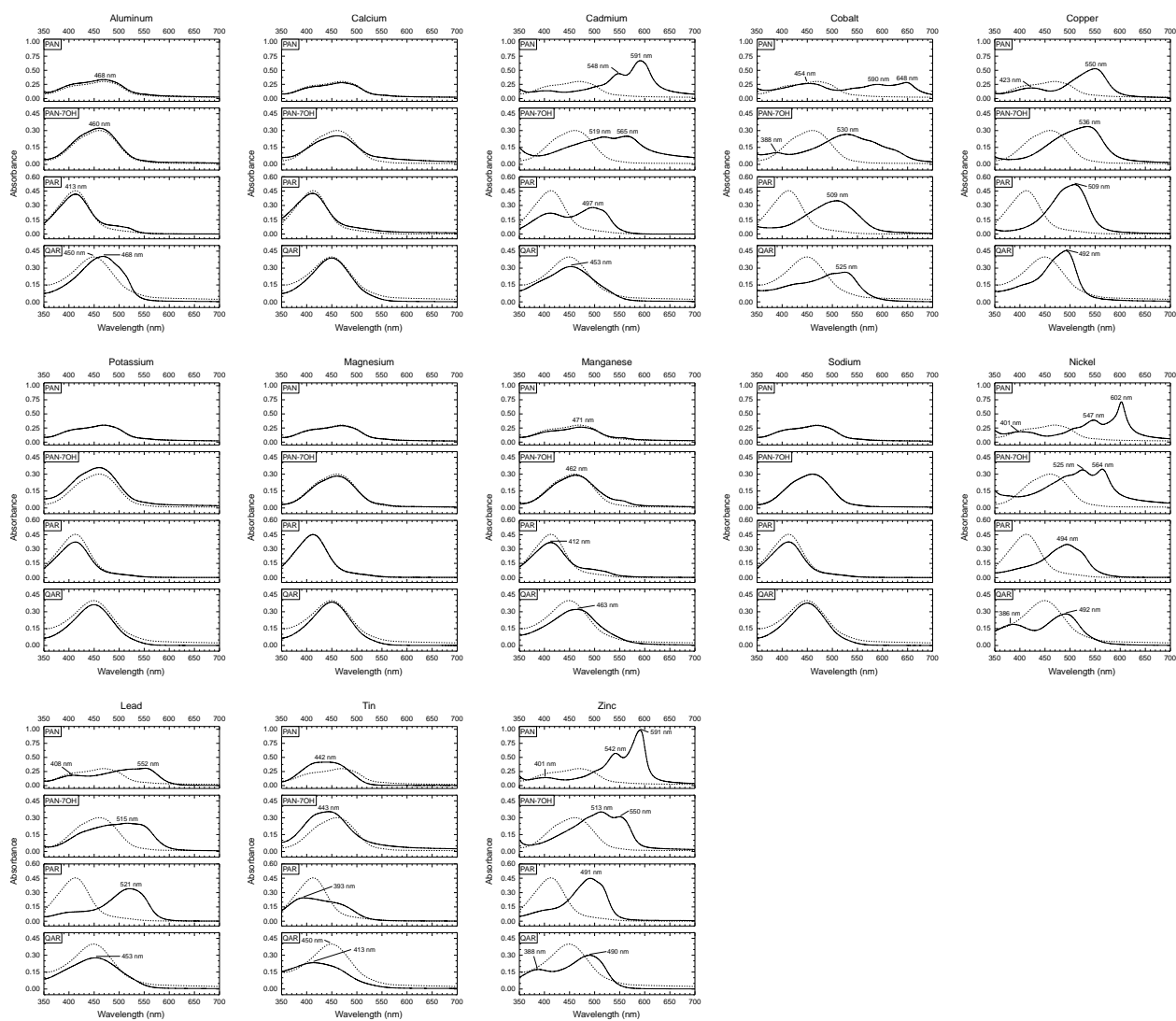


Figure 62: Characteristic responses of the 4 dyes from Figure 2 to a variety of metal ions (pH 7.0). The visual response can give some insight into what metals might complex with the dye, but the spectral response can give exact characteristics and be useful in determining the capability of the dye to be a sensor.

References

- (1) Aragay, G.; Pons, J.; Merkoçi, A. Recent Trends in Macro-, Micro-, and Nanomaterial-Based Tools and Strategies for Heavy-Metal Detection. *Chem. Rev.* **2011**, *111* (5), 3433–3458.
- (2) Lozoff, B.; Beard, J.; Connor, J.; Felt, B.; Georgieff, M. Long-Lasting Neural and Behavioral Effects of Iron Deficiency in Infancy. *Nutr Rev.* **2006**, *64*.
- (3) Cuajungcoa, M.; Lees, G. Zinc Metabolism in the Brain: Relevance to Human Neurodegenerative Disorders. *Neurobiol. Dis.* **1997**, *4*, 137–169.
- (4) Choi, D.; Koh, J. Zinc and Brain Injury. *Annu. Rev. Neurosci.* **1998**, *21*, 347–375.
- (5) Falchuk, K. The Molecular Basis for the Role of Zinc in Developmental Biology. In *Molecular and Cellular Biochemistry*; 1998; p 41048.
- (6) WOLFGANG, M.; CLAUS, J.; VALLEE, B.; FISCHER, E. Inhibitory Sites in Enzymes : Zinc Removal and Reactivation by Thionein. *Proc. Natl. Aca. Sci.* **1999**, *96* (March), 1936–1940.
- (7) O’Dell, B.; Sunde, R. *Handbook of Nutritionally Essential Mineral Elements*; 1997.
- (8) Shils, M.; Shike, M.; Ross, A.; Caballero, B.; Cousins, R. Modern Nutrition in Health and Disease. *J. Chem. Inf. Model.* **2013**, *53* (9), 1689–1699.
- (9) Nutrient Reference Values <https://www.nrv.gov.au/nutrients/copper>.
- (10) Poulson, B.; Wilkins, J. *Cobalt*.
- (11) Khatri, M. Vitamin B-12: What to Know <https://www.webmd.com/diet/vitamin-b12-deficiency-symptoms-causes#2>.
- (12) EPA. Basic Information about Lead in Drinking Water <https://www.epa.gov/ground-water-and-drinking-water/basic-information-about-lead-drinking-water#getinto>.
- (13) NIOSH. Health Problems Caused by Lead <https://www.cdc.gov/niosh/topics/lead/health.html>.
- (14) Tchounwou, P. B.; Yedjou, C. G.; Patlolla, A. K.; Sutton, D. J. Heavy Metals Toxicity and the Environment. **2012**, *101*, 1–30.
- (15) Kanluen, R.; Amer, S. I. *Treating Plating Wastewater*; 2001.
- (16) Caroli, S.; Forte, G.; Iamiceli, A. L.; Galoppi, B. Determination of Essential and Potentially Toxic Trace Elements in Honey by Inductively Coupled Plasma-Based Techniques. *Talanta* **1999**, *50* (2), 327–336.
- (17) Townsend, A. T.; Miller, K. A.; Aldous, S. The Determination of Copper , Zinc , Cadmium and Lead in Urine by High Resolution Inductively Coupled Plasma Mass Spectrometry . The Determination of Copper , Zinc , Cadmium and Lead in Urine by High Resolution ICP-MS. **1998**, No. May 2014.
- (18) Gasparik, J. .; Vladarova, D. .; Capcarova, M. .; Smehyl, P. .; Slamecka, J.; Garaj, P.; Stawarz, R.; Massanyi, P. J. Concentration of Lead, Cadmium, Mercury and Arsenic in Leg Skeletal Muscles of Three Species of Wild Birds. *J. Environ. Sci. Heal.* **2010**, *45* (7).
- (19) Pohl, P. Determination of Metal Content in Honey by Atomic Absorption and Emission Spectrometries. *TrAC trends Anal. Chem.* **2009**, *28* (1), 117–128.
- (20) Zare-Shahabadi, V.; Asaadi, P.; Abbasitabar, F.; Shirmardi, A. Determination of Traces of Ni, Cu, and Zn in Wastewater and Alloy Samples by Flame-AAS after Ionic Liquid-Based Dispersive Liquid Phase Microextraction. *J. Braz. Chem. Soc.* **2017**, *28* (5), 887–894.
- (21) Lin, T.-W.; Huang, S.-D. Direct and Simultaneous Determination of Copper, Chromium, Aluminum, and Manganese in Urine with a Multielement Graphite Furnace Atomic

- Absorption Spectrometer. *Anal. Chem.* **2001**, *73* (17), 4319–4325.
- (22) Chen, L.; Lei, Z.; Yang, S.; Wen, X. Application of Portable Tungsten Coil Electrothermal Atomic Absorption Spectrometer for the Determination of Trace Cobalt after Ultrasound-Assisted Rapidly Synergistic Cloud Point Extraction. *Microchem. J.* **2017**, *130*, 452–457.
- (23) Oehme, I.; Prokes, B.; Murkovic, I.; Werner, T.; Klimant, I.; Wolfbeis, O. LED-Compatible Copper(II)-Selective Optrode Membrane Based on Lipophilized Zincon. *Fresenius. J. Anal. Chem.* **1994**, *350* (7–9), 563–567.
- (24) Wang, K.; Seiler, K.; Rusterholz, B.; Simon, W. Characterization of an Optode Membrane for Zinc(II) Incorporating a Lipophilized Analogue of the Dye 4-(2-Pyridylazo)Resorcinol. *Analyst* **1992**, *117* (1).
- (25) Oehme, I.; Wolfbeis, O. S. Optical Sensors for Determination of Heavy Metal Ions. *Mikrochim. Acta* **1997**, *126* (3–4), 177–192.
- (26) Alreja, P.; Kaur, N. Recent Advances in 1,10-Phenanthroline Ligands for Chemosensing of Cations and Anions. *RSC Adv.* **2016**, *6* (28), 23169–23217.
- (27) Busschaert, N.; Caltagirone, C.; Van Rossom, W.; Gale, P. A. Applications of Supramolecular Anion Recognition. *Chem. Rev.* **2015**, *115* (15), 8038–8155.
- (28) Carter, K. P.; Young, A. M.; Palmer, A. E. Fluorescent Sensors for Measuring Metal Ions in Living Systems. *Chem. Rev.* **2014**, *114* (8), 4564–4601.
- (29) Kim, H. N.; Ren, W. X.; Kim, J. S.; Yoon, J. Fluorescent and Colorimetric Sensors for Detection of Lead, Cadmium, and Mercury Ions. *Chem. Soc. Rev.* **2012**, *41* (8), 3210–3244.
- (30) Wong, J. K. H.; Todd, M. H.; Rutledge, P. J. Recent Advances in Macrocyclic Fluorescent Probes for Ion Sensing. *Molecules* **2017**, *22* (2).
- (31) Zhang, J. F.; Zhou, Y.; Yoon, J.; Kim, J. S. Recent Progress in Fluorescent and Colorimetric Chemosensors for Detection of Precious Metal Ions (Silver, Gold and Platinum Ions). *Chem. Soc. Rev.* **2011**, *40* (7), 3416–3429.
- (32) Meeusen, J.; Tomasiewicz, H. N. A.; Petering, D. TSQ, a Common Fluorescent Sensor for Cellular Zinc, Images Zinc Proteins. *Inorg chem* **2011**, *50* (16), 7563–7573.
- (33) Nowakowski, A.; Petering, D. Reactions of the Fluorescent Sensor, Zinquin, with the Zinc-Proteome: Adduct Formation and Ligand Substitution. *Inorg chem* **2011**, *50* (20), 10124–10133.
- (34) Meeusen, J.; Andrew Nowakowski, A Petering, D. Reaction of Metal Binding Ligands with the Zinc Proteome: Zinc Sensors and TPEN. *Inorg chem* **2012**, *51* (6), 3625–3632.
- (35) Nowakowski, A.; Petering, D. Sensor Specific Imaging of Proteomic Zn²⁺ with Zinquin and TSQ after Cellular Exposure to N-Ethylmaleimide. **2013**, *4* (5), 448–456.
- (36) Burdette, S. C.; Walkup, G. K.; Spingler, B.; Tsien, R. Y.; Lippard, S. J. Fluorescent Sensors for Zn²⁺ Based on a Fluorescein Platform : Synthesis , Properties and Intracellular Distribution. *J. Am. Chem. Soc.* **2001**, No. 22, 7831–7841.
- (37) Buccella, D.; Horowitz, J. A.; Lippard*, S. J. Understanding Zinc Quantification with Existing and Advanced Ditopic Fluorescent Zinpyr Sensors. *J. Am. Chem. Soc.* **2011**, *133* (11), 4101–4114.
- (38) Chang, C. J.; Nolan, E. M.; Jaworski, J.; Burdette, S. C.; Sheng, M.; Lippard, S. J. Bright Fluorescent Chemosensor Platforms for Imaging Endogenous Pools of Neuronal Zinc. *Chem. Biol.* **2004**, *11*, 203–210.
- (39) Nolan, E.; Burdette, S.; Harvey, J.; Hilderbrand, S.; Lippard, S. Synthesis and

- Characterization of Zinc Sensors Based on a Monosubstituted Fluorescein Platform. *Inorg chem* **2004**, *43* (8), 2624–2635.
- (40) Lippard, C. R. G. S. J. 6-Methylpyridyl for Pyridyl Substitution Tunes the Properties of Fluorescent Zinc Sensors of the Zinpyr Family. *Inorg chem* **2006**, *45* (2), 555–561.
- (42) Nolan, E.; Jaworski, J.; Okamoto, K.; Hayashi, Y.; Sheng, M.; Lippard, S. QZ1 and QZ2: Rapid, Reversible Quinoline-Derivatized Fluoresceins for Sensing Biological Zn(II). *J. Am. Chem. Soc.* **2005**, *127* (48), 16812–16823.
- (43) Burdette, S. C.; Frederickson, C. J.; Bu, W.; Lippard, S. J. ZP4, an Improved Neuronal Zn²⁺ Sensor of the Zinpyr Family. *J. Am. Chem. Soc.* **2003**, No. 33, 1778–1787.
- (44) Walkup, G. K.; Burdette, S. C.; Lippard, S. J.; Tsien, R. Y. A New Cell-Permeable Fluorescent Probe for Zn²⁺. **2000**, No. 27, 5644–5645.
- (45) Davidson, M. Photobleaching
<http://micro.magnet.fsu.edu/primer/java/fluorescence/photobleaching/>.
- (46) Valeur, B. *Molecular Fluorescence*; 2001.
- (47) Aldstadt, J. H.; Olson, D. C.; Wolcott, D. K.; Marshall, G. D.; Stieg, S. W. Flow and Sequential Injection Analysis Techniques in Process Analysis. *Encycl. Anal. Chem.* **2006**.
- (48) Paul, M. Classification of Process Analysis: Offline, Atline, Online, Inline. *ResearchGate* **2009**.
- (49) Clark, M. *Handbook of Textile and Industrial Dyeing*; 2011.
- (50) Amchova, P.; Kotolova, H.; Ruda-kucerova, J. Health Safety Issues of Synthetic Food Colorants. *Regul. Toxicol. Pharmacol.* **2015**, *73* (3), 914–922.
- (51) Mohr, G.; Wolfbeis, O. Optical Sensors for a Wide PH Range Based on Azo Dyes Immobilized on a Novel Support. *Anal. Chim. Acta* **1994**, *292* (1–2), 41–48.
- (52) Wainwright, M. Dyes in the Development of Drugs and Pharmaceuticals. *Dye. Pigment.* **2008**, *76*, 582–589.
- (53) Corsini, A.; Yih, I. M.-L.; Fernando, Q.; Freiser, H. Potentiometric Investigation of the Metal Complexes of 1-(2-Pyridylazo)-2-Naphthol and 4-(2-Pyridylazo)-Resorcinol. *Anal. Chem.* **1962**, *34* (9), 1090–1093.
- (54) Ghasemi, J.; Niazi, A.; Kubista, M.; Elbergali, A. Spectrophotometric Determination of Acidity Constants of 4-(2-Pyridylazo) Resorcinol in Binary Methanol – Water Mixtures. *Anal. Chim. Acta* **2002**, *455* (2), 335–342.
- (55) Ghasemi, J.; Niazi, A.; Maeder, M. Spectrophotometric Studies on the Protonation and Nickel Complexation Equilibria of 4-(2-Pyridylazo) Resorcinol Using Global Analysis in Aqueous Solution. *Analysis* **2007**, *18* (2), 267–272.
- (56) Rouhollahi, A.; Kiaie, F. M.; Ghasemi, J. Multiwavelength Spectrophotometric Determination of Protolytic Constants of 4-(2-Pyridylazo) Resorcinol (PAR) in Binary DMF-Water Mixtures. *Talanta* **2005**, *66* (3), 653–658.
- (57) Fenske, T.; Oehm, S.; Hagemann, T.; Henning, P.; Labeots, J.; Schwabacher, A. Development of a Chemosensing Hydrogel Polymer Capable of the Real-Time Quantitation of Zn²⁺ in Aqueous Solutions. *pending* **2019**.
- (58) Quang, D. T.; Kim, J. S. Fluoro- and Chromogenic Chemodosimeters for Heavy Metal Ion Detection in Solution and Biospecimens. **2010**, 6280–6301.
- (59) Szurdoki, F.; Ren, D.; Walt, D. A Combinatorial Approach To Discover New Chelators for Optical Metal Ion Sensing. **2000**, *72* (21).
- (60) Zhang, X.; Yin, J.; Yoon, J. Recent Advances in Development of Chiral Fluorescent and

- Colorimetric Sensors. *Chem. Rev.* **2014**, *114*, 4918–4959.
- (61) Hunt, J.; Neece, S.; Ginsburg, A. “The Use of 4-(2-Pyridylazo)Resorcinol in Studies of Zinc Release from Escherichia Coli Aspartate Transcarbamoylas. *Anal. Biochem.* **1985**, *146*, 150–157.
- (62) Mikami, D.; Ohki, T.; Yamaji, K.; Ishihara, S.; Citterio, D.; Hagiwara, M.; Suzuki, K. Quantification of Ternary Mixtures of Heavy Metal Cations from Metallochromic Absorbance Spectra Using Neural Network Inversion. *Anal. Chem.* **2004**, *76* (19), 5726–5733.
- (63) Gismera, M. J.; Arias, S.; Sevilla, Ma Teresa Procopio, J. R. Simultaneous Quantification of Heavy Metals Using a Solid State Potentiometric Sensor Array. *Electroanalysis* **2009**, *21*(8) (1), 979–987.
- (64) Keithley, R. B.; Wightman, R. M. Component Regression With Residual Analysis. *October* **2010**, *28* (9), 1127–1136.
- (65) Maeder, M.; King, P. *Chemometrics in Practical Applications*; 2012.
- (66) Maeder, M.; Neuhold, Y.-M. *Practical Data Analysis in Chemistry*; 2007.
- (67) A Short Primer on Chemometrics for Spectroscopists. SpectroscopyNOW 2014.
- (68) Gans, P.; Sabatini, A.; Vacca, A. Investigation of Equilibria in Solution. Determination of Equilibrium Constants with the HYPERQUAD Suite of Programs. *Talanta* **1996**, *43*, 1739–1753.
- (69) Norman, S.; Maeder, M. Model-Based Analysis for Kinetic and Equilibrium Investigations. *Crit. Rev. Anal. Chem.* **2006**, *36* (3–4), 199–209.
- (70) Wold, S.; Sjostrom, M. PLS-Regression: A Basic Tool of Chemometrics. **2001**, 109–130.
- (71) Esbensen, K. *Multivariate Data Analysis: In Practice*; 2002.
- (72) Mehmood, T.; Ahmed, B. The Diversity in the Applications of Partial Least Squares: An Overview. *J. Chemom.* **2016**, *30* (1), 4–17.
- (73) Abdi, H. Partial Least Squares Regression and Projection on Latent Structure Regression (PLS Regression). *Wiley Interdiscip. Rev. Comput. Stat.* **2010**, *2* (1), 97–106.
- (74) Wold, S.; Høy, M.; Martens, H.; Trygg, J.; Westad, F.; MacGregor, J.; Wise, B. M. The PLS Model Space Revisited. *J. Chemom.* **2009**, *23* (2), 67–68.
- (75) Godoy, J. L.; Vega, J. R.; Marchetti, J. L. Relationships between PCA and PLS-Regression. *Chemom. Intell. Lab. Syst.* **2014**, *130*, 182–191.
- (76) Bissett, A. C. Improvements To Pls Methodology. **2015**.
- (77) Jong, S. SIMPLS: An Alternative Approach to Partial Least Squares Regression. *Chemom. Intell. Lab. Syst.* **1993**, *18* (3), 251–263.
- (78) Geladi, P.; Kowalski, B. Partial Least-Squares Regression: A Tutorial. *Anal. Chim. Acta* **1986**, 185.
- (79) van den Berg, R.; Hoefsloot, H.; Westerhuis, J.; Smilde, A.; van der Werf, M. Centering, Scaling, and Transformations: Improving the Biological Information Content of Metabolomics Data. *BMC Genomics* **2006**, *7*.
- (80) Westerhuis, J. A.; Smilde, A. K. Deflation in Multiblock PLS. *J. Chemom.* **2001**, *15* (5), 485–493.
- (81) Lepri, F. G.; Borges, D. L. G.; Araujo, R. G. O.; Welz, B.; Wendler, F.; Krieg, M.; Becker-Ross, H. Determination of Heavy Metals in Activated Charcoals and Carbon Black for Lyocell Fiber Production Using Direct Solid Sampling High-Resolution Continuum Source Graphite Furnace Atomic Absorption and Inductively Coupled Plasma Optical Emission Spectrometry. *Talanta* **2010**, *81* (3), 980–987.

- (82) Malley, D. F.; Williams, P. C. Use of Near-Infrared Reflectance Spectroscopy in Prediction of Heavy Metals in Freshwater Sediment by Their Association with Organic Matter. *Environ. Sci. Technol.* **1997**, *31* (12), 3461–3467.
- (83) Putra, A.; Helmi, S. A Study Characteristics and Detection of Metals Ion in Aqueous Solution by Near Infrared Spectra Area. *Int. J. Sci. Eng.* **2017**, *3* (3), 9–17.
- (84) Soares, L. C.; Alves, J. de O.; Linhares, L. A.; Egreja Filho, F. B.; Fontes, M. P. F. Vulnerability of Tropical Soils to Heavy Metals: A PLS-DA Classification Model for Lead. *Microchem. J.* **2017**, *133*, 258–264.
- (85) Sakizadeh, M.; Mirzaei, R.; Ghorbani, H. Dantiana. *Bull Environ Contam Toxicol.* Springer US 2015, pp 770–776.
- (86) Gannouni, S.; Rebai, N.; Abdeljaoued, S. A Spectroscopic Approach to Assess Heavy Metals Contents of the Mine Waste of Jalta and Bougrine in the North of Tunisia. *J. Geogr. Inf. Syst.* **2012**, *4* (3), 242–253.
- (87) Wu, H.; Liu, X.; Zhao, J.; Yu, J. NMR-Based Metabolomic Investigations on the Differential Responses in Adductor Muscles from Two Pedigrees of Manila Clam *Ruditapes Philippinarum* to Cadmium and Zinc. *Mar. Drugs* **2011**, *9* (12), 1566–1579.
- (88) Cheng, K. L.; Bray, R. H. 1-(2-Pyridylazo)-2-Naphthol as a Possible Analytical Reagent. *Anal. Chem.* **1955**, *27* (5), 782–785.
- (89) Peng, B.; Shen, Y.; Gao, Z.; Zhou, M.; Ma, Y.; Zhao, S. Determination of Total Iron in Water and Foods by Dispersive Liquid-Liquid Microextraction Coupled with Microvolume UV-Vis Spectrophotometry. *Food Chem.* **2015**, *176*, 288–293.
- (90) Tarighat, M. A.; Afkhami, A. Simultaneous Spectrophotometric Determination of Cu(II), Co(II) and Ni(II) Using Ratio Spectra-Continuous Wavelet Transformation in Some Food and Environmental Samples. *J. Braz. Chem. Soc.* **2012**, *23* (7), 1312–1319.
- (91) Ariza-Avidad, M.; Salinas-Castillo, A.; Cuellar, M. P.; Agudo-Acemel, M.; Pegalajar, M. C.; Capitan-Vallvey, L. F. Printed Disposable Colorimetric Array for Metal Ion Discrimination. *Anal. Chem.* **2014**, *86* (17), 8634–8641.
- (92) Ruzicka, J.; Hansen, E. *Flow Injection Analysis*, 2nd ed.; 1988.
- (93) Balconi, M.; Sigon, F.; Borgarello, M.; Ferraroli, R.; Realini, F. Flow-Injection Analysis for Power Plants: Evaluation of Detectors for the Determination of Control Parameters in Conditioned Water—steam Cycles. *Anal. Chim. Acta* **1990**, *234*.
- (94) Ruzicka, J.; Marshall, G. D. Sequential Injection: A New Concept for Chemical Sensors, Process Analysis and Laboratory Assays. *Anal. Chim. Acta* **1990**, *237*, 329–343.
- (95) Lenehan, C. E.; Barnett, N. W.; Lewis, S. W. Sequential Injection Analysis. *Analyst* **2002**, *127* (8), 997–1020.
- (96) Barnett, N. W.; Lenehan, C. E.; Lewis, S. W. Sequential Injection Analysis: An Alternative Approach to Process Analytical Chemistry. *TrAC - Trends Anal. Chem.* **1999**, *18* (5), 346–353.
- (97) Economou, A. Sequential-Injection Analysis (SIA): A Useful Tool for on-Line Sample-Handling and Pre-Treatment. *TrAC - Trends Anal. Chem.* **2005**, *24* (5), 416–425.
- (98) Idris, A. M. An Overview of the Generations and Recent Versions of Flow Injection Techniques. *Crit. Rev. Anal. Chem.* **2010**, *40* (3), 150–158.
- (99) Echols, R. T.; Christensen, M. M.; Krisko, R. M.; Aldstadt, J. H. Selective Determination of TNT in Soil Extracts by Sequential Injection Spectrophotometry. *Anal. Chem.* **1999**, *71* (14), 2739–2744.
- (100) Holman, D.; Christian, G.; Ruzicka, J. Titration without Mixing or Dilution: Sequential

- Injection of Chemical Sensing Membranes. *Anal. Chem.* **1997**, 69 (9), 1763–1765.
- (101) Chow, E.; Ebrahimi, D.; Gooding, J. J.; Hibbert, D. B. Application of N-PLS Calibration to the Simultaneous Determination of Cu²⁺, Cd²⁺ and Pb²⁺ Using Peptide Modified Electrochemical Sensors. *Analyst* **2006**, 131 (9), 1051–1057.
- (102) Bjerrum, J.; Nielsen, O.; Wang, Y.; Olsen, J. Technology Insight: Metabonomics in Gastroenterology—basic Principles and Potential Clinical Applications. *Nat. Clin. Pract. Gastroenterol. Hepatol.* **2008**, 5.
- (103) Ruzicka, J.; Hansen, E. Flow Injection Tutorial <http://www.flowinjectiontutorial.com/>.
- (104) Introduction to a Spectrometer. *Azo Mater.*
- (105) Reichardt, C. Solvatochromic Dyes as Solvent Polarity Indicators. *Chem. Rev.* **1994**, 94 (8), 2319–2358.
- (106) Mai, S.; Ashwood, B.; Marquetand, P.; Crespo-Hernández, C. E.; González, L. Solvatochromic Effects on the Absorption Spectrum of 2-Thiocytosine. *J. Phys. Chem. B* **2017**, 121 (20), 5187–5196.
- (107) Marini, A.; Muñoz-losa, A.; Biancardi, A.; Mennucci, B. What Is Solvatochromism ? *J. Phys. Chem. B* **2010**, 17128–17135.
- (108) Poulson, S.; Drever, J. Aqueous Complex of Nickel and Zinc with MOPS and the Solubility Product Constants of Zinc and Nickel Hydroxides.Pdf. 1996, pp 1975–1981.
- (109) Wold, S. Chemometrics ; What Do We Mean with It , and What Do We Want from It ? *Chemom. Intell. Lab. Syst.* **1995**, 30.
- (110) Tran, T.; Afanador, N.; Buydens, L.; Blanchet, L. Interpretation of Variable Importance in Partial Least Squares with Significance Multivariate Correlation (SMC). *Chemom. Intell. Lab. Syst.* **2014**, 138, 153–160.
- (111) Chandrasekaran, A. Solvents.
- (112) Properties of solvents used in Organic Chemistry
<http://murov.info/orgsolvents.htm#TABLE 2>.
- (113) Common solvents for organic chemistry
https://www.chemistry.mcmaster.ca/adronov/resources/Common_Solvents_for_Organic_Reactions.pdf.
- (114) Lohninger, H. Table of Dipole Moments.
- (115) Barbalace, K. Periodic Table of Elements
<https://environmentalchemistry.com/yogi/periodic/ionicradius.html>.

CURRICULUM VITAE

Joseph T. Labeots

Place of birth: Baraboo, WI

Education:

B.S., Winona State University, May 2014 Major: Chemistry

PhD, University of Wisconsin-Milwaukee, May 2019 Major: Chemistry

Dissertation Title:

A REAL-TIME APPROACH TO PROCESS MONITORING OF HEAVY METALS:
SPECTROPHOTOMETRIC CHARACTERIZATION AND APPLICATION OF NOVEL AZO
DYES

Experience:

Software

- OriginPro and Excel for data analysis
- ReactLab Equilibria for multivariate analysis
- CorelDRAW for graphic design
- Computational chemistry with GAMESS and GAUSSIAN run on a UNIX cluster
- MATLAB

Instrumentation

- UV-Vis absorption spectroscopy
- Fluorescence spectroscopy
- Microfluidics and sequential injection analysis
- Inductively coupled plasma-Mass spectrometry
- Thermocycling for polymerase chain reaction
- Gel electrophoresis for qualitative analysis

- General knowledge of laser spectroscopy

Techniques

- Determination of metal:ligand stability constants by titrimetry
- Multivariate data analysis for determination of stability constants
- Multivariate regression modeling for simultaneous quantification of analytes
- Process optimization and identification of influencing factors through multivariate approaches
- Microfluidics measurements
- Preparation and use of optical fibers
- Genetic recombination procedures including primer design, PCR, ligations, and digestions

Publications/Presentations

- AWRA WI chapter, 2017, poster
 - Optical Approaches to the Detection of Heavy Metals in Water
- SCIX, 2018, Oral Presentation
 - Process Monitoring of Heavy Metals: Spectrophotometric Characterization of Novel Chemosensor Dye

Instructional

- Taught chemistry at the undergraduate level for three years
- Instructed an undergraduate on a research project to identify characteristics of Azo dyes such as acid dissociation constants and metal binding affinities.
- Instructed a MS candidate on a research project that focused on developing analytical techniques for process monitoring of metals.